12-2021

Towards long term colloid suspension in a vertically rotated system.

Md Mahmudur Rahman
University of Louisville

TOWARDS LONG TERM COLLOID SUSPENSION IN A VERTICALLY ROTATED SYSTEM

By
Md Mahmudur Rahman
PhD Candidate, Mechanical Engineering
University of Louisville

A Dissertation Submitted to the Faculty of
the J.B. Speed School of Engineering of the University of Louisville
in Partial Fulfillment of the Requirements
for the Degree of

Doctor of Philosophy in
Mechanical Engineering

Department of Mechanical Engineering
University of Louisville
Louisville, KY 40292

December 2021

TOWARDS LONG TERM COLLOID SUSPENSION IN A VERTICALLY ROTATED SYSTEM

By
Md Mahmudur Rahman
PhD Candidate, Mechanical Engineering
University of Louisville

A Dissertation submitted on

September 24, 2021

To the following Dissertation Committee:

Director: Stuart J Williams, PhD, ME

Gerold Willing, PhD, ChE

Yongsheng Lian, PhD, ME

Ellen Brehob, PhD, ME

This dissertation is dedicated to

my parents Mr. Tohur Ahmad Hilali and Mrs. Afroza Begum,

My wife Rabeya Bosri Ohi,

and

My nine years old son Maher and four years old son Furqan

who were part of my inspiration, love, courage, and endless encouragement.

ACKNOWLEDGMENTS

I would like to thank my PhD advisor, Dr. Stuart J Williams, for his guidance and patience. Without his mentorship, it would be very difficult for me to achieve the work I have accomplished from my PhD studies. He aided me from all aspects such as from acquiring new students for my project, sending me to relevant conferences or even writing codes by himself when I was stuck with a certain problem. I would also like to thank the other committee members, Dr. Gerold Willing, Dr. Yongsheng Lian, Dr. Ellen Brehob, and Dr. Keith Sharp for accepting to be on my dissertation committee and for their comments and assistance over the past five years. I would like to thank John Jones, the technician at the Mechanical Engineering Department who helped me with the design, machining, and fabrication of devices. For the simulation, I used UofL's high speed computing facilities and Harrison Simrall, Director of Research Computing, was very helpful. I was fortunate to guide two graduate students Willis Lee and Arvind Iyer, and their supports for a separate side project was also instrumental in my PhD research. I would like to thank my lab mate and friend Mido Rashed for being a good friend in the lab and offering me academic and emotional supports during my study. Finally, Thanks Allah (God) the Almighty for helping me to navigate this journey which was very satisfactory.

ABSTRACT

TOWARDS LONG TERM COLLOID SUSPENSION IN A VERTICALLY ROTATED SYSTEM

Md Mahmudur Rahman

September 24, 2021

Within a colloidal suspension gravity may compromise the observation of governing physical interactions, especially those that are weak and/or take significant time to develop. Conducting the experiment in a long-term microgravity environment is a viable option to negate gravitational effects, though significant resources are required to do so. While it may not be possible to simulate long-term microgravity terrestrially, particles can resist quick sedimentation in a confined suspension system rotating vertically with appropriate rotation speed. The goal of the investigation is to demonstrate the existence of long-term particle suspension regime for a certain colloidal suspension while characterizing colloidal behavior due to hydrodynamic interactions.

First, to understand the colloidal suspension in a rotational system, I studied the colloidal behavior in such a system where colloidal particles and underlying surfaces interact to each other hydrodynamically. Therefore, I studied the collective behavior of colloidal particles (4.0 µm PMMA), located near the solid surface in a fluid medium confined in a cylindrical cell (3.0 mm diameter, 0.25 mm height)

which was rotated vertically at a low rotational speed (20 rpm). The observed colloidal behavior was then validated through a Stokesian dynamics simulation where the concept of hydrodynamic contact force or lubrication interactions were avoided which is not physically intuitive and mathematically cumbersome. Rather, I adopted hard-sphere like colloidal collision or mobility model. I found that colloidal agglomeration is a function of the applied rotation scheme, either forming colloidal clusters or lanes. While evolving into dynamic structures, colloids also laterally migrate away from the underlying surface.

While forming colloidal structures due to hydrodynamic interactions among particles and nearby solid surface, particles migrate away from the surface and eventually redistribute throughout the sample cell. After redistribution, I demonstrated long term colloidal stability within the sample cell. When particles are redistributed with relatively equal spacing and not concentrated near a solid surface, structure formation is minimized and does not evolve any further which can be considered as long-term suspension.

TABLE OF CONTENTS

LIST OF FIGURES

CHAPTER 1

BACKGROUND

1.1 Introduction

Compared to atomic interactions, structural relaxation time for colloid interactions are much slower, 10^9 times slower than atomic quantity (Bartlett et al., 1991). This macroscopic time scale could be minutes, hours, or even days. Given such slow interaction rates, sedimentation of the colloid particles, due to gravity, can be significant over this time scale. To negate gravity and observe long-term effect of particle interaction, one viable option could be to conduct experiments in microgravity (Zhu et al., 1997; Bailey et al., 2007), as on the International Space station (ISS). However, it costs significant resources and time. Therefore, there have been many attempts to simulate microgravity, a clinostat (Herranz et al., 2013) has been widely implemented in gravitational biology research. However, simultaneous observations of colloids within a microfluidic sample, in a vertically rotating device, have not been widely studied. There is another technique available to limit sedimentation by using density matched suspension medium (Wiederseiner et al., 2011; Zhu et al., 2016). The restriction there is that the specificity involved

in density matching is not amenable to all combinations of particles and fluids. For example, in certain solvents particles can swell, changing their size and density, and may leak the fluorescent dye (Kodger et al., 2017).

A few attempts have been made to simulate microgravity for colloidal suspension (Bartlett et al., 1991; El Masri et al., 2012; Dantuma et al., 2015) by vertically rotating a sample cell. The Bartlett group (Bartlett et al., 1991) worked on sub-micron sized polymethyl methacrylate (PMMA) particles suspended in cis-decalin and carbon disulfide at a rotational speed of one rotation per day. Based on this extremely slow rotational speed, it was likely that the colloid suspension was nearly density matched. The El Masri group studied suspension of 2.2 µm PMMA particles with a density variation with the medium of 0.15 g/ml and rotational speed was 3 rpm (El Masri et al., 2012). Dantuma et al. studied nanoemulsion (particle size 250 nm) stability in a viscous medium (33 cP) while clinostat rotated at 1.6 rpm (Dantuma et al., 2015). Even though these studies lack rigorous characterization of the rotating system and direct comparison with a true microgravity study, they at least suggest that ground based long-term colloid suspension is possible for certain conditions. However, no one looked closely at hydrodynamic interactions among colloidal particles in a rotating system in confinement. Therefore, to pursue a long-term suspension terrestrially, the fundamental physics behind colloidal hydrodynamic interactions in such system needs to be considered. Therefore, this dissertation primarily focused on different regimes such as colloidal structure formation and mixing before establishing a long-term suspension. This research will help establish required parameters for a vertically rotated system to sustain colloid suspension for an extended time (such as, for a week). This work will help

colloid researchers to investigate weak interaction forces. This platform can also study long-term colloid stabilization mechanisms for such cases where gravity otherwise impedes such observations. Further, this platform will enable preliminary inexpensive terrestrial experimentation before being pursued on the International Space Station.

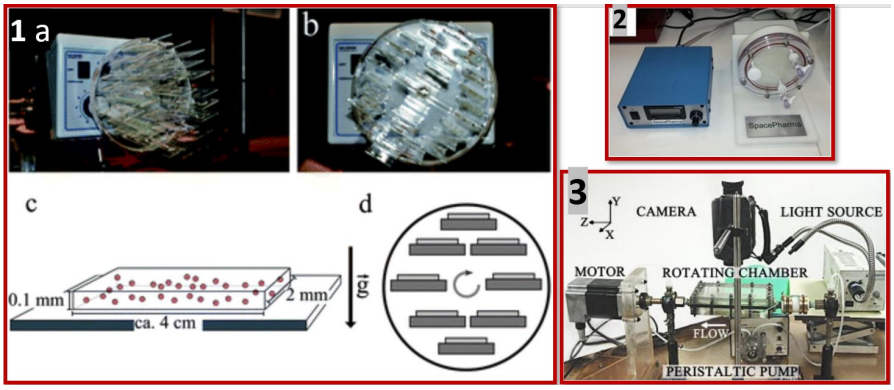

Figure 1.1: Several simulated microgravity devices. 1. Device used by El Masri group for a range of colloidal experiments (El Masri et al., 2012), (a,b) rotating stage loaded with samples, (c,d) sketches of experimental setup, 2. A Rotating Wall Vessel (RWV) (Amselem, 2019) 3. Device used by Boris Khusid group to study the effect of clinorotation and positive dielectrophoresis on suspensions of heavy colloids (Markarian et al., 2004).

1.2 Motivation

There is a growing interest in colloid research to fabricate materials with better thermal (Prasher et al., 2005), electrical (Urban et al., 2007) or optical (Kamat, 2013) properties by tuning their mesoscale crystal structure. Investigating fundamental colloid interactions and stabilization mechanisms is an important task in that goal. To observe long-term effect of certain colloidal interactions, particles need to be continuously suspended for an extended period of time. However, gravity can compromise investigations because heavy particles will settle. There has

not been a thorough study to build a terrestrial platform which can negate gravity settling for colloidal suspensions and to understand hydrodynamic interactions among colloidal particles in such a system. Previous attempts are reported in Section 1.1. However, those studies dealt with very small particles (submicron size) and/or the suspended medium was either close to density matched or highly viscous. In a relaxed parameter setting, such as low viscous medium or non-density matched solution, particles induce fluid motion and thus interact with each other hydrodynamically. Therefore, it is important to conduct a thorough study on a rotational system to establish a set of required parameters to sustain a colloid suspension for a long time.

1.3 Theory

Once momentum is fully transferred from a rotating system to the confined fluid, the fluid rotates as almost rigid body with that rotating system (Stewartson, 1953; Proudman, 1956). However, with the addition of particles, microfluidic motion is induced that disrupts the static nature of the suspension medium. Due to unmatched density between particle and the liquid, centrifugal acceleration can add more complexity and can compromise observations of interparticle forces, just like gravity compromises observation on settling experiments. Therefore, a thorough understanding of how suspended colloids behave on a vertically rotated system is a necessity. In this section, some of the fundamental physical mechanisms that relate to colloidal suspensions in a vertically rotated system are reviewed.

1.3.1 Particle sedimentation

A particle in a liquid suspension reaches terminal velocity within milliseconds. This motion (Figure 1) can be modeled as creeping flow ($Re << 1$). In an ideal scenario (where particle-particle interaction and wall effects are neglected), gravity force (F_d) is balanced by the liquid drag (F_g) as shown below,

$$\sum F = 0 = F_d - F_g \tag{1.3.1}$$

Viscous drag on the particle is given by Stokes's law,

$$F_d = V_{sed}(6\pi\mu a) \tag{1.3.2}$$

where V_{sed}, μ, and a represent particle settling velocity, viscosity of the medium, and particle radius, respectively. At this settling velocity, gravity force on the particle due to weight and buoyancy of the particle is given by,

$$F_g = \frac{4}{3}\pi a^3(\rho_p - \rho_m)g \tag{1.3.3}$$

where, ρ_p and ρ_m represent density of the particle and density of the medium, respectively. Therefore, particle settling velocity can be calculated by the following equation,

$$V_{sed} = \frac{2}{9}a^2\frac{(\rho_p - \rho_m)}{\mu}g \tag{1.3.4}$$

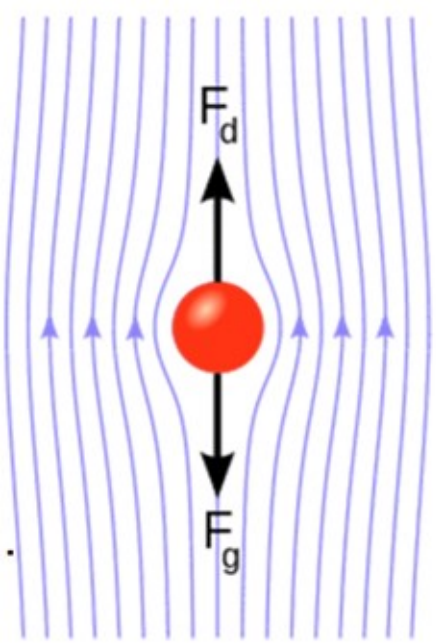

Figure 1.2: Particle in liquid settles at a uniform speed. Gravitational force and fluid drag force are balanced on that falling particle (image credit: Wikipedia).

As we can see from Equation 1.3.4, settling velocity increases as a^2 and thus varies greatly with the particle size. It also increases with the density difference between particle and the medium, and decreases with increasing of viscosity of the medium. An assemblage of particles usually experience an increase in drag and a pair of particles in an infinite fluid fall faster than a single particle (Zapryanov and Tabakova, 1999).

1.3.2 Particle-particle interaction

There is a well-known theory called DLVO (Derjaguin-Landau-Verwey-Overbeek) theory to explain like-charged colloidal interaction. This theory comprises an attractive van der Waals interaction and a repulsive electrostatic double layer interaction. The total attraction potential is described by the sum of attraction potential and repulsion potential. When two particles approach each other, elec-

trostatic repulsion increases and can form a repulsive barrier, as shown in Figure 1.3. If this energy is greater than the thermal energy of the molecular agitation of the liquid medium (Brownian diffusion), colloids may remain repulsed from each other and form a stable solution. Otherwise, particles will aggregate due to the van der Waals attraction potential (Bhattacharjee et al., 1998; Verwey et al., 1948; Derjaguin, 1941). The repulsive electrostatic interaction potential is dependent on the concentration and valence state of counterions, which accompanies a charged particle in order to maintain electric neutrality, and the van der Waals attraction potential is almost independent of the concentration and valence state of counter-ions; the overall potential is strongly influenced by the concentration and valence state of counter-ions. An increase in concentration and valence state of counter-ions results in a faster decay of the electric potential. As a result, the repulsive barrier is reduced and its position is pushed towards the particle surface (Cao, 2005).

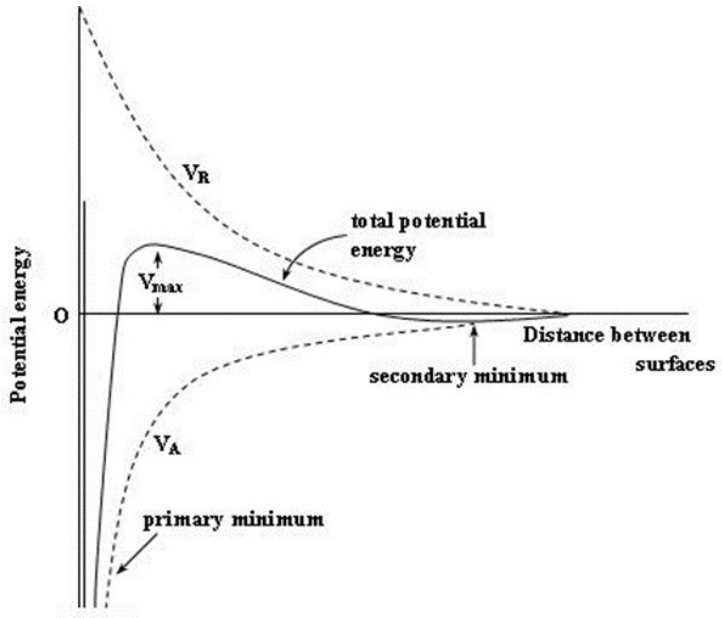

Figure 1.3: The van der Waals attraction potential (V_A), electric repulsion potential (V_R), and the combination of the two opposite potentials as a function of distance from the surface of a spherical particle. At a distance far from solid surfaces, both forces approach to zero. Near the surfaces there is a deep minimum (primary minimum) in the potential energy due to van der Waals attraction. A maximum (V_{max}), known as repulsive barrier, is located a little further away from the surface due to the dominance of electric repulsion potential over van der Waals potential (image credit: Cao (2005))

In addition to this interaction, other interparticle forces can also be present in the solution. Those include, but not limited to, hydrogen bonding, hydrophobic interactions, osmotic pressure, depletion attraction, structural forces, etc. (Grasso et al., 2002).

1.3.3 Object in rotation

If an object is in rotation, its motion and acceleration can be mathematically described from the following two equations,

$$\mathbf{V}_{in} = \mathbf{V}_{rot} + \omega \times \mathbf{r} \tag{1.3.5}$$

$$\mathbf{a}_{in} = \mathbf{a}_{rot} + 2\omega \times \mathbf{V}_{rot} + \omega \times (\omega \times \mathbf{r}) + \frac{d\omega}{dt} \times \mathbf{r} \tag{1.3.6}$$

where, $\mathbf{V}$ and $\mathbf{a}$ represent velocity and acceleration, respectively, at a distance $\mathbf{r}$ from the center of rotation, and ω represents angular velocity of the rotating object. Subscript 'in' indicates Inertial Reference Frame (IRF, non-rotational) and subscript 'rot' indicates Rotational Reference Frame (RRF, 'non-inertial'). In Equation 1.3.6, the second, third, and fourth terms are known as Coriolis acceleration, centrifugal acceleration, and Euler acceleration, respectively. For a uniformly rotational case, Euler acceleration is negligible.

Now we will try to understand physically each terms' contribution from the following two cases.

Motion and forces obtained from RRF while object is stationary in IRF

An object A is fixed on an inertial reference frame (IRF), as shown in Figure 1.4. This object is being observed from a rotational reference frame (RRF) which is rotating counterclockwise with an angular velocity ω.

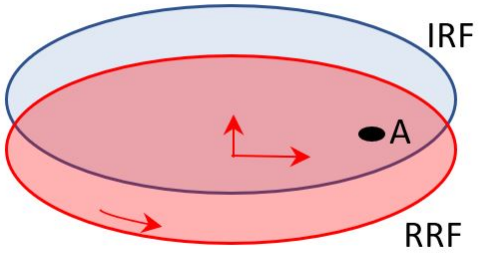

Figure 1.4: An object A is fixed on an inertial reference frame. This object is being observed from a rotational reference frame which is rotating counterclockwise with an angular velocity of ω.

As body A is not moving in IRF, $V_{in} = 0$, and therefore, we get, from Equation 1.3.5, $\mathbf{V}_{rot} = -\omega \times \mathbf{r}$. We know that there is no force acting on the object. Therefore, the object is stationary in IRF. However, if we observe object A from RRF, the object is rotating clockwise in a circular orbit with a velocity $\omega \times \mathbf{r}$. If we place $\mathbf{a}_{in} = 0$, $\frac{d\omega}{dt} \times \mathbf{r} = 0$ and $\mathbf{V}_{rot} = -\omega \times \mathbf{r}$ in Equation 1.3.6, we can find an apparent acceleration on the body as, $\mathbf{a}_{rot} = -\omega \times \mathbf{V}_{rot}$ or $\mathbf{a}_{rot} = \omega \times (\omega \times \mathbf{r})$ (Figure 1.5) , which always acts perpendicular to the body's motion and is directed towards the center . This apparent acceleration can be termed as both centripetal acceleration and Coriolis acceleration as both definitions describe the term. No matter how they are defined, there is no actual force acting on the body.

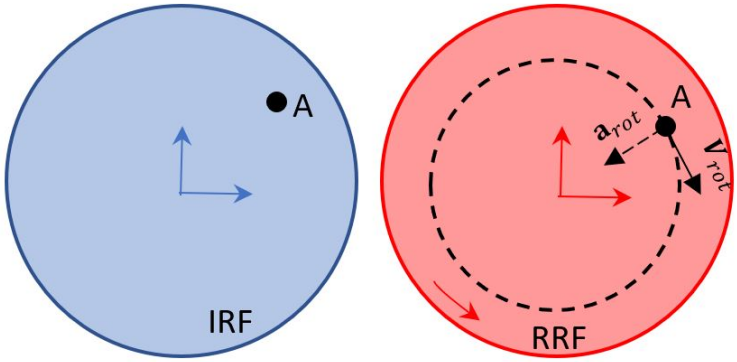

Figure 1.5: Object A is moving counter clockwise, as can be seen from RRF, with a velocity $\omega \times \mathbf{r}$, while remains stationary in IRF.

However, if the object is at uniform motion in IRF, the acceleration (fictitious) on the object with respect to RRF would be,

$$\mathbf{a}_{rot} = -2\omega \times \mathbf{V}_{in} + \omega \times (\omega \times \mathbf{r}) \tag{1.3.7}$$

Again, the second term of Equation 1.3.7 is causing a circular orbit of that uniformly moving object in RRF while another fictitious force ($2\omega \times \mathbf{V}_{in}$) is acting on

the object which is always perpendicular to the direction of motion in the inertial frame.

Force acting on a body resting and moving on RRF

Now, let's consider another scenario where an object is sitting on a system which is rotating counterclockwise. Radial distance from the center of rotation to that object is $\mathbf{r}$. From Equation 1.3.5, we get $\mathbf{V}_{in} = \omega \times \mathbf{r}$, as $\mathbf{V}_{rot} = 0$. From Equation 1.3.6, we get $\mathbf{a}_{in} = \omega \times (\omega \times \mathbf{r})$ which is termed as centripetal acceleration, directing radially inward. To keep the object in place centripetal acceleration is necessary. It can either be pulling through the material between the object and the center of rotation or pushing through the material situated radially outward from that object. Otherwise, the object would move radially outward as it experiences acceleration due to rotation, which is termed as centrifugal acceleration or inertial acceleration. These two forces balance and thus the object remains stationary in a rotational reference frame while rotating in an orbit in an inertial reference frame.

Now, let's see how the body will experience forces if the object is moving, arguably, at a uniform speed in RRF. Again, we can derive this from Equation 1.3.6,

$$\mathbf{a}_{in} = 2\omega \times \mathbf{V}_{rot} + \omega \times (\omega \times \mathbf{r}) \tag{1.3.8}$$

To retain object motion $\mathbf{V}_{rot}$ at RRF, $2\omega \times \mathbf{V}_{rot}$ and $\omega \times (\omega \times \mathbf{r})$ forces are necessary. These forces are provided through rotation. In other words, the object experience these forces in opposite direction in rotation which we term as Coriolis acceleration $(-2\omega \times \mathbf{V}_{rot})$ and centrifugal acceleration $(-\omega \times (\omega \times \mathbf{r}))$. Result is

shown graphically in Figure 1.6.

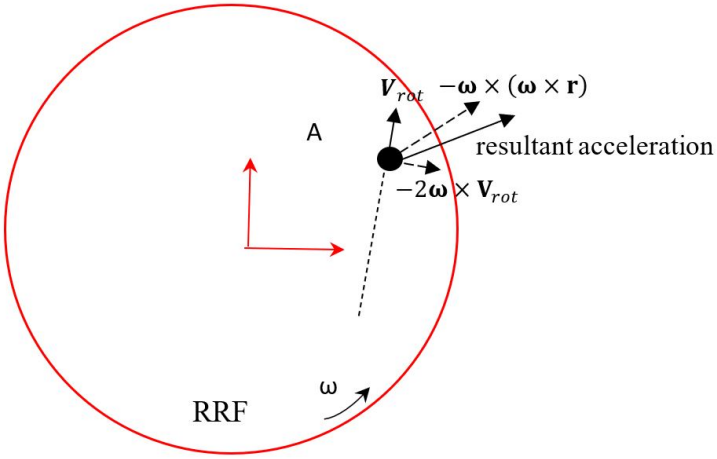

Figure 1.6: Graphical representation of the forces that object A experiences when it moves at a uniform speed in RRF. Vectors are not drawn to scale. Depending on the magnitude of the resultant force, motion path can deviate to the right, noted as resultant acceleration

1.3.4 Peclet number

Particles experience Brownian motion when suspended. Whether a particle settles or not depends on Peclet number, Pe, ($\frac{V_{sed}a}{D}$). Here, D represents Brownian diffusion coefficient ($\frac{k_BT}{6\pi\mu a}$), where, k_B = Boltzman's constant = $1.3806503 \times 10^{-23} J/K$, T = absolute temperature, μ = viscosity of the medium. If $Pe < 1$, particles will remain in the colloid solution and will likely not settle unless they aggregate and form larger clusters.

1.3.5 Colloids in a vertically rotated cell

In rotation, colloidal particles continuously settle due to gravity ($\mathbf{F}_g$). However, the gravity vector rotates at the speed of rotation. Therefore, particles sink in a circular path. As particles are in rotation, centrifugal ($\mathbf{F}_c$) and Coriolis ($\mathbf{F}_{Cor}$)

forces act on those particles. Particles are driven by the resultant force which is balanced by the viscous drag force ($\mathbf{F}_d$), as shown below

$$\mathbf{F}_d = \mathbf{F}_g + \mathbf{F}_c + \mathbf{F}_{Cor} \tag{1.3.9}$$

Besides all these forces, particles experience Brownian motion. Brownian velocity (RMS distance traveled per second) can be calculated as follows,

$$v = \sqrt{\frac{k_{BT}}{3\pi a \mu t}} \tag{1.3.10}$$

With the decrease of the particle size (a), Brownian motion becomes higher and the particle remains suspended longer. From Equation 1.3.4, we have seen that with the decrease of particle size, particles' settling speed decreases since it's proportional to a^2. With the increasing distance of the particle from the center of rotational axis, the particle experiences higher centrifugal acceleration. Therefore, smaller size particles, with lower rotational speed and with a sample cell of smaller radius, can be the ideal scenario for long-term colloid suspension such that unintended fluid motion due to particle mobility as a consequence of rotation is not created. However, larger particles sediment faster and with lower Brownian motion larger particle size and density create challenges to sustain long-term colloid suspensions. Ideally, velocity derived from Brownian diffusion is not equivalent to the concept of velocity. Brownian diffusion measures the root mean square displacement of the particle with respect to time. For example, in 4 s particle may travel twice the distance of what it would travel in 1 s. Therefore, comparison

Table 1.1: Settling velocity, Brownian velocity and Peclet number for different particle choices

Particle size (μm)	Material	Density (g/cc)	Settling Velocity ($\mu m/s$)	Brownian Velocity ($\mu m/s$)	Peclet Number
0.1	Polystyrene	1.05	3.06×10^{-4}	2.21	3.12×10^{-6}
1.0	Polystyrene	1.05	3.06×10^{-2}	7.00×10^{-1}	3.12×10^{-2}
4.0	Polystyrene	1.05	4.90×10^{-1}	3.50×10^{-1}	7.99
0.1	PMMA	1.22	1.35×10^{-3}	2.21	1.37×10^{-5}
1.0	PMMA	1.22	1.35×10^{-1}	7.00×10^{-1}	1.37×10^{-1}
4.0	PMMA	1.22	2.60	3.50×10^{-1}	35.2
0.1	SiO_2	1.81	4.96×10^{-3}	2.21	$5.06\ _{-5}$
1.0	SiO_2	1.81	4.96×10^{-1}	7.00×10^{-1}	$5.06\ _{-1}$
4.0	SiO_2	1.81	7.94	3.50×10^{-1}	129

between sedimentation velocity and Brownian 'velocity' in 1 sec can show us an intuitive understanding of the flow dynamics of the suspension. Brownian diffusion and particle sedimentation is compared for different particle size and density in Table 1.1 where the suspension medium is water at room temperature.

1.3.6 Functional weightlessness

A state of "relative motionlessness" is defined with respect to the simultaneous contributions of gravity, centrifugation, and Brownian motion acting on the suspended particle. By selecting an appropriate rotational speed, particle movement due to sedimentation and centrifugation can be kept within the limits of Brownian "noise" (Klaus et al., 1998).

D.M. Klaus et al. (Klaus et al., 1998) showed how to set minimum rotational speed to achieve 'functional weightlessness'. At low rotational velocity and within a small sample cell, linear motion of particle sedimentation is transformed into a near circular path. To achieve 'functional weightlessness', this circular path has to be within the Brownian displacement radius (diffusion length, R_B) within that

time. Time to travel one circular orbit when the system is rotating at N_{min} rpm is,

$$t = \frac{60}{N_{min}} \tag{1.3.11}$$

Over this time, the particle travels a circumference equal to the distance $2\pi R_B$. Dividing this distance by t, we can get the expression for a particle's sedimentation velocity. Rearranging we get an expression for R_B as the following,

$$R_B = \frac{30 V_{sed}}{\pi N_{min}} \tag{1.3.12}$$

From Equation 1.3.10, the expression for Brownian velocity can be multiplied with t, to get Brownian displacement R_B.

$$R_B = \sqrt{\frac{20 K_B T}{\pi a \mu N_{min}}} \tag{1.3.13}$$

Equating equation 1.3.12 and 1.3.13 we get the expression for the minimum required rotational speed, N_{min}. We also know V_{sed} from Equation 1.3.4.

$$N_{min} = \frac{20 {a_p}^5 (\rho_p - \rho_m)^2 g^2}{9\pi\mu K_B T} \tag{1.3.14}$$

where a_p, ρ_p,ρ_m,μ,K_B, and T represents particle radius, particle density, density of the medium, viscosity of the medium, Boltzman's constant, and temperature. N_{min} increases with ${a_p}^5$ and with $\Delta\rho^2$. Quantitatively, this is shown in Table 1.2.

Table 1.2: Particle size and corresponding minimum rotational velocities for achieving 'functional weightlessness' as proposed by D.M. Klaus et al.

Particle size (μm)	Density (g/cc)	Settling Velocity V_{sed}, ($\mu m/s$)	Required RPM N_{min}
4	1.05	0.52	1.66
4	1.22	2.17	29.43
4	1.51	5	155.8

Three different particles with different size and density are suspended in water at room temperature. Minimum required rotational velocities to achieve functional weightlessness for different particles are shown in Table 1.2.

This theoretical analysis shows promise for long term suspension for particles with small radii and low-density differentials with the medium. However, with the increase of particle size and density, high rotational speed is required. With the increase of rotational speed, centrifugal acceleration will compromise observation as particles will drift towards the circumference of the sample cell.

1.3.7 Colloidal hydrodynamic interactions

Reynolds number of the fluid flow due to sinking microparticles is very low (in the order of $10^{-}5$). Therefore, the flow dynamics is purely viscous and described as Stokes flow. The velocity field is shown by the following equation (Furst and Squires, 2017; Rotne and Prager, 1969),

$$\mathbf{V}(\mathbf{r}) = \frac{1}{8\pi\mu r}\left[(\mathbf{F} + (\mathbf{F}.\hat{\mathbf{r}})\hat{\mathbf{r}}) + \frac{a^2}{3r^2}(\mathbf{F} - 3(\mathbf{F}.\hat{\mathbf{r}})\hat{\mathbf{r}})\right] \tag{1.3.15}$$

where $\mathbf{F}$ and $\mathbf{r}$ represent force and position vectors. The flow field caused by a sink-

ing microparticle influences other microparticles through short range (second part of Equation 1.3.15) and long-range interactions (first part of Equation 1.3.15). The velocity field is shown graphically in Figure 1.7. Through many-body interactions colloidal particles can form dynamic structures. Therefore, in an active colloidal system, it is important to characterize colloidal hydrodynamic interactions in a rotational system. The details of hydrodynamic interactions among mobile colloidal particles are explained in Chapter 3 where we developed a modified simulation approach for colloidal hydrodynamic interactions.

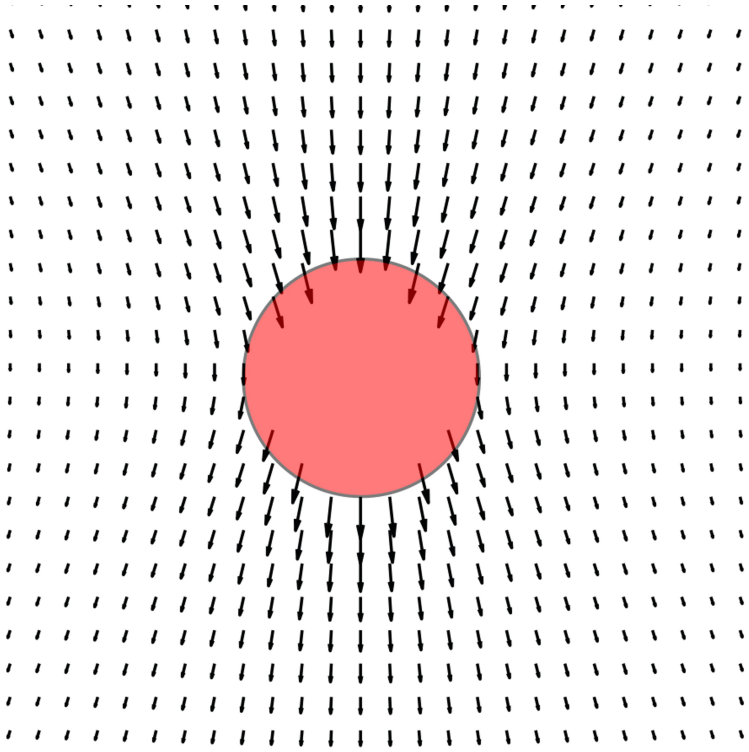

Figure 1.7: Velocity field caused by a single particle's sedimentation/mobility influences fluid at a large distance as long ranged velocity field decays as $1/r$.

1.3.8 Electrostatic repulsion interaction

In a colloidal suspension charged spheres can be important especially for attraction interaction or a combination of attraction (such as van der Waals or others,

as discussed in Section 1.3.2) and repulsion interaction which would lead to an isoelectric point where minimum energy principle can be applied. However, in case of very short ranged repulsion interaction compared to the particle size, due to same charge among interacting colloids, particles can be modeled as hard sphere colloids. When colloids are dispersed in an aqueous medium with a large dielectric constant, counterions in the solution screen surface charges to a significant extent which weakens the repulsion interaction in the long range (Choi et al., 2019; Pantina and Furst, 2004). As a result, particle to particle electrostatic repulsion forces operate typically on the order of several nanometers. However, in an organic solvent with moderate dielectric constant, a relatively small amount of surface charge is produced and therefore, less charge screening occurs (Choi et al., 2019; Royall et al., 2003). The resulting electrostatic repulsion is stronger than in an aqueous solution.

CHAPTER 2

DEVICE DESIGN AND CHARACTERIZATION

2.1 Introduction

A true investigation on colloid interaction demands long-term particle suspension to characterize weak interaction forces that are otherwise masked by gravity and to observe interactions for an extended time. This unique environment, especially for heavier particles, is not possible on ground-based experiments due to gravity settling. We need to keep particles suspended for a long time to observe long term effects of certain colloidal interactions. To address this, we designed a vertically slow rotating platform that can hold a sample cell as a mean of long-term suspension. A thorough characterization of this system needs to be carried out to further prove that this device can suspend colloids for an extended time without introducing unintended interactions.

2.1.1 Particle's translating orbit within its radius

From Equation 1.3.9, gravity, centrifugal acceleration and Coriolis force are balanced by fluid drag force. Centrifugal acceleration ($\mathbf{a}_c = \omega \times (\omega \times \mathbf{r})$) is lowest (zero) at the center and grows higher when it is further away from the center. It also increases with the square of rotational speed. To keep the effect of centrifugal acceleration smaller relative to the gravity, we chose a small sample cell (3 mm diameter) and low rotational velocity (< 60 rpm). With this sample size and rotational velocity selection, the relative contribution of gravity and maximum (at the edge of the sample cell) centrifugal acceleration is shown in Figure 2.1. Relative contribution of gravity and Coriolis acceleration is shown in Figure 2.2.

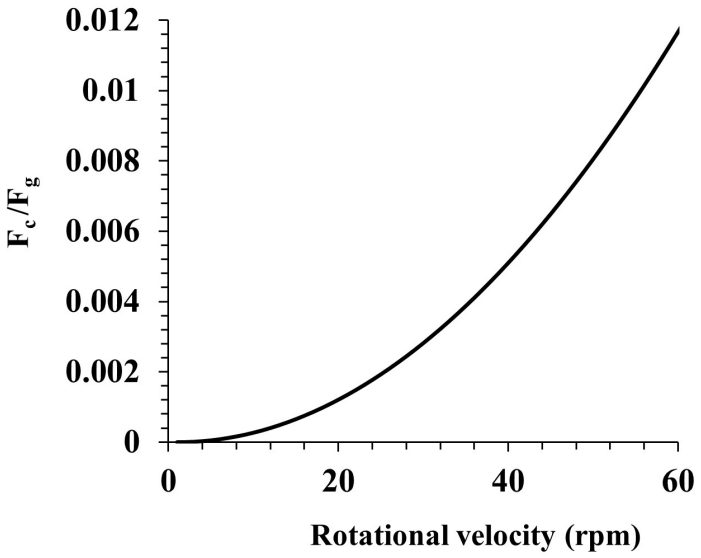

Figure 2.1: Relative contribution of centrifugal (F_c) and gravity acceleration (F_g) with respect to rotational velocity (rpm).

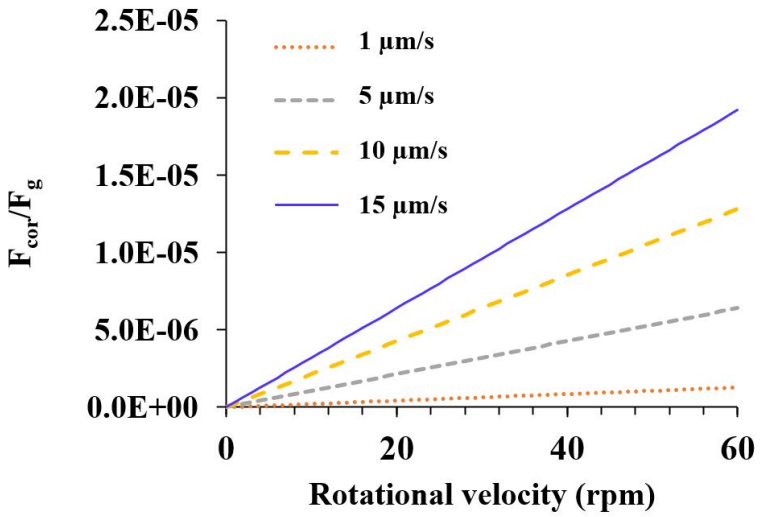

Figure 2.2: With the increase of particles' settling velocity, Coriolis acceleration increases as well. However, this acceleration, on the particle, is extremely small compared to the gravity acceleration.

Because of very small effects from centrifugal acceleration and Coriolis acceleration, we neglected their contribution in our calculations. Now, as only gravity forces are significant, the particle translates, in one rotation, the same distance as it would settle in a non-rotational case. Further, the particle's trajectory is in a circular orbit in rotation. Knowing their settling velocity, we can calculate the radius of circular orbit according to Equation 1.3.12. Rearranging and setting particle radius a_p instead of R_B in Equation 1.3.12, we get minimum rotational speed to confine the particle's circular orbit within particle's radius,

$$N_{min} = \frac{60 V_{set}}{2\pi a_p} \tag{2.1.1}$$

With the increase of particle's sedimentation velocity, particles sink in a larger circular orbit (as demonstrated in Figure 2.3 with bigger particles and larger sample cell). Therefore, minimum rotational velocity to confine particle's circular orbit

Table 2.1: Particle size and corresponding rotational speed for keeping translating orbit within the particle's size.

Particle size (μm)	Density (g/cc)	Material	Settling Velocity V_{sed}, ($\mu m/s$)	Minimum rotational velocity required, rpm
4	1.05	Polystyrene	0.52	2.5
4	1.22	PMMA	2.17	10.5
4	1.51	Melamine resin-FITC	5	24
3.62	1.81	SiO_2	6.5	34.3

within its radius also increases. However, increasing rotational velocity will increase centrifugal acceleration (Figure 2.1). This limitation in rotational speed also affects particle selection, as shown in Table 2.1. We selected 4 µm PMMA as a model particle to study and characterize hydrodynamic interactions due to the particle's mobility (Chapter 3 and 4). Rotational speed was set to 20 rpm to further reduce orbital path at which the particle translates while the system is rotating.

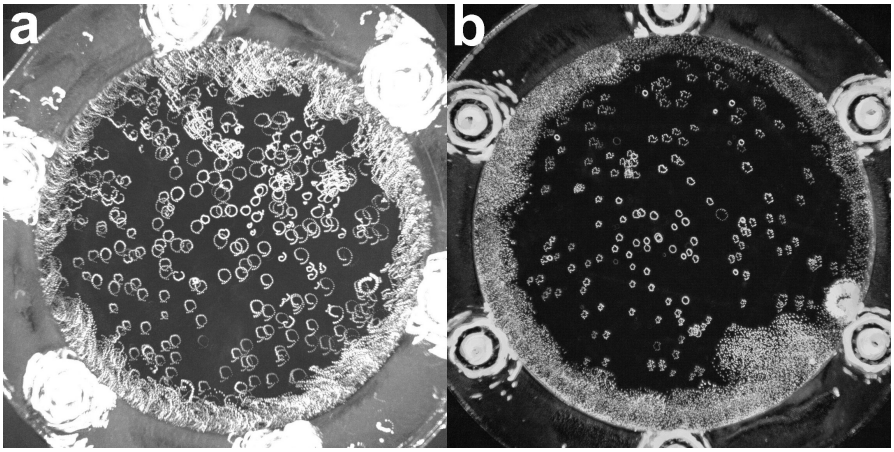

Figure 2.3: Demonstration of particle's translation in a near circular orbit when the sample cell (60 mm × 3 mm) rotates uniformly at (a) 23 rpm and at (b) 32 rpm counterclockwise. Particle size and specific gravity are 150 µm and 1.15, respectively. Calculated sedimentation velocity is 2.07 mm/s. Calculated (from Equation 1.3.12) radius of the circular orbits are (a) 0.86 mm and (b) 0.62 mm. Sequential images were captured in one rotation. All captured images were registered on the same position of the sample cell. All registered images were added to view particle trajectory.

2.1.2 Non-dimensional analysis on volumetric fluid displacement

A non-dimensional number is suggested that compares the volume displaced per revolution from the particles with the volume of the well. This takes into the concentration of particles and their particle-settling fluid volume displacement. The proposed non-dimensional number is,

$$\frac{Q_p}{\mathbb{V}_w} T \tag{2.1.2}$$

where, Q_p is the effective volumetric flow of displaced fluid volume due to translated particle, $\mathbb{V}_w$ is the volume of well, and T ($= \frac{60}{N}$, where N is the rpm) is the period of well orbit; centrifugal forces are assumed negligible.

While sinking, a particle displaces fluid from its moving path. The projected area of a spherical sinking particle is πa^2 (Figure 2.4).

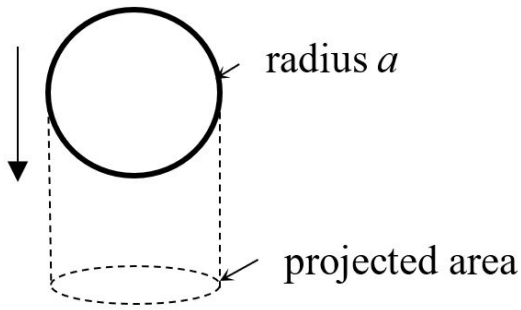

Figure 2.4: A particle with radius a is sinking at its settling velocity and displaces fluid from its moving path.

The volumetric displacement per unit time due to the motion of a single particle can be calculated as follows,

$$Q_{single\ particle} = V_{sed}\left(\pi a^2\right) \tag{2.1.3}$$

Total volumetric displacement per unit time, $Q_p = Q_{single\ particle} \times (Number\ of\ particles)$. Therefore, the proposed non-dimensional number is,

$$\frac{Q_p}{\mathbb{V}_w} T = \frac{(\rho_p - \rho_m)\, g\, (\pi a^2)}{6\pi\mu a} \left(\frac{\mathbb{V}_p \times No.\ of\ particles}{\mathbb{V}_w}\right) T \tag{2.1.4}$$

After simplification we get,

$$\frac{Q_p}{\mathbb{V}_w} T = \frac{10\,(\rho_p - \rho_m)\, gaC}{\mu N} \tag{2.1.5}$$

where, C is the particle concentration (% volume), N is rotational velocity. This non-dimensional number increases with the increase of particle density, size, and concentration and with decreasing rotational velocity. This non-dimensional number intuitively represents a ratio of inertial fluid pressure caused by many particles mobility to the rotational viscous effect and can be valid when there is no secondary flow induced by other means (such as from side wall interactions or centrifugal acceleration).

2.2 Methods

2.2.1 Constructing a vertically rotating platform

Based on the above discussion, we built a rotational platform (Figure 2.5). This rotational platform was designed to rotate at a constant rotational velocity with low angular velocity (3.5 rpm to 60 rpm). The platform was attached to a motor (Cytron OEM, SPG30-60K) and rotated vertically (rotational axis is orthogonal to the direction of gravity). The white LED light source was placed at an oblique angle for scattered imaging which was enhanced further with a black background. Lights are programmed through a Raspberry Pi. Those turned on right before the image was taken to avoid light-induced thermal effect. A C-mount CCD camera (PCO.sensicam from PCO AG, Kelheim, Germany) with appropriate microscope objective lens (2X, 4X and 10X) was placed on an optical table. The camera captured images (exposure time of 500 µs) of the sample cell at the same location once per revolution.The camera trigger was also programmed through the same Raspberry Pi. Circular sample holder (2.6 held an extended arm from its center which was used to disrupt transmission to an Infrared (IR) sensor (from Adafruit, model number ADA2167). Raspberry PI then calculated rotational speed from the signal received from IR sensor. This signal would simultaneously turn on the LED lights and subsequently trigger the digital camera.

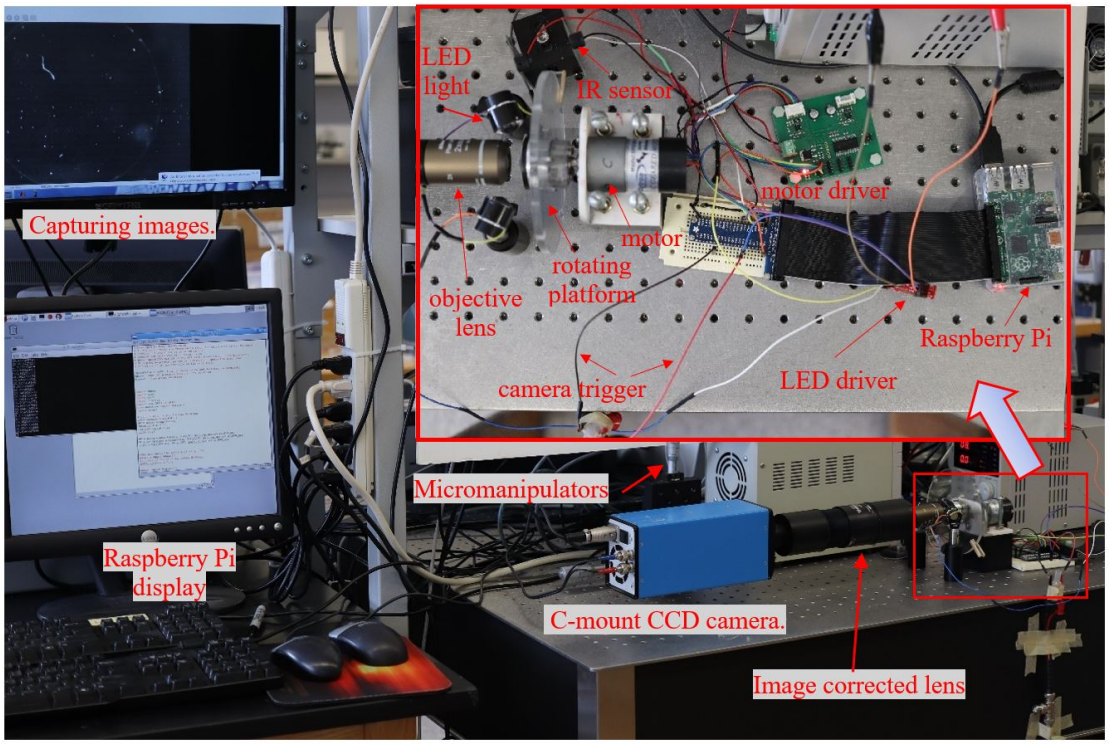

Figure 2.5: C-mount CCD Camera with infinity corrected lens and microscope objective is mounted, at the rotational axis, on a three-axis micromanipulator which is fixed on a non-rotating optical table. A microcontroller (Raspberry Pi) can control the LED light and camera trigger, and it receives signal from IR sensor. Rotational velocity can also be adjusted through the microcontroller as required. This setup is designed for uniform rotational velocity throughout the experiment.

2.2.2 Designing a sample cell holder

The rotating platform (Figure 2.6) was connected vertically to the motor shaft. It held a sample cell at the center of the rotational axis. For keeping the sample at the center, there were three (they are apart from each other at 120°) screws located on the sample cell holder. For observing colloids in a long-term period (say for a week), we captured images exactly at the same angular position at each revolution with the help of an IR sensor as mentioned in Section 2.2.1.

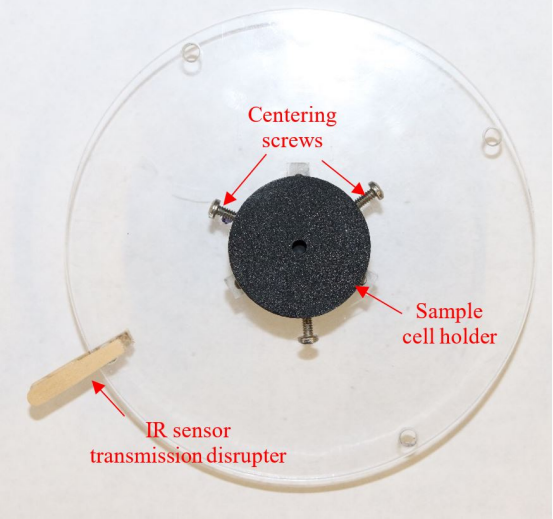

Figure 2.6: Rotating platform with sample cell holder. Sample cell holder contains three screws which can be used for placing sample at the center of the axis of rotation. Image is taken once in a rotation when IR sensor does not receive transmitted signal due to the blockage of extended wooden bar connected to the rotating platform.

2.2.3 Designing a microfluidic device

For a preliminary assessment of the device, we prepared 3 mm x 0.16 and 3 mm x 0.25 mm raised circular feature which was patterned on a silicon wafer via photolithography using SU-8 photoresist and served as a mold. PDMS was poured onto the mold, cured, and removed to create the wells. A Plasma-treated glass slide and the backside of the PDMS mold were bonded together to give the well structural stability and a mounting surface (Figure 2.7). The colloidal sample was then suspended in an appropriate aqueous medium and poured into the well. To avoid trapped air bubble inside the well, PDMS well was plasma-treated beforehand to make it more hydrophilic. A glass cover slip was placed on top of the deposited colloid droplet. After wiping excess solution, surface tension by itself was sufficient to hold the cover slip in place throughout the experiment.

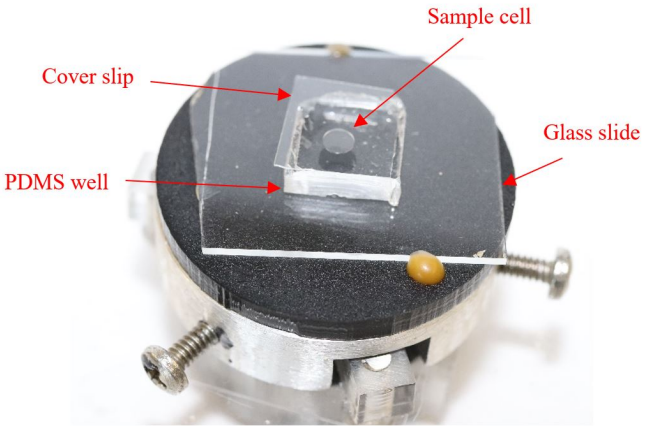

Figure 2.7: Sample cell as a circular well was fabricated using PDMS which was then attached on the sample holder, with the help of capillary wax, at the center of the axis of rotation.

In line with the simulation (discussed in Chapter 3, we set up experiments accordingly and also explore different colloidal suspensions with varying concentrations. In our experimental setup, we developed a 3.0 mm diameter by 250 µm deep cylindrical sample cell, made from PDMS, which contained the monodisperse colloidal sample. In the PDMS device, uniformly distributed colloid mixture was injected from inlet and ejected through the outlet. Prior to experimentation, the sample was inspected for bubbles, as a bubble-free sample is needed for our experiments. Microfluidic channels connecting the inlet/outlet to the cylindrical cell were made in a serpentine shape to increase hydraulic resistance and thereby reduce unwanted hydrodynamics due to any trapped air bubble at the inlet/outlet ports, as shown in Figure 2.8. Once the PDMS device was loaded with the colloid sample, inlet and outlet ports were sealed using capillary wax and nail polish. Particles were kept at rest for at least 10 minutes to let them sediment on the bottom of the cell. The sample cell was then loaded to our rotating platform (see Section 2.2.1 and 2.2.2).

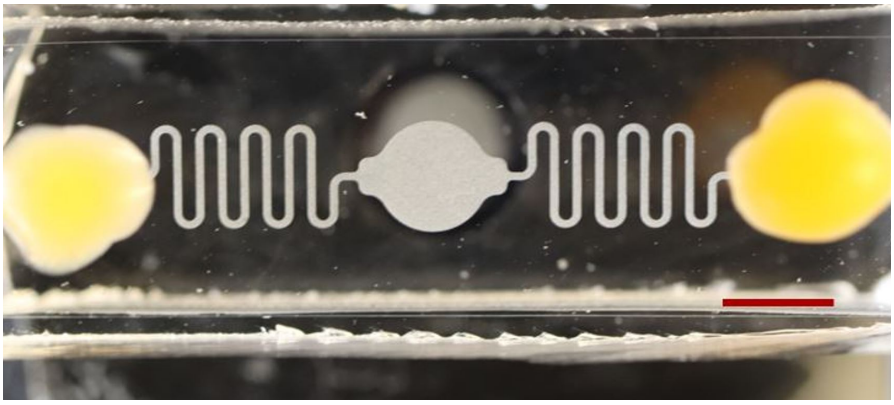

Figure 2.8: To minimize bubble formation during colloid sample injection, inlet and outlet ports were made to a 3.0 mm by 250 µm cylindrical well. To minimize further unintended fluid motion due to air bubbles which may be entrapped at inlet and/or outlet, serpentine shaped channel was produced. Scale bar: 3 mm. The image is shown here to demonstrate sample cell design only, not for the actual experiment.

2.2.4 Colloidal sample preparation

For device characterization and observation of colloidal stability, 8 μm polystyrene and 3.62 μm silica microspheres were used at different concentrations suspended in DI water. 2.0% (V/V) non ionic surfactant and emulsifier Tween 20 was used to prevent unwanted particle aggregation to the PDMS or glass surface.

2.2.5 Image analysis

After capturing, images were processed using the software *Fiji Is Just ImageJ (FIJI)*. Then, particle tracking or fluid flow analysis was done using the technique called particle image velocimetry (PIV). MATLAB's PIVlab tool (Thielicke and Stamhuis, 2014) was used for PIV analysis. For particle tracking in thermophoresis experiments (Section 2.4), we used FIJI's TrackMate plugging.

2.3 Results

While making the platform suitable for long-term particle suspension and developing a proper imaging setup, we conducted many experiments (sample cell size 3 mm $\times$ 160 µm and 3 mm $\times$ 250 µm) to converge operational parameters towards the goal. Some of the key results are described below.

2.3.1 Absence of bulk flow and uniform pressure field

In a sealed sample cell fluid rotates with the system as a rigid body (Stewartson, 1953; Proudman, 1956). We verified rigid body rotation for our system by introducing a very sparse particle concentration; we observed no bulk fluid motion when the system was rotating at a uniform speed. The result is shown in Figure 2.9. Polystyrene particles were used as tracer particles to observed fluid flow due to rotation. We did not observe any streamlines in particle image velocimetry (PIV) analysis, except particle's Brownian motion.

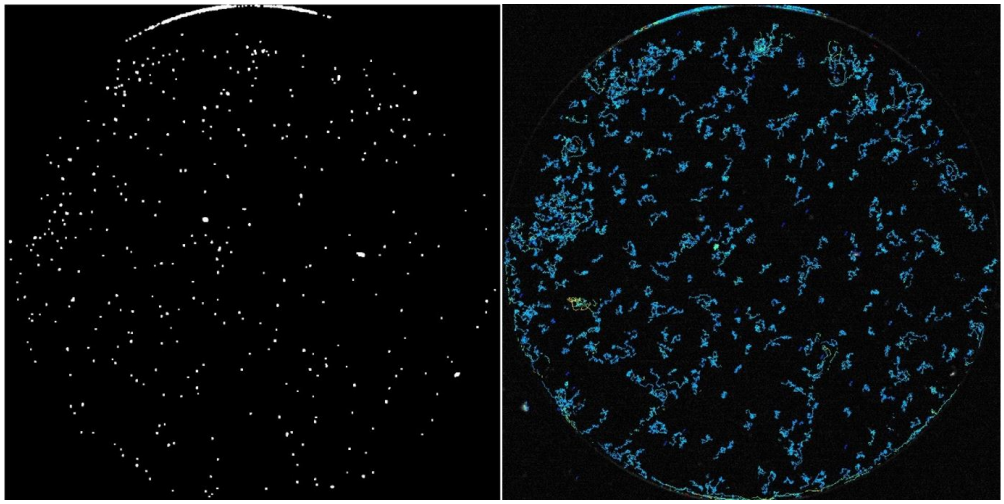

Figure 2.9: 8 μm polystyrene particle with very low concentration is distributed in distilled water (left). Sample cell (3 mm $\times$ 160 μm) was run at 3.5 rpm (left). Particle position was tracked for the entire experiment time (1 day). Result (right) is shown for the observation period of 3.5 hours from the beginning of rotation. No bulk fluid motion was observed, except random particle motion.

It is important to eliminate trapped or floating air bubbles in the rotational sample cell. It is obvious that floating air bubbles disrupt overall fluid motion. However, trapped air bubbles can cause non-uniform or pulsatile pressure field which can influence particle trajectory. Gravity, and pressure gradient (from non-uniform pressure filed) combined and resulted in a unique motion path of the suspended particles (Figure 2.10).

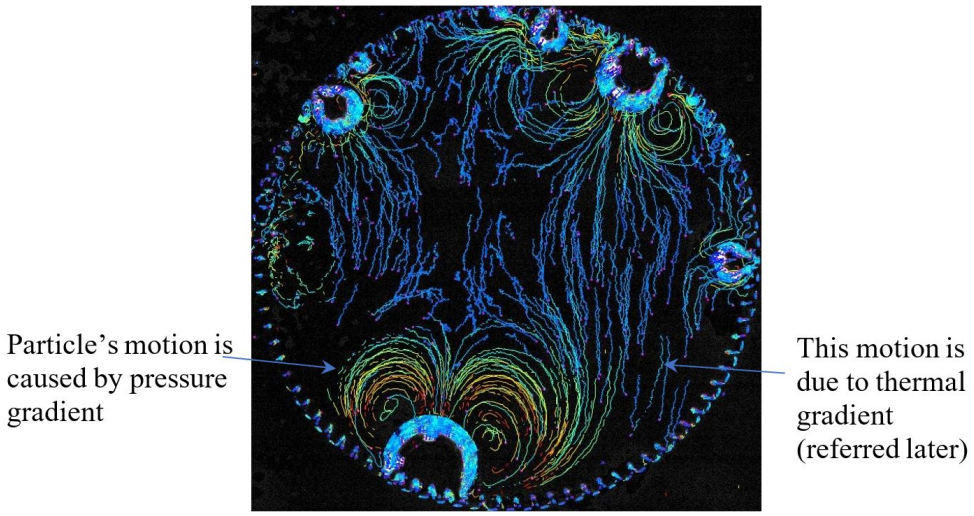

Figure 2.10: Effect of pressure gradient due to trapped air bubble. 8 μm polystyrene (specific gravity 1.05) sample cell was rotated at 17 rpm.

2.3.2 Particle induced fluid motion

As discussed in Section 2.1.1 and 2.1.2, the particle's motion in a circular orbit and volumetric displacement of fluid depends on the rotational speed and the volume concentration of the particles. For a low concentration of particles, the fluid rotates as a rigid body and no bulk fluid motion is observed (Figure 2.9). However, with the increase of particle concentration (and density) bulk fluid motion was observed (Figure 2.11 and 2.12).

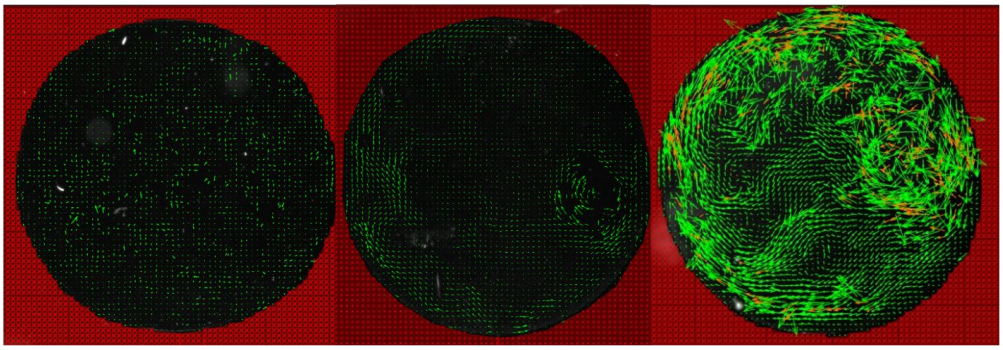

Figure 2.11: 3.62 μm Silica particle (specific gravity 1.81, average settling speed 6.5 µm/s), rotated at 10 rpm. Particle concentration is 0.01%, 0.05% and 0.1% w/v (from left to right). Particle image velocimetry (PIV) analysis is showing particle induced fluid motion. Images were taken 3 hours later, once particles redistributed and remained suspended for long time.

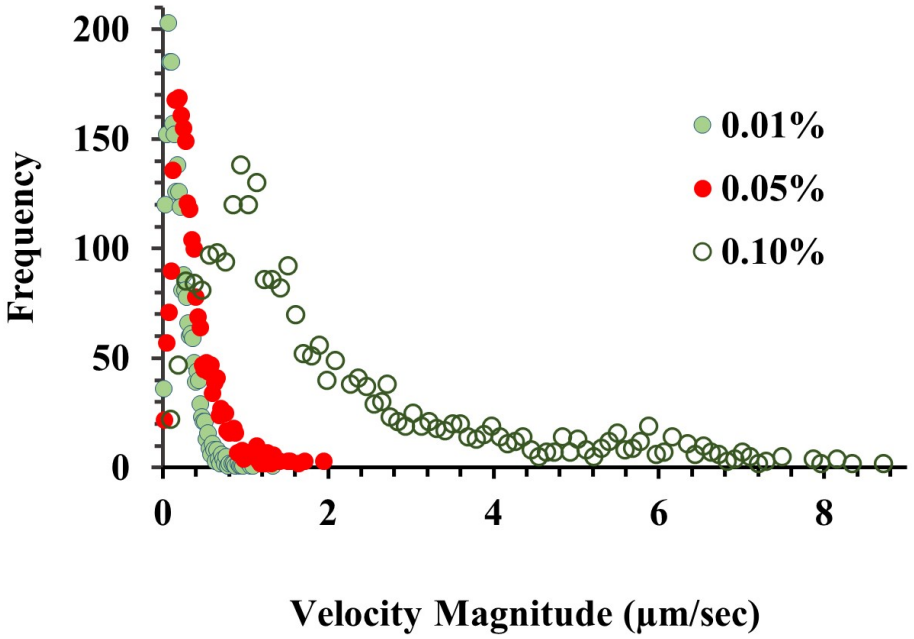

Figure 2.12: Velocity vector histogram for different particle concentration. These plots qualitatively shows that higher particle concentration generated stronger flow relative to the lower concentration. PIV analysis was done for the experiments shown in Figure 2.11 with the same PIV parameter setting for each experiment.

Particle-induced fluid motion (for high concentration) can be regulated by adjusting rotational speed. With the increase of rotational velocity, particle settling orbit decreases, which reduces the amount of displaced fluid per revolution. Further, we

observed particle-particle electrostatic interactions when the radius of the rotating orbit was reduced; in other words, decreasing particle-induced fluid displacement provides long term suspensions with less unintended fluid flow and thus improved observations of interparticle interactions (Figure 2.13).

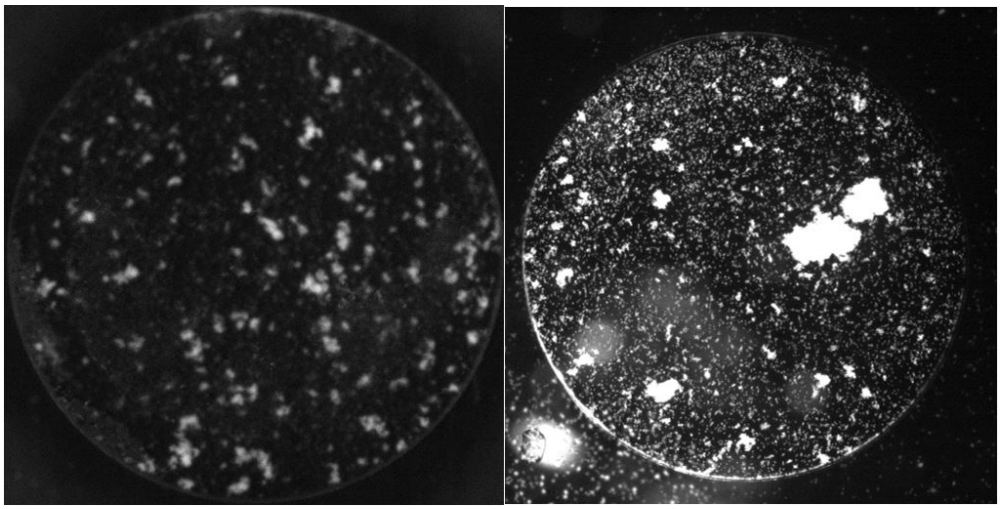

Figure 2.13: 3.62 μm Silica (specific gravity 1.81, 0.1% w/v) particle, sample rotated at 40 rpm (left), calculated radius of circulating orbit for a single particle is 1.55 μm. While this particle concentration (0.1%w/v) generated bulk fluid motion and no aggregation is observed at 10 rpm (Figure 2.11), they were aggregated here (left) while not contributing to bulk fluid motion as seen for low rotational speed (10 rpm). 8 μm Polystyrene particle, sample rotated at 10 rpm, specific gravity 1.05, 0.1% (w/v), and calculated radius of circulating orbit for a single particle 2 μm, formed aggregation (right).

2.3.3 Geometry at the sidewall boundary influences fluid motion

We already noticed that high particle concentrations can induce fluid motion depending on the rotational speed. Particle-induced fluid motion is reflected from the sidewall boundary and increases its magnitude even further. Designing different geometries at the side wall bounary can help suppress fluid motion. In Figure 2.14, the influence of bulk fluid motion from two different configurations at the side wall boundary are shown. Sawtooth boundary suppressed fluid motion

significantly. Primary observation suggests that, at the location of sawtooth side wall, fluid from the bulk and fluid from the sidewall geometry counteract to each other (Figure 2.15) and thus suppressed overall fluid motion. The role of side wall geometry in fluid motion in a confined cell indicates that particles interact with the nearby surfaces. Therefore, beyond primary observation, this further motivated us to look closely the colloidal hydrodynamics near a solid surface (Chapter 3. However, the geometry at the sidewall boundary was not optimized for suppressing motion but is recommended for future work. For the remainder of this dissertation we used straight sidewalls for consistency.

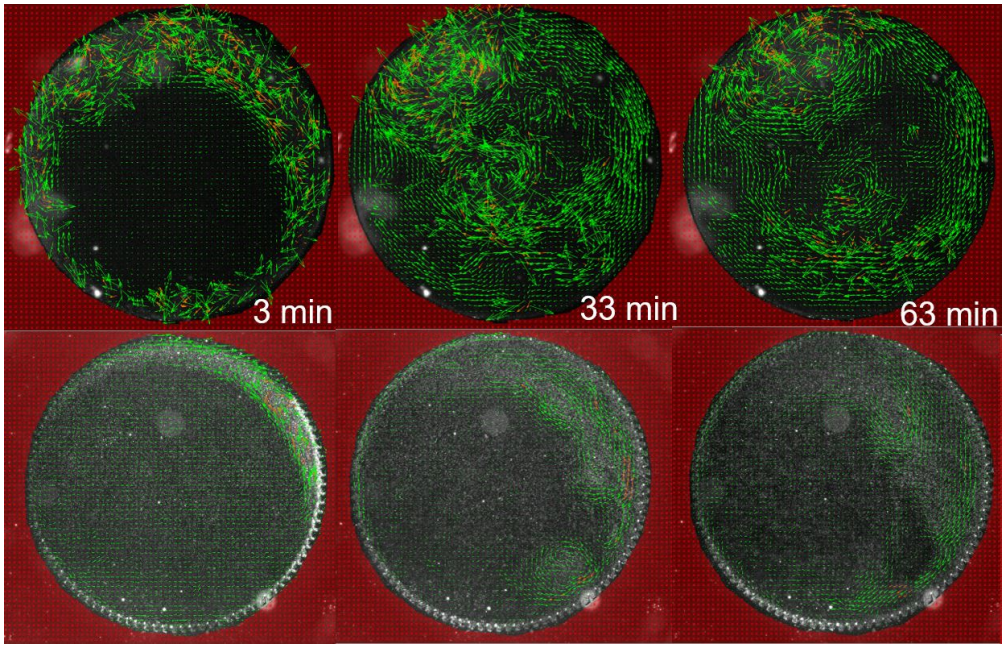

Figure 2.14: Two different experiments were run at the same conditions except that the side wall boundaries were different (top- smooth side wall boundary and bottom-sawtooth shaped side wall boundary as shown in Figure 2.15b). Pointer length of velocity vectors for sawtooth geometry is drawn 2X bigger.

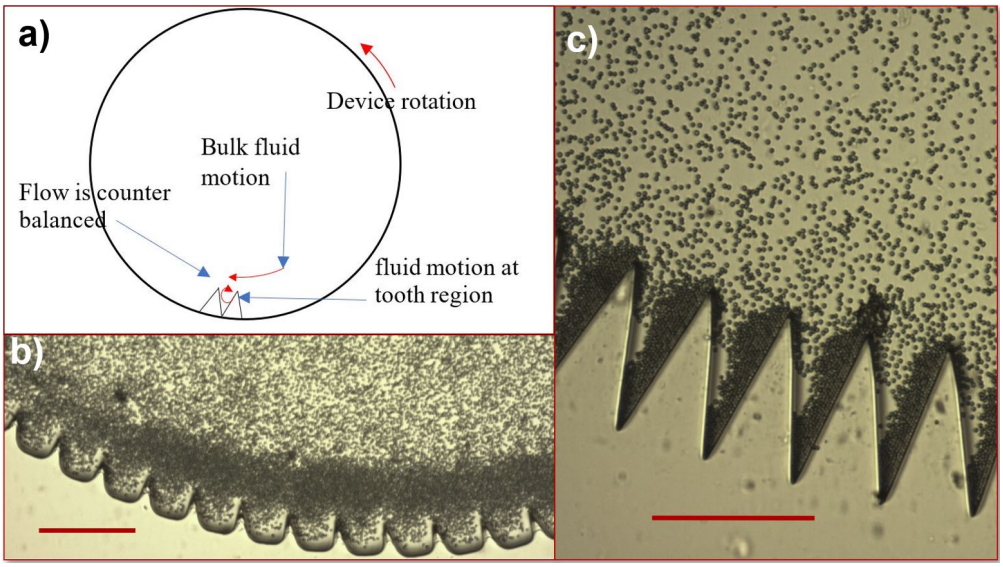

Figure 2.15: a) Flow generated from the bulk liquid and generated at the tooth region are possibly counter-acting and thus suppressing fluid motion. b) and c) We fabricated different side wall geometries and observed that certain geometries (b) are more helpful in suppressing fluid motion than the others (c). Scale bar: 100 µm.

2.4 Particle motion in thermal gradient

While remaining in suspension, particles indeed showed thermophoresis in response to a thermal gradient (Figure 2.16). Particle tracking velocimetry analysis showed that particles moved in the direction of the thermal gradient. A sample cell was placed at the center of rotating axis, but in close proximity to the rotating shaft which has a flat groove on it. The steel shaft was the source of heating due to constant lighting of the sample area. The flat groove-side acted as a colder side on the sample cell resulting in a temperature gradient in the sample cell. Making a similar groove on the other side of that shaft eliminated directional fluid motion. Particles moved towards the colder region following a linear path at 40X slower speed relative to the average sedimentation velocity. Similar results have been observed elsewhere (Toda et al., 1996) in microgravity experiments (using drop

tower).

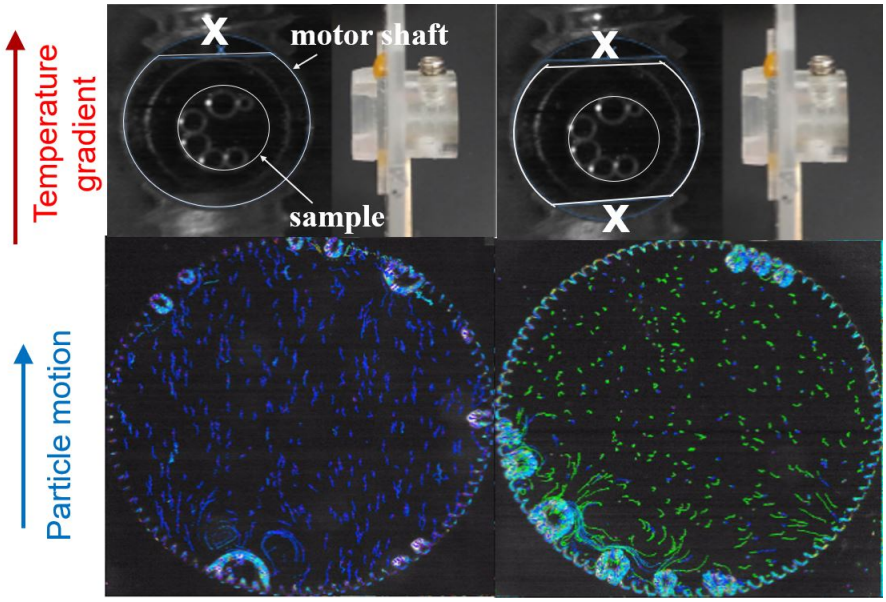

Figure 2.16: 8 μm polystyrene microsphere (Specific gravity 1.05) suspension, sample rotated at 17 rpm. Sample cell was placed at the center of rotating axis, but near to the rotating shaft which has a flat groove on it (marked area by 'x'). This generated a heat gradient in the sample cell. Making similar groove on the other side of that shaft eliminated directional particle motion. Particle migrated from hotter region to colder region along thermal gradient. The average velocity of thermophoretic migration was 0.035 μm/s, while their average sedimentation velocity was measured in the same sample cell as 1.5μm/s.

2.5 Conclusion

Non-dimensional analysis suggested that volumetric fluid displacement is directly proportional to particle concentration and inversely proportional to rotational speed. We made a similar qualitative observation during the device characterization and parameter selection period. The preliminary result suggests that colloidal concentration plays role in collective fluid motion which disrupts the static nature of colloidal suspension. We further found that geometry at the side wall boundary plays significant role in suppressing fluid motion which indicates confinement or underlying surface plays role in colloidal collective behavior. Therefore, it is

important to evaluate colloidal hydrodynamic interactions among particles and nearby solid surfaces from the perspective of microscale fluid dynamics of a single particle's mobility. Due to the complexity of such a non-equilibrium system, computer simulation is necessary to understand the underlying physics, which is explained in detail in Chapter 3. As we observed apparent thermophoresis, we were careful in lighting of the sample cell such that any objects or parts near to the sample cell do not generate thermal gradients.

CHAPTER 3

SIMULATING COLLOIDAL HYDRODYNAMICS

3.1 Introduction

Hydrodynamic interaction (HI) in the Stokes flow regime has long been established theoretically with long range and short range (lubrication) particle-particle interactions. The flow field produced by a particle is approximated by the Green's function and multipole expansion of the particle's surface force density. This is done using Taylor series expansion of the Green's function on the particle surface which produce disturbance field with coefficients of the moments of surface traction (Kim and Karrila, 2013). In getting true disturbance velocity, for particles of irregular shape and to capture short range particle interactions, higher order terms of the multipole expansions are needed. However, translating spheres only require two terms - force monopole and isotropic quadruple (Rotne and Prager, 1969). In multibody HI, this produces an accurate description of long-range particle coordination. However, when particles are in close proximity with each other, additional higher order moment terms are needed to accommodate lubrication interactions (Ladd, 1990; Durlofsky et al., 1987; Brady and Bossis, 1988). Thus,

disturbance flow caused by the mobility of a single particle entrains other particles in suspension. Configuration-dependent mobility matrices couple hydrodynamic force/torque on the particles to their motion relative to the fluid. Through the formulation of grand mobility matrices, while capturing long-range and short range interaction, Stokesian dynamics (SD) simulation technique was developed by Brady and Bossis (1988). SD simulation techniques were subsequently improved (i.e. faster and more efficient) through the work of a number of researchers (Sierou and Brady, 2001; Wang and Brady, 2016; Fiore and Swan, 2019). Other simulation techniques are available for colloidal suspensions, a good review of them is available in literature (Fiore and Swan, 2019; Maxey, 2017; Driscoll and Delmotte, 2019). Because of the complex nature of colloidal suspensions, many different simulation techniques exist, each with their own respective advantages and complex formulations. Here we adopted a simple simulation technique avoiding the so-called hydrodynamic contact forces or lubrication interactions to reduce mathematical complexity. Rather we employed hard sphere collision model that incorporated hydrodynamic and center-to-center repulsion forces due to particles' overlapping. This method can be useful for experimental colloid scientists where seemingly abstract and complex mathematical formulation can be avoided.

A majority of SD simulations focus on Brownian particles in an unbounded system with a few exceptions (Swan and Brady, 2007; Aponte-Rivera and Zia, 2016). The dominant term in the colloids' mobility (Green's function with coefficients of point force- as known as Stokeslet) is long-ranged ($\sim \frac{1}{r}$, where r represents distance from particle's center and $r > a$, where a is particle's radius). Boundary effects also need to be considered where colloids are contained in a bounded medium. Otherwise, as

number of particles increases, simulation results in a severely nonconvergent sum of interactions(Brady and Bossis, 1988). Here we simulate non-Brownian colloid suspension near a no-slip flat plate boundary condition. The disturbance field caused by a Stokeslet near a no-slip boundary is provided by Blake (Blake, 1971) using an image system. In an unbounded system, the velocity field caused by a translating sphere, as mentioned earlier, is presented by a linear combination of a Stokeslet $\left(\sim \frac{1}{r}\right)$ and a (potential) source dipole $\left(\sim \frac{1}{r^3}\right)$. As the source dipole term decays quickly with distance r, resultant wall reflections do not transcend to distant particles. Therefore, the velocity field caused by a translating sphere near a boundary is approximated here as the Stokeslet near a boundary in addition to a source dipole term in an unbounded system.

One of the important properties of Stokes flow is that divergence of stress (usually represented by σ) is zero ($\nabla.\sigma = 0$) enclosing any fluid volume if it does not contain the location where point force (Stokeslet) is applied, which signifies that particles entrained by a Stokes flow do not experience force on its surface ($\int_s \sigma.\hat{n}ds = 0$, where s represents particle's surface). This implies that entrained particles are force-free and will float at the velocity of the flow field located in the center of that particle. As particles move as a rigid body, there is a mismatch of the velocity field on the surface and the velocity field in the fluid medium near the surface, which in turn causes either torque (when $\mathbf{r}$, distance between the moving and the entrained particle, orients perpendicular to the particle's velocity, $\mathbf{v}(\mathbf{r})$), stresslet (when $\mathbf{r}$ orients in the direction of $\mathbf{v}(\mathbf{r})$), or linear combination of torque and stresslet on the particle surface. This can also be seen if we integrate the first moment of force over the entire surface, which can be shown mathematically as

$\int_s (\sigma.\hat{n})\,\mathbf{a}ds \neq 0$, where $\mathbf{a} = a\hat{r}$.

Due to the application of torque and stresslet on that entrained particle it causes a reflected velocity field which, by superposition principle is also known as a method of reflection (Happel and Brenner, 2012)[47], modifies the original velocity field. Unlike the original one, the dominant term of this reflected velocity field is short-ranged $\left(\sim \frac{1}{r^2}\right)$ (Guazzelli and Morris, 2011). Therefore, it can also be stated that rigid particles in suspension contribute to the stress because of the short-ranged torque and stresslet exerted by the fluid on the particles (Kim and Karrila, 2013). To calculate torque and stresslet on an entrained (second) particle, we need to calculate $\int_s (\sigma'.\hat{n})\,\mathbf{a}ds$ over the entire surface which is mathematically cumbersome. Instead of doing this, we can scale torque (as explained in Section 3.1.2) and stresslet from the velocity of the driven particle at the center of the entrained particle. As reflected velocity field caused by the torque and stresslet are short-ranged, we can neglect wall reflection as it is necessary for a Stokeslet. Torque and stresslet, at a distance greater than $2a$, does not change velocity field significantly, as their strength decays as $\frac{1}{r}$ and $\frac{1}{r^2}$ respectively and velocity field caused by them decays as $\frac{1}{r^2}$. We justify these simplifications by employing a particle tracking model from hard-sphere collision dynamics which can capture particles' location while not compromising dynamics due to discarding quickly-decaying reflected velocity field for stresslet.

3.1.1 Single particle mobility due to sedimentation near a solid surface

Our approach primarily focuses for the case where $Pe > 30$, assuming that Brownian motion is not important to preclude sedimentation. Fluid dynamics of particle sedimentation depends on Reynolds number ($Re = \frac{\rho_m U a}{\mu}$). If $Re < 1$ particle motion dynamics is mostly driven by viscous effects. For most colloids, $Re \ll 1$ and hence inertia can be ignored; for our test particles, Re is on the order of 10^{-6}. First part of Equation 1.3.15, $(\mathbf{F} + (\mathbf{F}.\hat{\mathbf{r}})\hat{\mathbf{r}})$, represents a velocity field which is known as Stokeslet, caused by a point force in an unbound quiescent fluid. The second term $\frac{a^2}{3r^2}(\mathbf{F} - 3(\mathbf{F}.\hat{\mathbf{r}})\hat{\mathbf{r}})$ represents fluid field caused by (potential) source dipole separated at a distance a. At large distances the flow field is dominated by Stokeslet where flow decays as $\sim \frac{1}{r}$. Contrary to Stokeslet, the source dipole decays quickly $\left(\sim \frac{1}{r^3}\right)$. Therefore, particle dynamics in Stokes flow regime contributes to long range as well as short range interactions. Due to long range interactions, in many-body-hydrodynamics, increasing the number of particles can mathematically result in an increasing velocity field.

In Stokes flow regime, reversibility and linearity play significant roles in resolving complex problems. Due to its linearity principle, similar solutions from Stokes equation for multiple particles can be added together and the resultant velocity represents the flow field due to multiparticle mobility. As mentioned earlier, with the increasing number of particles, the flow field mathematically diverged to an increased velocity field. However, in practice colloid systems are always contained by solid surfaces. Colloids interact with the solid boundary in the form of long-

range interactions. In 1971, J. R. Blake showed velocity field caused by a Stokeslet near a no-slip boundary through the application of an image system (Blake, 1971). The entire velocity field he wrote, in a form of tensor notation, is as follows

$$u_j^* = \frac{F_k}{8\pi\mu}\left[\left(\frac{1}{r}-\frac{1}{R}\right)\delta_{jk}+\frac{r_j r_k}{r^3}-\frac{R_j R_k}{R^3}+ 2h\left(\delta_{k\alpha}\delta_{\alpha l}-\delta_{k3}\delta_{3l}\right)\frac{\partial}{\partial R_l}\left\{\frac{hR_j}{R^3}-\left(\frac{\delta_{j3}}{R}+\frac{R_j R_{j3}}{R^3}\right)\right\}\right] \tag{3.1.1}$$

where the initial point force (F_k) is located at $(y1, y2, h)$, the image at $(y1, y2, -h)$, as shown in Figure 3.1, and $r = \sqrt{(x_1-y_1)^2+(x_2-y_2)^2+(x_3-h)^2}$ and $R = \sqrt{(x_1-y_1)^2+(x_2-y_2)^2+(x_3+h)^2}$

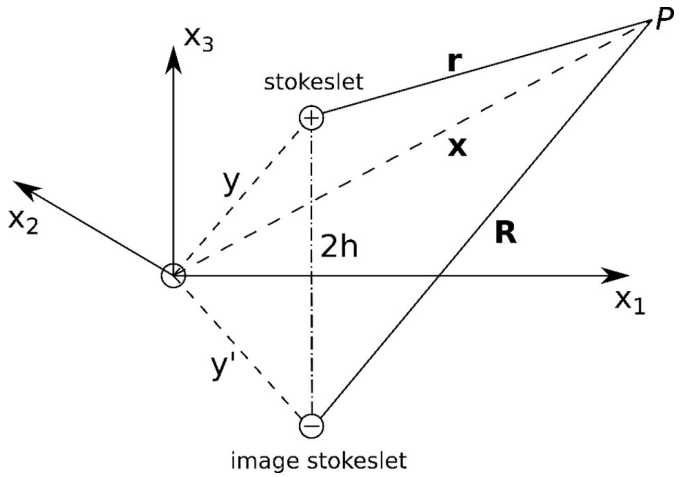

Figure 3.1: The position of stokeslet and image stokeslet, and relevant distance vectors x, r and R. Wall is situated at $x_3 = 0$. Image is reproduced from (Blake, 1971)

Isolated Stokeslet in an infinite viscous fluid ($r \ll h$) is preserved from Equation 3.1.1 and thus it is converged to the expression as denoted by the first part of Equation 1.3.15. However, the outer-field (away from the particle) is modified considerably by the presence of wall and no slip boundary ($u_{x_3=0} = 0$) is ensured at the wall. By combining right side of Equation 1.3.15 (i.e. the source dipole term) to Equation 3.1.1, we can get the velocity field caused by a moving spherical

particle in a practical application (such as near a solid surface). In the far field this combination reflects correctly and does not pose any error. However, for particles locating very near to the boundary, the no slip condition is slightly violated. As the source dipole term decays quickly, this error is not commuted at greater extent, rather override by the Stokeslets due to the presence of many particles. In Section 3.1.3, we show an attempt to minimize this error.

3.1.2 Torque and stresslet approximation, caused by fluid disturbance

This section could be important for the case of dense bimodal or polydisperse colloid suspensions with higher aspect ratio. Disturbance flow caused by a translating sphere can exert either torque or stresslet on the entrained particle, or in linear combination of both, depending on the position of the entrained particle (Figure 3.2). As entrained particles are forced free, they float with their center-point velocity. Particles translate like a rigid body such that every point of the particle translates at the same velocity. Therefore, there is a discontinuity of the velocity at the surface from liquid to the solid. This discontinuity would naturally cause particle rotation (and hence rotational velocity field) and straining motion. This reflected velocity field is short ranged as their leading order term decays as $\frac{\mathbf{1}}{r^{\mathbf{2}}}$ (Guazzelli and Morris, 2011) and the strength of torque and stresslet decays as $\frac{\mathbf{1}}{r}$ and $\frac{\mathbf{1}}{r^{\mathbf{2}}}$ respectively. Therefore, for a dilute suspension, these force moments do not add significant contribution especially when long-range velocity field is already counted from many-body interactions. However, we show here how to add these

reflected velocity fields caused by the force moments from the disturbed flow. In the following paragraph, we focused on the torque and thus neglected the stresslet due to its complexity and irrelevance for our case.

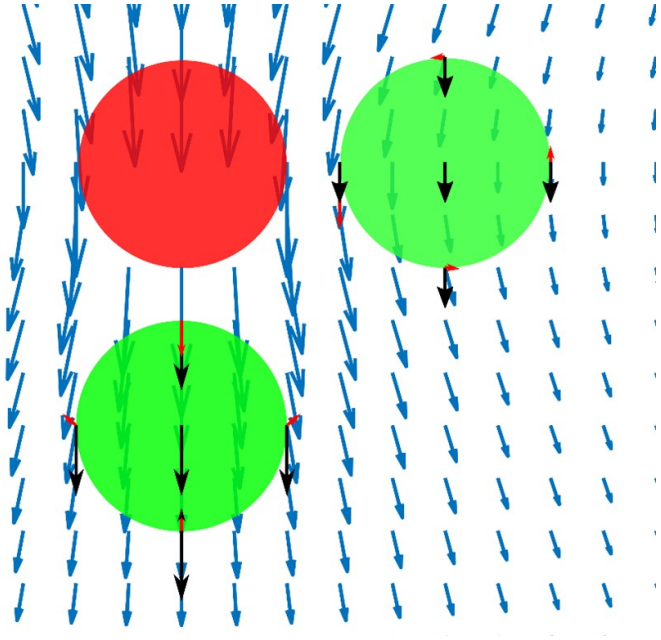

Figure 3.2: Flow field caused by a translating red particle is shown here as the blue arrows. When the distance between translating particle and an entrained particle (green sphere, top right) is perpendicular to the direction of translating particle's velocity, fluid exerts torque on the entrained particle which causes rigid body rotation. When the distance between the translating particle and an entrained particle (green sphere, bottom) is along the direction of translating particle's velocity, fluid exerts stresslet to the entrained particle. Due to the particles' rigidity, they are unable to be sheared and thus cause a reflected velocity field. For other locations, stresslet and torque are in linear combination.

The velocity field caused by individual rotating particles may be included with the total velocity field. However, calculating the rotational flow field in that manner is nontrivial and computationally costly. Instead, we can scale particle rotational motion as $\omega = \frac{\hat{\mathbf{r}} \times \mathbf{V}(\mathbf{r})}{a}$ (see Appendix), where $\mathbf{V}$ is the velocity at the entrained particle caused by the driven particle. Once we know angular velocity of the entrained particle, we can get the modified velocity of the driven particle from the following equation (Guazzelli and Morris, 2011)

$$\mathbf{V'}_{r=\mathbf{0}} = V_{r=\mathbf{0}} + \frac{a^3}{r^3}(\omega \times \mathbf{r}) \tag{3.1.2}$$

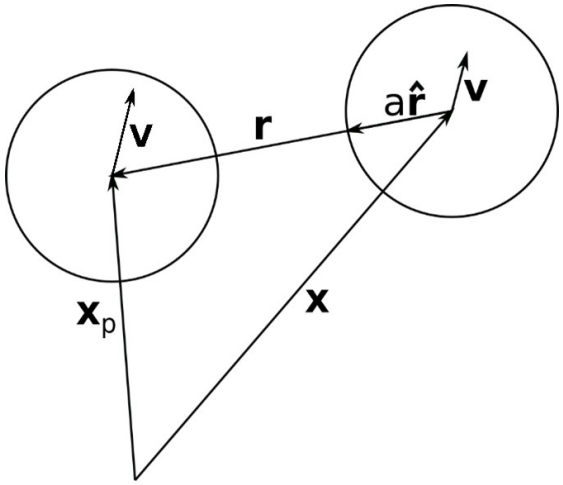

Figure 3.3: X_p and X represents the position vectors of the driven and the entrained particles respectively. Depending on their position, the entrained particle may cause stress on the fluid which can modify driven particle's velocity.

3.1.3 Wall effect on short-range velocity field

For particles near to the boundary, the velocity field due to short range source dipole (second term of Equation (1.3.15) and rotation caused by other nearby particles may need to be corrected due to the presence of the boundary. As these velocity fields are short ranged, instead of considering true physics (image reflection due to rotlet and source-doublet singularities (Swan and Brady, 2007; Blake and Chwang, 1974), we took a simplified approach using a linear velocity-drop near the boundary, as shown in following equation and in Figure 25.

$$\mathbf{V}_{short-range,\ \ wall} = \mathbf{V}_{short-range}\frac{x_3}{2a} \tag{3.1.3}$$

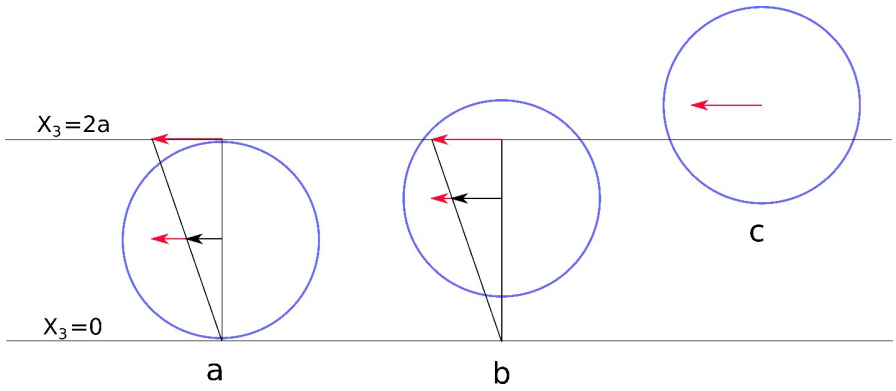

Figure 3.4: Red arrow indicates velocity, due to short range source dipole and rotation caused by other near-by particles, at the particle's center. Particle's short-range velocity is modified, as shown in black arrow, when they are within $2a$ distance from the boundary (a, b). Boundary effects on short-range velocity is not counted for particles away ($X_3 > 2a$) from the boundary (c).

3.1.4 Hard-sphere colloid mobility model

In Stokes flow, fluid dynamics is governed by the viscous effect. Therefore, momentum diffuses momentarily and such error, due to mathematical approximation, does not propagate throughout the simulation time. However, particle distribution at a certain moment is important. Therefore, it is imperative to track correct particle location. In our test system we assumed colloids are hard spheres – they are not deformed due to interparticle collisions. Without incorporating a hard sphere model, numerical addition of vector fields due to hydrodynamic interaction alone will cause particles to overlap with each other, significantly altering the true colloid mobility. If colloids invade each other, short-range velocity term becomes dominant. Therefore, approximation, as described earlier, is not going to be helpful. Before running each simulation, the particles' positions need to be adjusted. Here we adopted a hypothetical idea of repulsion. First, in our numerical solution scheme, we allowed particles to overlap each other. Whenever center-to-center dis-

tance among particles is less than $2a$, we assumed that they would repel each other with a certain repulsion force, (say $\mathbf{F}_p = -\mathbf{F_1}$) to require their center-to-center distance to become $2a\hat{\mathbf{r}}$, refer to Figure 3.5. These repulsion forces are balanced by hydrodynamic drag forces. Therefore, we can write as $6\pi\mu\mathbf{U}_p a_p = -6\pi\mu\mathbf{U}_1 a_1$. As particles are equal size, this equation turns to $\mathbf{U}_p = -\mathbf{U}_1$. Further, this event's time-step is constant for both particles and therefore $\mathbf{r}_p = -\mathbf{r}_1$. The total distance among particles, after particles' displacement, is $\mathbf{r}_p + \mathbf{r} - \mathbf{r}_1 = 2a\hat{\mathbf{r}}$. By solving $\mathbf{r}_p$ and $\mathbf{r}_1$, we can get position vector $\mathbf{X}'_p$ and $\mathbf{X}'_1$.

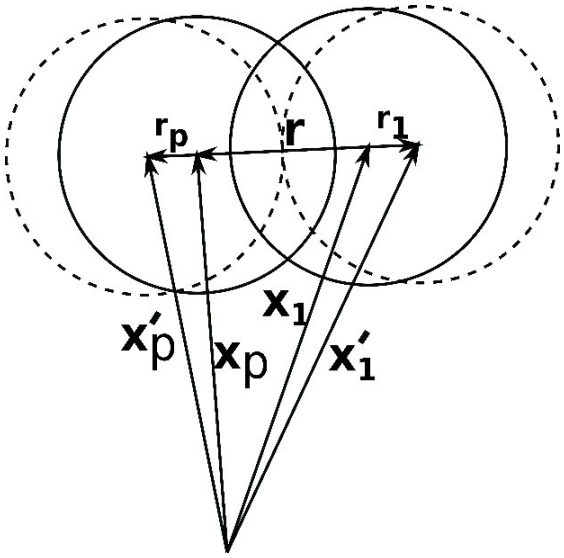

Figure 3.5: Solid line represents particle's position before hard-sphere model is applied, while dotted line shows position after displacement.

In sequential computation, we first select a particle. We then find particles that are within the neighborhood of $3a$[1]. radial distance from that test particle. Within that neighborhood, we calculate center-to-center distance from the test particle. We sort them from lowest distance to highest. Using the above-mentioned process, we reposition the test particle while checking overlapping among all the particles

[1] $2a$ distance may be enough, however, during iteration process particles little away from $2a$ distance may enter into the neighborhood which may remain missing. Increasing the neighborhood size further will simply add computational cost.

in the neighborhood. This process continued for each individual particle. It is worth mentioning that during particles' relocation process, we do not count the velocity field caused by that relocation process; for a small-time step, we believe this is not necessary. For a very dense particle concentration and larger time-step, adding velocity field caused by particle relocation due to hard-sphere mobility may be needed.

3.1.5 Sidewall Boundary effect

The sample cell consists of two parallel surfaces, which are separated by a cylindrical sidewall. Particles initially reside near one of the two parallel surfaces. The distance between the two surfaces are such that the other parallel surface does not impose significant resistance to the colloids' mobility. However, particles near the peripheral boundary reside close to two side walls;: the underlying side wall and the sidewall perimeter. In this scenario, it is important to consider near-wall as well as side-wall effect in colloidal fluid motion. However, considering multiple wall effects is nontrivial. Therefore, for the simulations we assumed an 'infinitely' long substrate such that there are negligible sidewall interactions. However, we count sidewall-affected-reduced-force on the particles (which is described later in this section) and keep particle positions confined within the side-wall boundary.

The sample cell on our experimental device is considerably big (3 mm diameter) compared to the simulation space size (0.36 mm diameter) because of computational cost. For a constant particle density within the numerical simulation, number of particles increases as A^2, where A represents radius of the sample cell.

Therefore, simulating the exact device size (3 mm) would produce a relatively long simulation time. To overcome these difficulties, we worked with a smaller simulation space while relaxing the sidewall boundary effect. We believe that keeping the experimental device smaller would alter the observed dynamics due to sidewall boundary effects. However, as side-wall boundary effect is relaxed in the simulation, results from simulation should reflect results from the experiment.

In physical terms the sidewall boundary has two effects on fluid motion. First, it applies additional resistance on particle motion depending on where the particle is located from the side-wall boundary. Second, because of the effect of sidewall boundary, the surface boundary 'views' a reduced force on the particle. Therefore, the computed velocity field (Section 3.1.1) needs to include modified forces on each particle. As the sidewall imposes resistance and reduces forces on the particles, it also causes reflection of the velocity field caused by the particle. Dealing with the two image Stokeslets (reflection from the nearby surface and reflection from the sidewall) can alter no-slip boundary condition on both walls. The surface boundary effect is prominent for all particles (except for those which are very close to the side-wall boundary) when the sidewall boundary is quite large. Therefore, here we count one image Stokeslet which is caused by the nearby surface boundary. However, to account for sidewall boundary effects on these forces (especially on particles which are very close to the boundary), we consider reduced forces on the particles which is described below.

Considering image system (as described in Section 3.1.1), particle mobility, due to Stokeslet perpendicular to the wall, can be shown as $V_{\perp} = \frac{1}{6\pi\mu a}\left(1 - \frac{9a}{8h}\right) F_{\perp}$ and, for Stokeslet oriented parallel to the wall, can be shown as $V_{\parallel} = \frac{1}{6\pi\mu a}\left(1 - \frac{9a}{16h}\right) F_{\parallel}$

(Furst and Squires, 2017). Because of the sidewall effect, particle mobility is reduced. Reduced mobility causes reduced force ($F_{\perp,\ reduced} = 6\pi\mu a V_{\perp}$) on the fluid which is 'viewed' by the nearby parallel surface. Therefore the reduced force for both parallel and perpendicular orientations can be written as $F_{\perp,\ reduced} = \left(1 - \frac{9a}{8h}\right) F_{\perp}$ and $F_{\parallel,reduced} = \left(1 - \frac{9a}{16h}\right) F_{\parallel}$. This modification will significantly affect particles that are very near to the sidewall boundary. Gravitational forces on each particle acts on xy plane, as shown in Figure 3.6. For each particle, coordinate transformation is needed to get force component in perpendicular $(F_{\perp})$ and in parallel $\left(F_{\parallel}\right)$ direction to the sidewall. After obtaining reduced forces due to the sidewall boundary, coordinate transformation is again needed to get the reduced force component in the x and y directions.

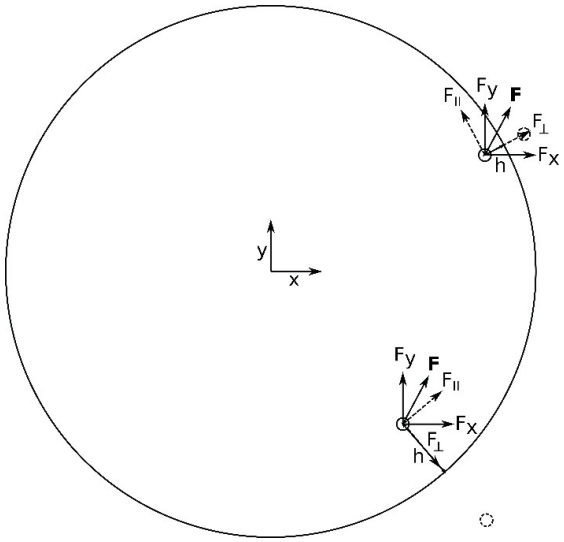

Figure 3.6: **F** represents gravity force. As gravity force vector rotates, it can direct any direction on xy plane at any instant of time. Here h represents radial distance from particle's center to the side-wall boundary.

3.2 Methods

3.2.1 Non-overlapping particle distribution

To verify the simulation with the experiments, we formulated the simulation the same way as we conducted the experiment. In our experimental procedure, particles settled on the surface during sample loading. Therefore, within a simulation space, particles were placed randomly against the surface. Here, the x-y plane is parallel with the solid boundary and the z axis is normal to this plane. Thus, the starting z coordinate for each particle is the particle's radius (as shown in Figure 3.7, left). Using the model of hard sphere colloid mobility (as explained in Section 3.1.4), particles are pushed away (along their center-to-center line) until they do not overlap to each other (Figure 3.7, right). For a higher concentration of colloids, some particles may stay on top of the other particles. In some higher concentration cases, the initial z-coordinates of the particles were randomized within a specific range ($a < z < 1.25a$ distance).

For two particles, we observe this flow field as a pair-wise interaction. For many particles interacting with the said driven particle, we can get the resultant velocity due to rotational effects by adding all $\frac{a^3}{r^3}(\omega \times \mathbf{r})$ terms to the velocity of the driven particle. As being short range (diverges as $\sim \frac{1}{r^3}$), wall reflection for rotation can be ignored for those particles located away from the wall. A point to note here is that here we count rotation due to near-by particles' mobility, however, we don't track particle's rotation.

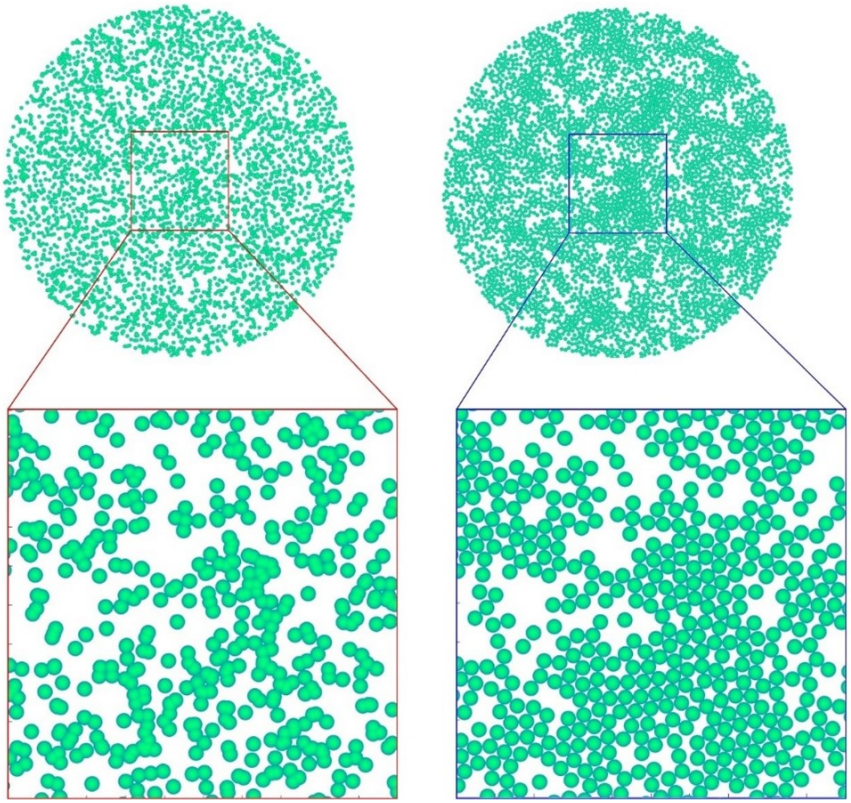

Figure 3.7: (Left) Particles' x and y coordinates are chosen randomly. They can be overlapped to each other. (Right) Using hard-sphere mobility model (as explained in Section 3.1.4), particles are spaced, after 100 iterations, so that they do not overlap each other and stay on the surface. Diameter of the simulation space is 360 μm.

3.2.2 Computer simulation

We developed the following simulation code in MATLAB. The entire mathematical consideration for the simulation process with thorough explanation of every detail of the procedure is discussed before (the component wise each equation is provided in Appendix A). In brief, first the sedimentation velocity of each particle was calculated. Velocity of each particle was multiplied by the simulation time step to determine the particles' displacement during that interval. To adopt undeformed colloid interaction, a hard-sphere model was adopted. First, an individual particle

was selected. We then find particles that are within the neighborhood of $3a$ radial distance from the chosen particle. Within that neighborhood, we calculate center-to-center distance from the test particle. We sort them from lowest distance to highest. Using the process as mentioned in Section 3.1.4, we reposition the test particle while checking for overlap among all adjacent particles. This process continued for each particle. After repositioning, gravitational force on each particle was rotated at -6 degrees (in anticlockwise rotation of the device, force vectors rotated in clockwise pattern and vice versa), which provided a time step of 50 ms (when rotational speed was 20 rpm) and this process continued. Once the gravitational force vector returns to the original orientation (at 0 degree), all of the particles' positions were recorded. This iterative cycle continued throughout the simulation time. The process is illustrated in the flowchart (Figure 3.8). Using MATLAB 2013a and using cluster parallel computing facilities, one rotational cycle took around six minutes for 4500 microparticles. In another simulation cycle, a different rotational scheme (360° counter-clockwise rotation at 20 rpm, stopped for 0.2 seconds, 180° clockwise rotation at 20 rpm, stopped for 0.2 seconds, 360° counter-clockwise rotation at 20 rpm, stopped for 0.2 seconds, 180° clockwise rotation at 20 rpm, and stopped for 0.2 seconds) was employed.

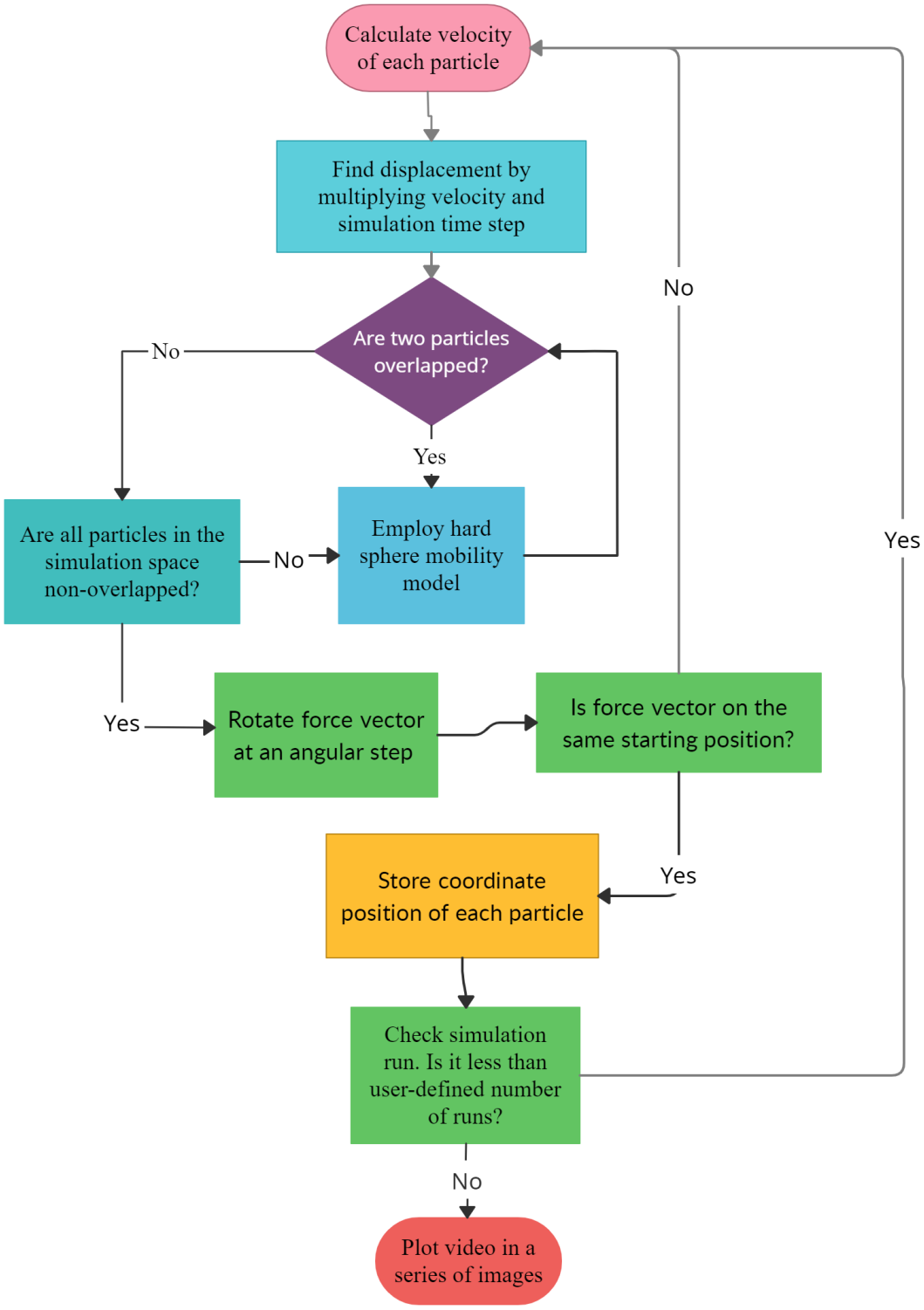

Figure 3.8: Flow chart of each step on the simulation process, as described in Section 3.2.2.

3.3 Results

3.3.1 Role of contact forces in simulation

Adopting hydrodynamic contact forces or lubrication interaction in simulating colloidal interaction is crucial. As distance between neighboring particles' coordinates become very smaller ($r << a$), higher order short-ranged interaction ($\sim \frac{1}{r^3}$) becomes dominant resulting in non-convergent sum of higher velocity magnitude. Particles overlapping each other is non-physical and thus alters the dynamics significantly, as shown in Figure 3.9. Adopting contact forces is challenging and mathematically cumbersome as explained in Section 3.1. We also believe that contact forces or lubrication interaction in colloidal hydrodynamics is not as physically intuitive as something like electrostatic interaction. Rather particles do not cross each other due to excluded volume principle. Therefore, we adopted a hard-sphere mobility model as explained in detail in Section 3.1.4. One of the advantages of this model is that, we track pair-wise particle interaction at a distance not less than at $2a$ which helps in approximating higher-order short ranged reflected velocity field such as torque and stresslet.

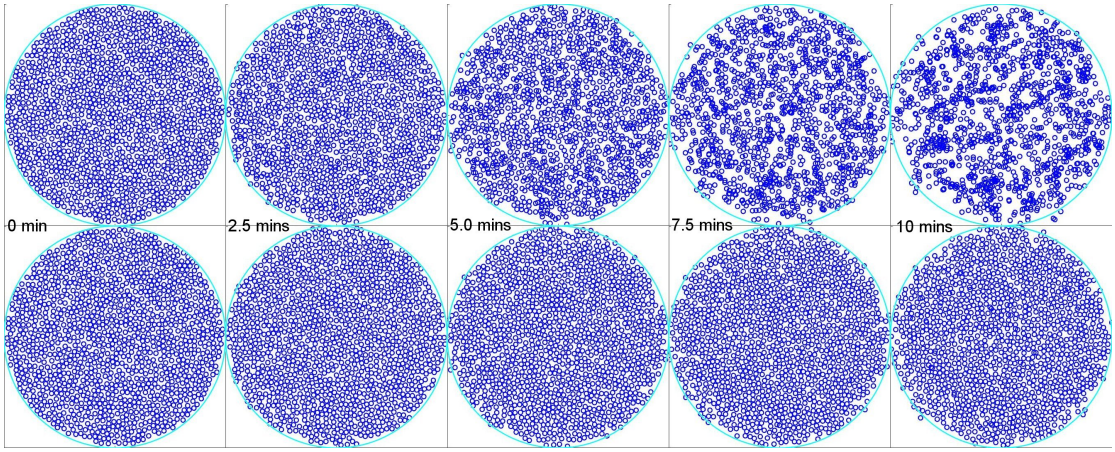

Figure 3.9: (Top row) Simulation of colloidal hydrodynamics without hard-sphere model. As particle overlapping to each other, which is non-physical, they quickly converge high magnitude velocity and keeps trapping of the particles. (Bottom row) Hard-sphere mobility model represents actual dynamics. Here, particles are non-overlapped allowing them to move out of plane in case of collision or 'contact forces'.

3.3.2 Colloidal mobility in one rotation

We observed previously (Section 2.1.2 and 2.3.2) that concentrated colloids generates higher fluid velocity compared to lower-density colloidal suspensions. We demonstrate similar observations through simulations. As colloids aggregate, they also migrate away from the surface, resulting in constructive interference in fluid flow while decreasing interference in side wall effect. As a result particles collectively move faster than they would move individually in the suspension. Here, we observed colloidal aggregates translating in a circular orbit in one single rotation (Figure 3.10). Additional simulations were conducted where the particle height from the surface was varied (Figure 3.11). Here, their orbits (shown by blue or cyan circles) increase with distance from the surface. Thus, the particle's trajectory is retarded as it gets in close proximity to the wall.

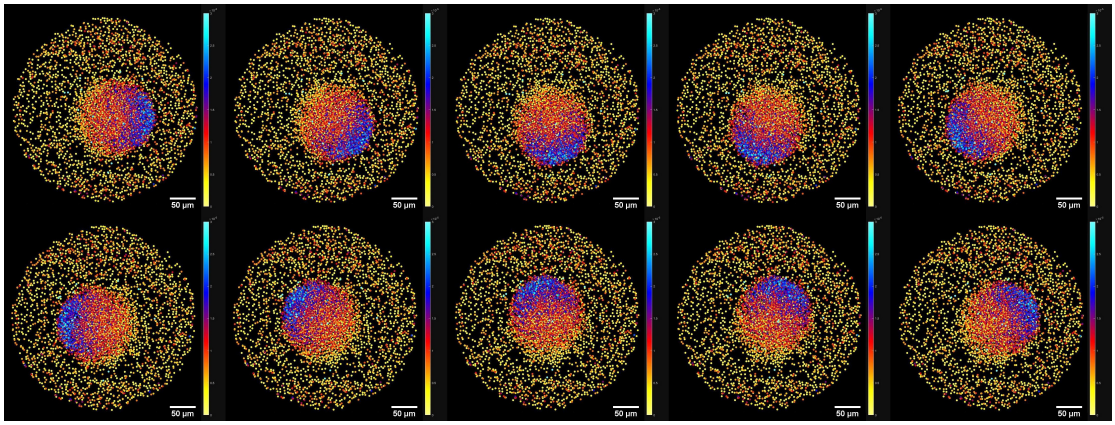

Figure 3.10: Collective motion for colloidal aggregates which formed around 50 mins later from running simulation experiment. 20 rpm uniform rotation counterclockwise formed colloidal clusters. 0.56% (v/v) hard-sphere (specific gravity 1.22, particle diameter 4 μm) solution in DI water initially were distributed at the surface. Image is progressing from left to right and top to bottom. Total time: 6 seconds. Color bar represents lateral migration where yellow color represents 2 μm distance from the surface while cyan color represents 30 μm from the surface.

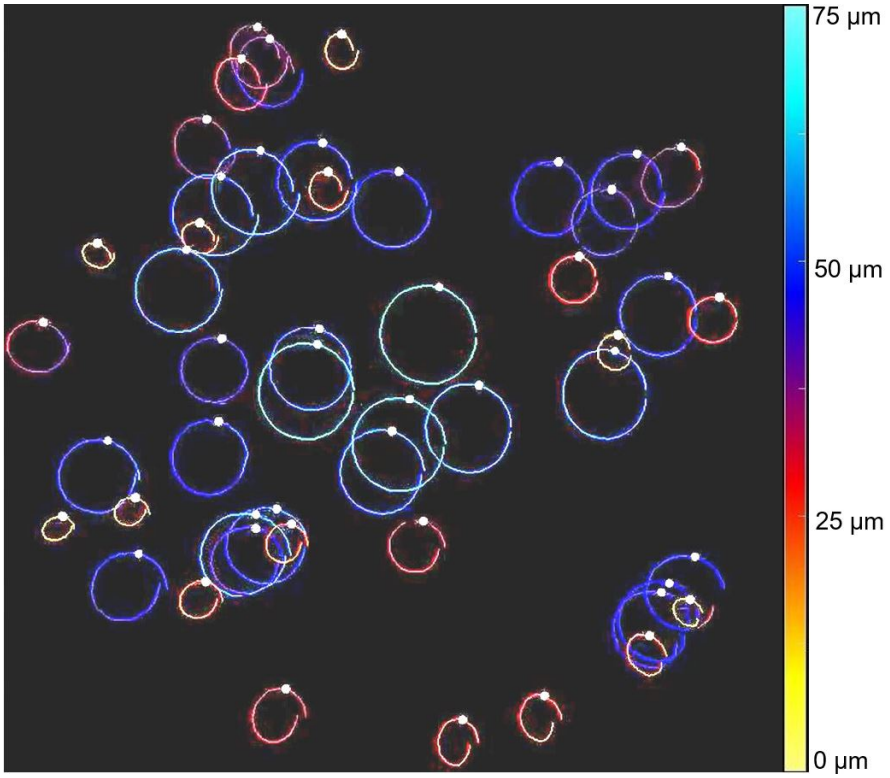

Figure 3.11: 4556 (3 μm PMMA) microparticles are moving in water due to rotational gravity in a cylindrical cell (430 μm diameter by 150 μm height). 50 microspheres were chosen to show their motion. Particles moving faster are in the middle of the cell (orbit shown by cyan color) and particles moving slower either reside near either of the two walls or at the boundary. Color bar shows distance of the particle from one of the side wall.

3.3.3 Colloidal cluster formation

At the beginning of the simulation, randomly distributed same-sized colloidal microspheres started adjacent to one of the two surfaces of the confinement. Over time they formed dynamic collective structures. During uniform rotation at 20 rpm, they first formed patches of structures (clusters) and then those structures collided forming a bigger structure which grew even further, as shown in Figure 3.12. While forming structures they also migrated away from the surface contributing to higher flow velocity. Thus, we realize the underlying side-wall effect on the collective motion of the particles.

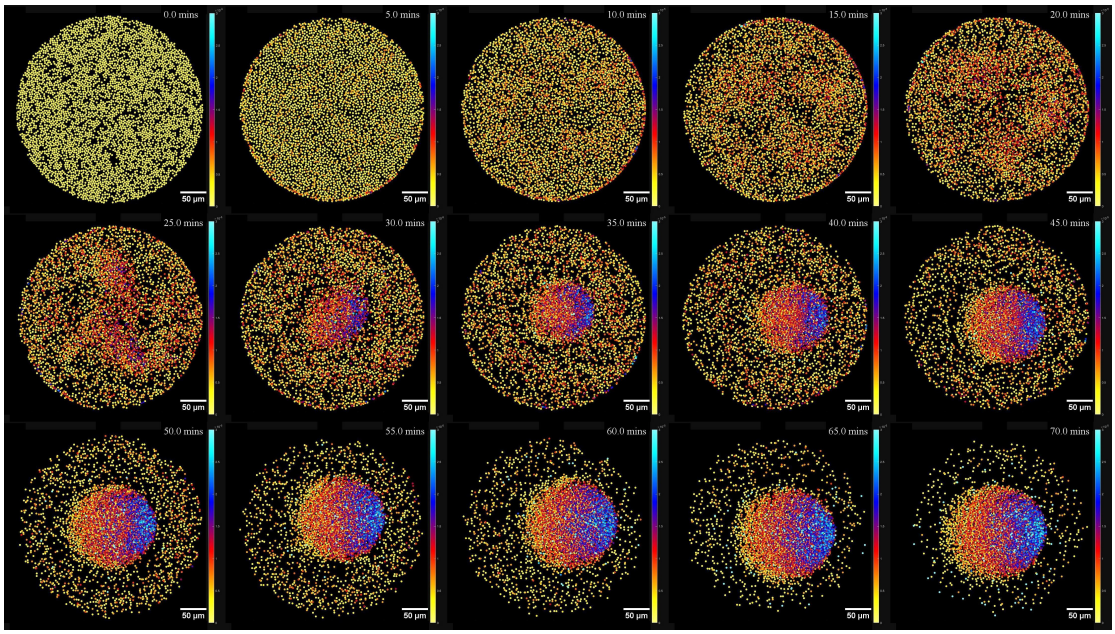

Figure 3.12: Particles were initially distributed at the surface. With vertical rotation, over time colloid aggregated and formed clusters while migrating away from the surface. The aggregated structures also collided to each other. Image is progressing from left to right and from top to bottom. Images are shown at 5 mins interval. Total time: 70 mins. Color bar represents lateral migration where yellow color represent 2 µm distance from the surface while cyan color represents 30 µm from the surface.

3.3.4 Colloidal lane formation

Employing a different force pattern on colloidal microspheres, we observed a different structure pattern. We employed a complex rotational gravity force field, as described in Section 3.2.2. We observed the formation of lane like structures, as shown in Figure 3.14. Particles joined in forming lanes at several layers in height while leaving non-colloidal zones.

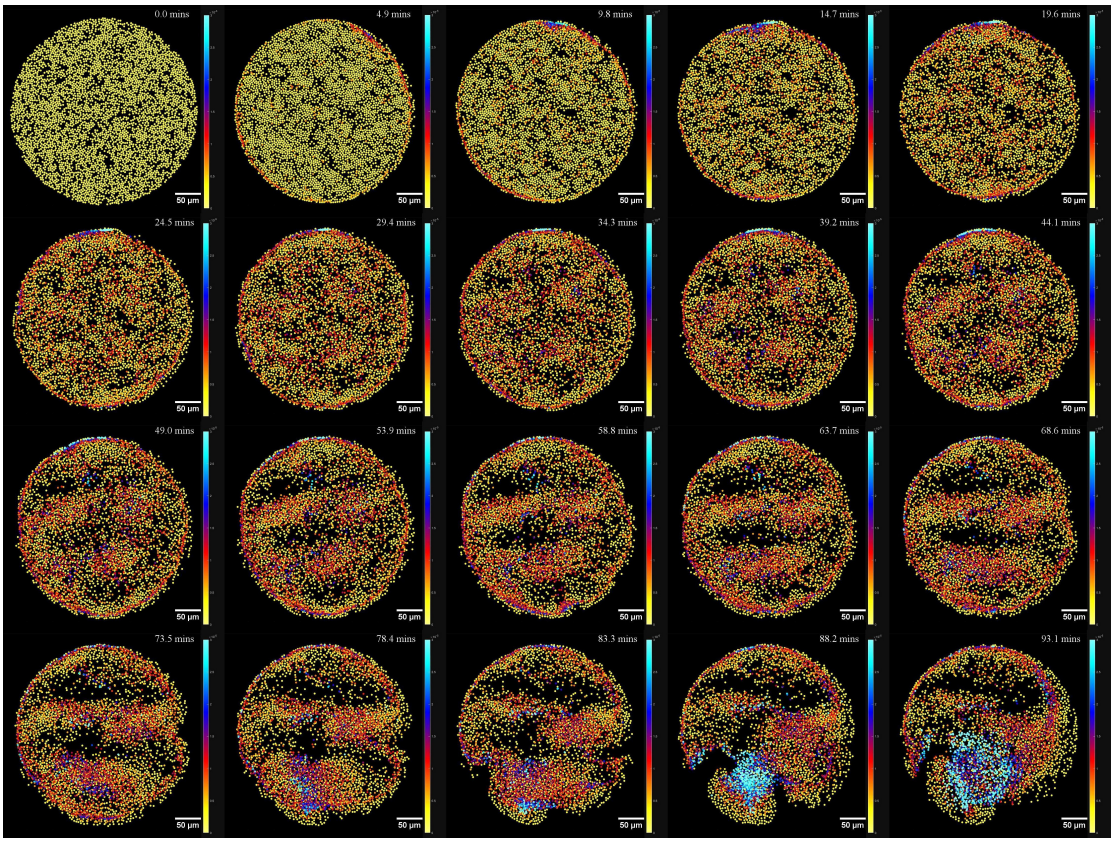

Figure 3.13: Sample cell was rotated with a complex rotational scheme as described in Section 3.2.2 which formed lane like dynamic structures. 0.56% (v/v) hard-sphere (specific gravity 1.22, particle diameter 4 μm) solution in DI water initially were distributed at the surface. Image is progressing from left to right and from top to bottom. Images are shown at nearly 5 min interval. Total time: 93 min. Color bar represents lateral migration where yellow color represent 2 µm distance from the surface while cyan color represents 30 µm from the surface.

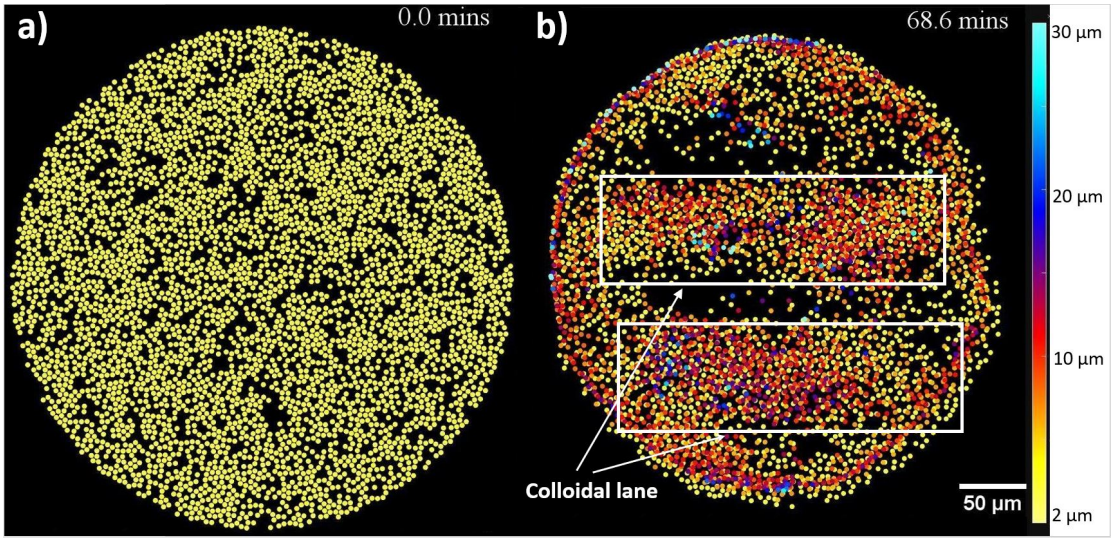

Figure 3.14: Colloidal lanes are further highlighted by white rectangles. Lanes are separated by colloid free zones. (a) Colloids were initially distributed on the surface. (b) After around 70 mins later, colloid lanes formed and migrated away from the surface. Color bar represents particle distance from the underlying surface.

3.4 Conclusion

Here, we avoided hydrodynamic 'contact forces' which is mathematically tedious and physically non-intuitive. The nearest velocity we tracked at $2a$ distance from the entrained particle which was helpful in eliminating short-ranged and higher-ordered reflected velocity field. Instead, we adopted hard-sphere mobility model where particle's true location was tracked by balancing center-to-center repulsion forces due to excluded volume and hydrodynamic drag forces. As our simulation is constituted by adopting model and mathematical approximation based on intuitive physical understanding at microscale interaction, which is outlined in detail in this chapter, we give importance to validate our approach through experimental consideration. Therefore, further results of our simulation are discussed in Chapter 4 where the same set of experiments are run to confirm the simulations. We further

explored different colloidal suspensions with varying concentrations in Chapter 4. While discussion in Chapter 2 gave us qualitative understanding of the system, simulation provides validation of those understandings while facilitating in-depth understanding such as role of force pattern and side wall in rotational colloidal suspension.

CHAPTER 4

EXPERIMENTAL VALIDATION OF SIMULATED STRUCTURES

4.1 Introduction

Pattern formation, collective behavior, and functional characteristics out of a non-equilibrium colloidal system are commonly seen for a wide range of applications. Self-assembled colloid structures can be formed through the manipulation of chemical signaling (Theurkauff et al., 2012), protein mediated microtubules movement (Surrey et al., 2001), capillary forces (Aizenberg et al., 2000), droplet evaporation (Bhardwaj et al., 2010), electric fields (Vissers et al., 2011; Yan et al., 2016), magnetic fields (Pham et al., 2017), optics (Palacci et al., 2013; Altemose et al., 2020), acoustics (Ahmed et al., 2017) and so on. In all self-assembly cases, hydrodynamic interactions, in addition to the applied external stimuli, play a critical role in colloid manipulation. However, using hydrodynamic interparticle interactions alone for self-assembly has not been as extensively studied. Some examples

Chapter 4 reflects accepted work in the Journal of Colloid and Interface Science entitled as *Cyclic force driven colloidal self-assembly near a solid surface*, Volume 607, Part 2, 2022,Pages 1402-1410, ISSN 0021-9797

of hydrodynamic-guided self-assembly include the formation of line patterns for liquid-merge granular materials on a substrate using horizontal vibration (Sánchez et al., 2004) and a recent study on unstable fronts and motile structures formation using magnetic microrollers (Driscoll et al., 2017). Hydrodynamic interactions are critical in predicting active colloid behavior where external forces are used for controlled motion or forming static structures. Many living cells such as bacteria form collective dynamic structures(Wensink et al., 2012), including vortex arrays (Riedel et al., 2005), on surfaces. Here we developed a new avenue of dynamic structure formation through the manipulation of gravitational effects on the colloids by employing different rotational scheme. In addition to the numerical simulation, we devised an experiment to explore colloid structure formation near a solid surface using a cyclic force pattern. Here we used rotational gravity force with respect to the sample cell's reference frame by rotating the sample cell at low speed so that centrifugal forces are negligible relative to gravitational forces. Colloid structure formation predicted by the simulation is reflected through our experiment. By altering the force pattern cycle, different types of dynamic structures were formed, and underlying colloidal hydrodynamics were validated through the simulation. Evolution rate of dynamic structure formations were modulated by using different particle concentrations.

In addition to the numerical simulation, we devised an experiment to explore colloid structure formation near a solid surface using a cyclic force pattern. Here we used rotational gravity force with respect to the sample cell's reference frame by rotating the sample cell at low speed so that centrifugal forces are negligible relative to gravitational forces. Colloid structure formation predicted by the sim-

ulation is reflected through our experiment. By altering the force pattern cycle, different types of dynamic structures were formed, and underlying colloidal hydrodynamics were validated through the simulation. Evolution rate of dynamic structure formations were modulated by using different particle concentrations.

4.2 Methods

4.2.1 Colloidal solution preparation

Through the careful consideration as discussed in Section 2.1.1, we chose 4.0 µm poly(methyl methacrylate) (PMMA) microspheres ($\rho = 1.22\ g/cc$) from Sigma-Aldrich (Product number 73371, 10% solids, coefficient of size variance <3%, std dev $< 0.15\ \mu m$, surface is negatively charged). Microsphere solutions, without further washing from supplier's product, were diluted in DI water with a concentration of 0.1%, 0.5%, 1.0% and 3.0% (v/v). 10 mM Sodium Dodecylsulfate (SDS, from Sigma-Aldrich, 98.5%, Product L3771) was added in the solution to further enhance electrostatic repulsion among PMMA microspheres and to prevent sticking of the particles to the PDMS surface by ensuring SDS adsorption saturation on surfaces (Li et al., 2013; Khademi et al., 2017). The range of electrostatic repulsive force between microsphere, in an aqueous medium, is typically on the order of nanometers (Choi et al., 2019; Pantina and Furst, 2004) which is extremely local compared to particle size. Furthermore, this is an active colloid system and non-Brownian, where sedimentation velocity dominates particle movement (Peclet number is approximately 35). Therefore, microspheres are con-

sidered as hard spheres in our simulation. Particles were examined under the microscope after each experiment to check if they were attached to the surface or formed crystals. While we tried with different surfactant solutions such as SDS, Tween 20 and Cetrimonium Bromide (CTAB) with varied concentrations, 10 mM SDS-DI water solution was the ideal candidate at which colloids interacted with each other and with nearby surface only hydrodynamically. Colloidal solutions were degassed prior to experiments. Single particle sedimentation velocity was calculated to be 2.17 µm/sec and, in single particle sedimentation, Peclet number (Lee and Furst, 2006) $\left(Pe = \frac{4\pi g a^4(\rho_p - \rho_m)}{3k_B T}\right)$ is 35.

4.2.2 Image analysis

Structure growth factor analysis

To quantify colloidal structure growth over time, we calculated the characteristic structure growth factor for images as a function of time. We believe colloid structure growth is a function of local particle concentration. Therefore, we measured local growth factor at five different locations on the sample space and then we calculated mean from those measurements for a certain concentration of colloid sample at a certain time.

From 2D Fourier-transform of image intensity $I(r,t)$, we can detect dominant spatial features on the image in the form of spatial frequency and we can get characteristic length of those spatial features. Initially colloids were dispersed then, over time, their self-assembled structures evolve. Therefore, the amplitude of the lower frequency spectrum in the transformed images increases as the structure

grows. We first calculated radially-averaged static structure factor $S(q,t)$ (Teece et al., 2011) where q is the radial distance of FFT image. This is done by computing power spectrum after Fourier-transforming (FFT) of the image using the software (ImageJ). Using radial profile angle plugin of ImageJ, we computed the $S(q,t)$. Any distinctive peak on this structure factor can detect characteristic length of underlying structures in the image. As structure size increases, the peak value shifts left (from larger q to smaller q). Figure 4.1c shows examples of the radially-averaged $S(q,t)$ measurements at different times from the beginning of experiment for the colloid concentration of 3.0% (v/v). This is done after prepossessing images with FFT bandpass filter (large structures down to hundred pixels and small structures up to two pixels, as shown in Figure 4.1a). The calculated $S(q,t)$ is rather noisy and hence there is no distinct single peak. Therefore, we characterized structure growth by calculating the first moment $\widetilde{q}(t)$ of the structure factor,

$$\widetilde{q}(t) = \frac{\int_{q_1}^{q_2} q^{'}\mathrm{S}(q^{'},\mathrm{t})\mathrm{d}q^{'}}{\int_{q_1}^{q_2} \mathrm{S}(q^{'},\mathrm{t})\mathrm{d}q^{'}} \tag{4.2.1}$$

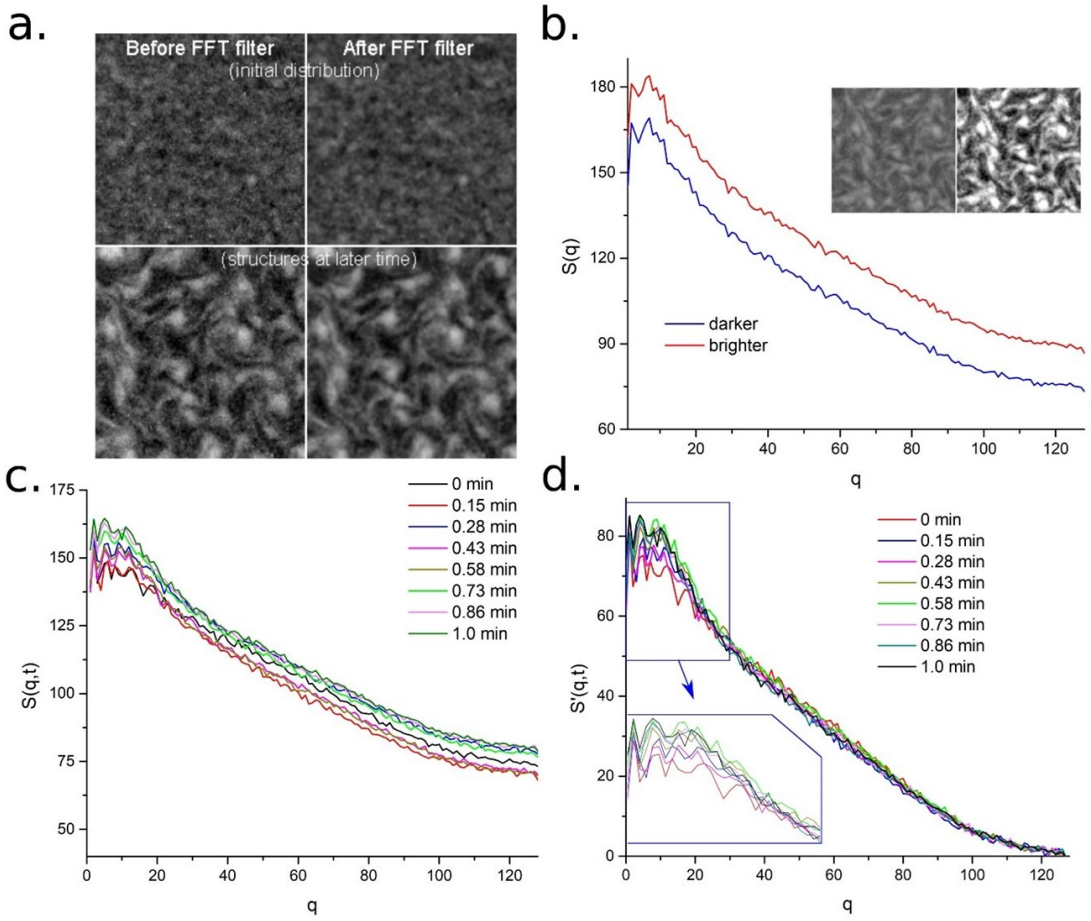

Figure 4.1: An example of image analysis procedure. Few images were taken from dynamic "vortex" formation experiment of 3.0% PMMA concentration. (a) Each image is preprocessed using FFT bandpass filter (large structures down to 100 pixels and small structures up to 2 pixels). (b) Brightness differences (while inherent structures are the same) can exhibit shifting in structure factor, $S(q)$. (c) Radially-averaged $S(q,t)$ measured at different time interval. (d) All $S(q,t)$ plots are shifted down towards a point where magnitude of all higher spatial frequency (>100) content is almost zero.

There are still practical challenges. For example, as colloids are aggregating the evolved image can have different brightness because of aggregation pattern, or simply because of different brightness of illumination. Image brightness change (while inherent structures are same) can shift radially-averaged structure factor (as shown in Figure 29b). Therefore, calculating $\widetilde{q}(t)$ using Equation 4.2.2 will not detect any trend of structure growth, rather data will scatter randomly. In

addition to that, we are mostly interested in low frequency content of $S(q,t)$ because structure changes are reflected through smaller q. With that assumption (brightness can shift the curve) and that obvious reason (low frequency content are important), we shifted all the $S(q,t)$ down towards a point where magnitude of all higher spatial frequency (>100) content becomes almost zero (shown in Figure 4.1d).

We further squared the scaled structure factor, $S'(q,t)$ so that more weight can be carried to lower frequency content. Therefore, we modified the first moment $\widetilde{q}(t)$ of the structure factor as the following,

$$\widetilde{q}(t) = \frac{\int_{q_1}^{q_2} q^{'}\mathrm{S}^{'}\left(q^{'},\mathrm{t}\right) * \mathrm{S}^{'}(q^{'},\mathrm{t})\mathrm{d}q^{'}}{\int_{q_1}^{q_2} \mathrm{S}^{'}\left(q^{'},\mathrm{t}\right) * \mathrm{S}^{'}(q^{'},\mathrm{t})\mathrm{d}q^{'}} \tag{4.2.2}$$

Finally, we calculated normalized (by the size of the transformed image) characteristic structure growth factor by computing $\frac{1}{\widetilde{q}(t)}$ which is all then multiplied by a suitable number for plotting purposes.

Images from simulations were different than those of the experiments. For example, simulation images would clearly show the location of individual particles due to the relatively lower number of particles (because of higher magnification) whereas experimental images encountered a greater number of particles and optical distortions. Therefore, we pre-processed simulation images such that the subsequent analysis was not significantly influenced by individual particles but rather structure information was captured from aggregation patterns. After converting the original simulation image to 8-bit binary, we dilated image using the software ImageJ as shown in Figure 4.2. Dilation adds pixels to the black ob-

jects and therefore minimized the effect of individual particles while sharpening the clusters. Subsequently, same FFT filtering is applied to all images to make simulated and experimental images as visually similar as possible.

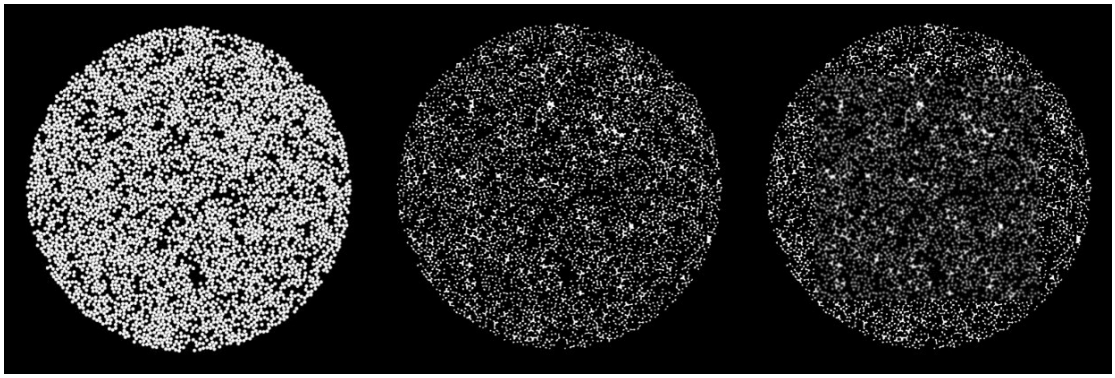

Figure 4.2: Pre-processing of simulation images. (left) image is generated from simulation. (middle) simulation image is converted to 8 bit binary image and then is dilated using imagej. (right) FFT filtering (as described in the text) is done within the ROI where the rest analysis is done.

Detecting colloidal lane formation

In the case of lane-like structures, bright spots appear in the perpendicular direction to the lanes in 2D-Fourier transformed images (as shown in Figure 4.3, bottom right). Therefore, radially averaged structure factor ($S'(q,t)$) measured only on the brighter side (shown by red zone in Figure 4.3) will always be higher than the darker side (as shown by green zone on the same figure). The peak value from the ratio of these two values will detect the maximum lane formation in evolving structures.

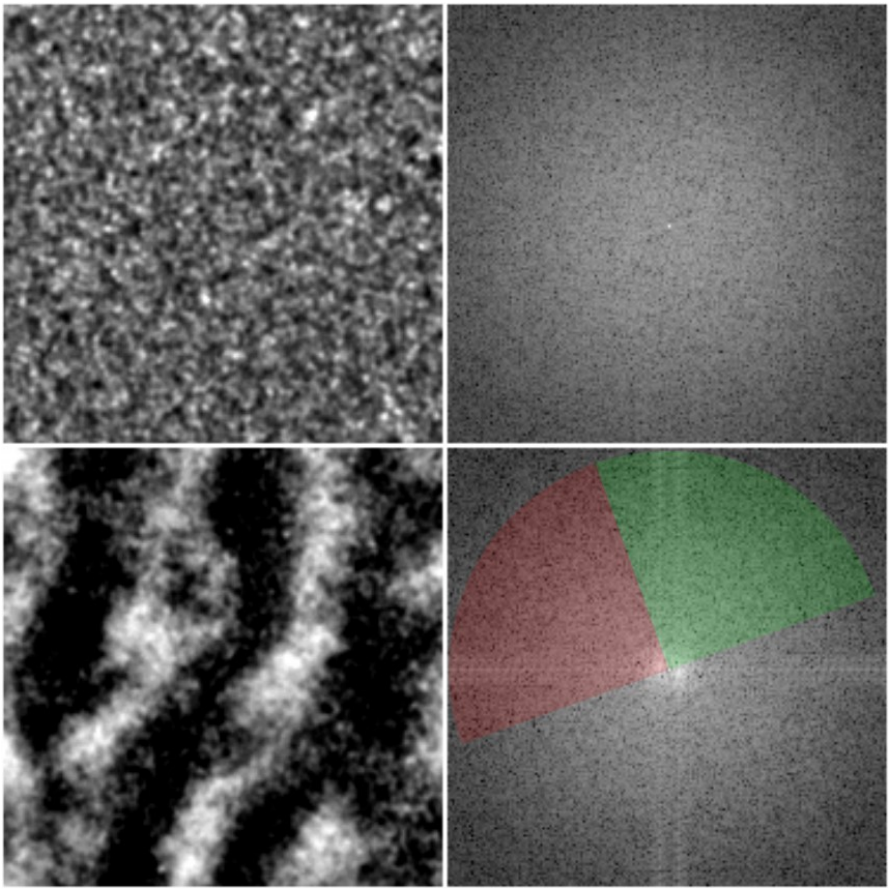

Figure 4.3: Analyzing Lane formation. (top) initial particle distribution is shown on the left and corresponding FFT image is shown on the right. Intensity of FFT image is radially uniform at all direction. (bottom) When Lane like feature (left) emerges, corresponding FFT image shows brighter intensity values in the perpendicular direction of the lane stripes marked by the red zone, while green zone shows relatively darker values.

Particles lateral migration from the wall

As particles form clusters over time, they also migrate away from the surface. With high magnification imaging, migrated particles become defocused once they leave depth of field of that objective lens. We calculated gradient features of image intensity (using MATLAB's *imgradient* function) to evaluate migration over time.

4.3 Results

Computer simulation on colloid structure formation near a solid surface, as discussed in Chapter 3, is verified through experiment. Our simulation and experiment differ in a way that former is done within 360 µm diameter of a cylindrical space, at a concentration of 0.56% v/v, while the latter is conducted in a 3000 µm diameter of cylindrical space. We worked within a small simulation space compared to the experiment space as increasing simulation space would increase the number of particles as thus the computation cost. On the other hand, we did not shrink the size of experiment space to the size of simulation space, as it would possibly alter the dynamics due to significant influence of the side wall geometry (whose influence was neglected for simulation study). In the following sections, we showed results from qualitative observations and fast-Fourier-transformation (FFT) based image analysis for two different experiments and simulation scenarios.

4.3.1 Formation of colloidal clusters

Sample cells were rotated at 20 rpm horizontally for both experiment and simulation. Particle concentration for experimental colloid solution was ranged from 0.1% to 3.0% (v/v), the simulation had a concentration of 0.56% (v/v). We observed "vortex" array like colloidal clusters whose growth rate was related to particles concentration (Figure 4.4). As magnitude of fluid flow is directly related to the number of particles (due to their mobility) in the fluid domain, we expect

rapid structure growth as particle concentration increases.

Prediction from simulation for particle concentration of 0.56% reflects experiments in similar ways. Once particles aggregated, in both experiment and simulation, it formed a cluster and these clusters translated in circular orbit (3.3.2 which at longer time scale appears to evolve as colloidal vortex array (for simulation, a single vortex). As qualitative picture (from both simulation and experiment) looks similar, we therefore examined structure growth rate. We found that structure growth rate from simulation matched closely with experiment for a similar concentration (Figure 4.5). Structure growth rate is linear until large structures collide with each other due to confinement.

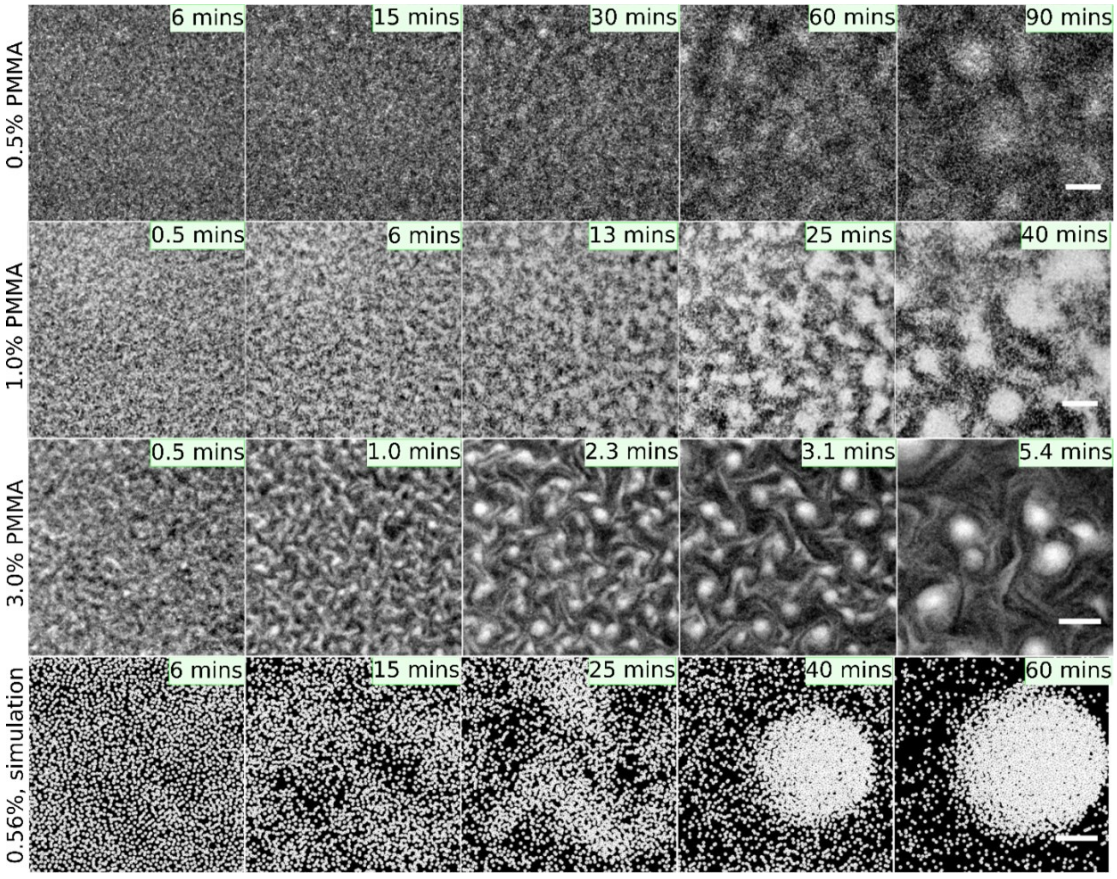

Figure 4.4: Colloid 'vortex' array like structure grows faster for higher concentration of particles. Scale bars for 0.5% PMMA, 1.0%PMMA and 3.0% PMMA are 200 µm and for the simulation (0.56% PMMA) is 50 µm.

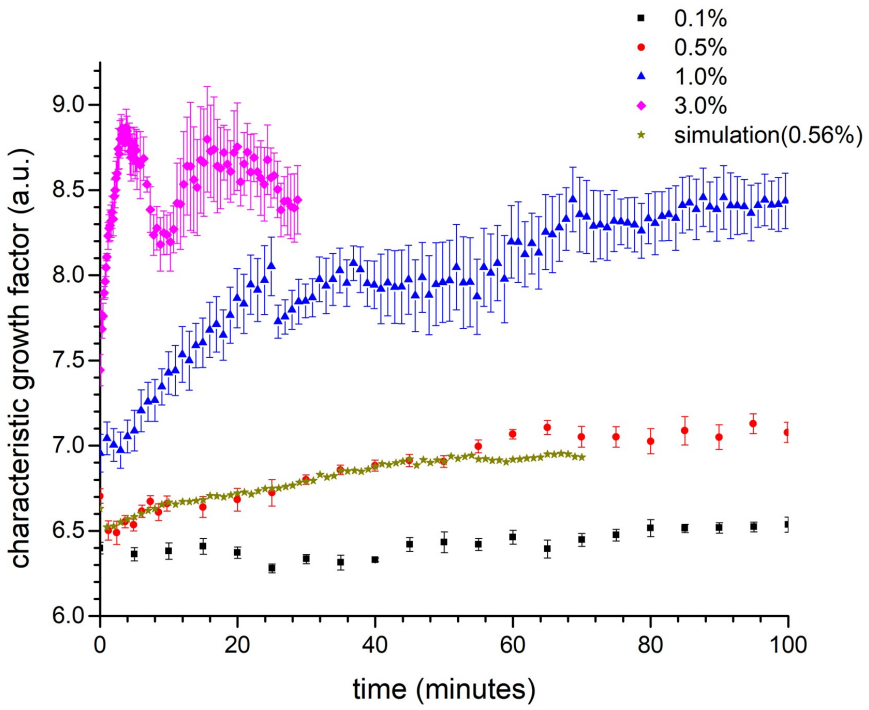

Figure 4.5: Structure growth factor is measured locally, and mean value is plotted. Error bar represents standard error of the mean (SEM). Initial particle distribution for 0.1%, 0.5% and 3.0% was uniform. However, there existed gradient for initial particle distribution for 1.0%. As particle concentration becomes higher, structure growth becomes faster. Once growing 'vortex' collide with each other structures dispersed in random manner which is shown by higher SEM values. For the case of 1.0% concentration, during linear growth higher SEM value indicates a band of linear structure growth pattern as there was a gradient in local particle distribution. Structure growth from simulation (0.56%) is plotted on top of the experiment data conducted for 0.5% concentration.

4.3.2 Colloidal Lane formation

To validate predictions from the simulation, we conducted another set of experiments that produced different dynamic structures. Instead of continuous rotation, we set a cycle of different rotation patterns, as explained in Section 3.2.2. This rotational cycle continued for several hours for experiments and for 2 hours for simulation for a similar particle concentration. We observed colloidal lane like structures from both simulation and experiment, as shown in Figure 4.6.

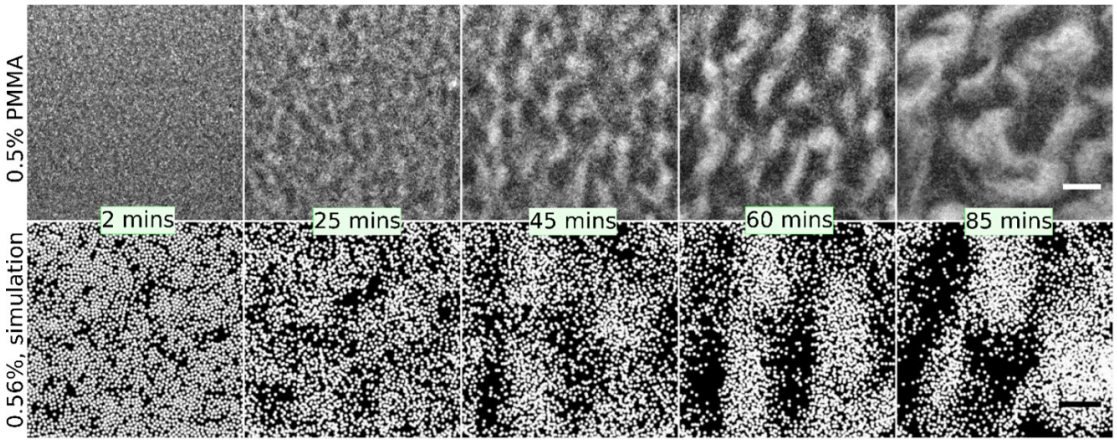

Figure 4.6: Top (experiment) and bottom (simulation). Colloids formed lane like structure in case of a cycle of new rotational scheme (as described in the text) continued for few hours. In both simulation and experiment we observed similar type of lane formation. Scale bar for experiment (0.5% PMMA) is 200 µm and for the simulation (0.56% PMMA) is 50 µm.

From an initially uniform colloidal distribution, a vivid lane formation eventually assembled until it later disappeared due to dynamic progression. Therefore, we expect similar lane formation from simulation at that time if particle concentration remains close to the experiment. We tracked length-wise structure growth as a function of time. We observed peak of this growth factor similar for both experiment and simulation (Figure 4.7).

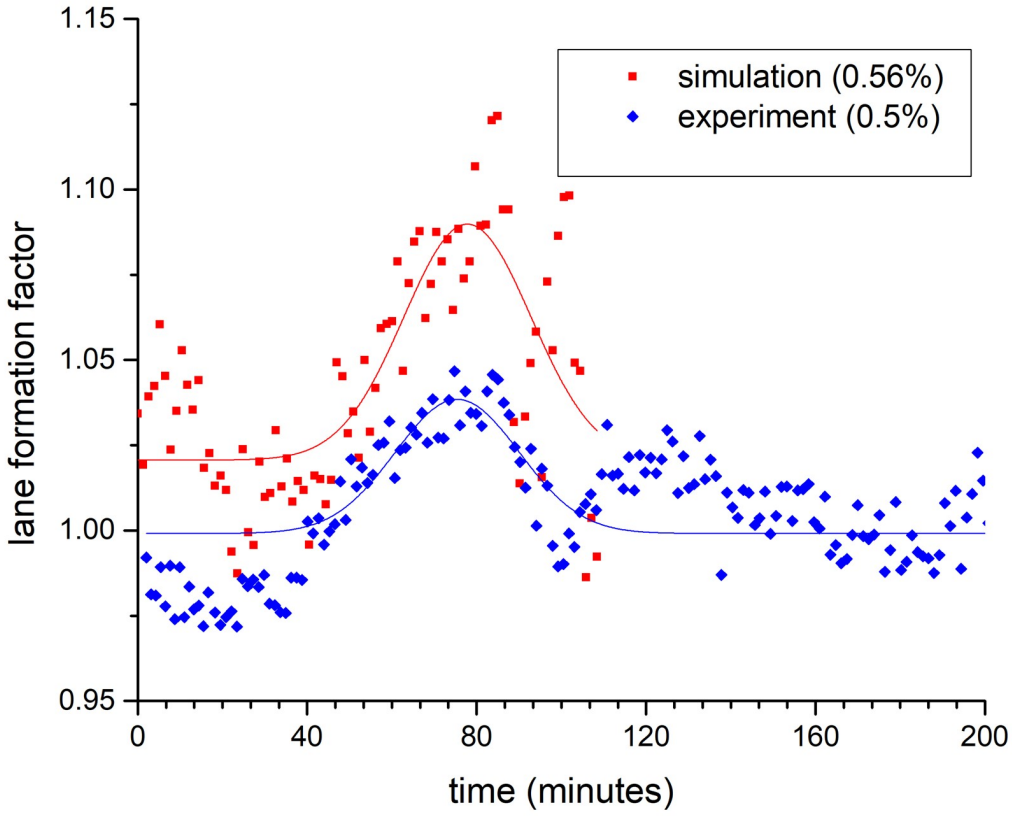

Figure 4.7: Time at the peak value of lane formation factor, which represents a ratio of image information on brighter to darker zone (see Figure 4.3), shows when vivid lane formation occurs. From both simulation and experiment, this peak value occurs at the same time. Particle concentrations are shown in percentages.

4.3.3 Efficient mixing

In Section 4.3.1, faster growth rate of colloid structure formation is shown as a function of particle concentration. Colloidal mixing is extremely slow for a low concentrated solution however employing different forcing function can improve mixing rate as shown in Figure 4.8. The more particles join in the aggregation structure, the more colloidal mobility is ensured. Enhanced colloidal mobility and lateral migration, which reduces resistance due to parallel surface interactions, while clearing particles from non-colloidal zone creates the possibility of faster

mixing.

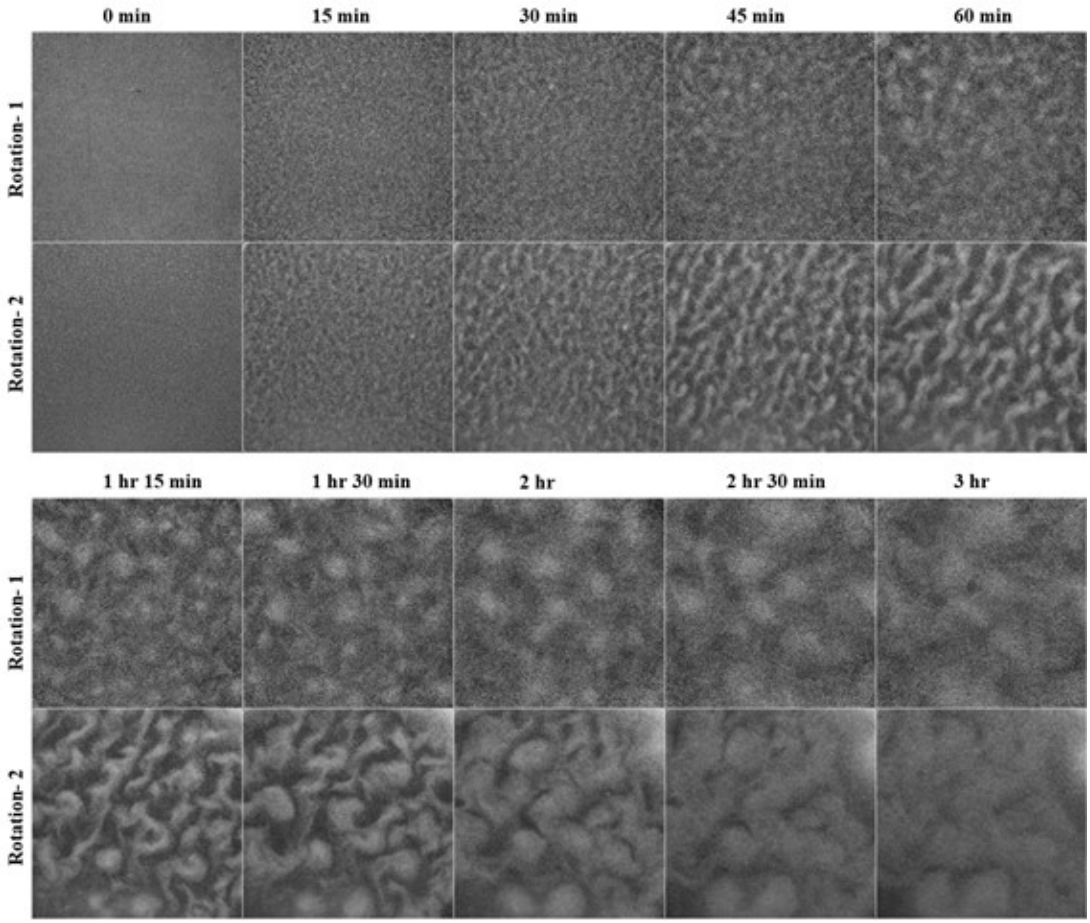

Figure 4.8: Colloidal mixing is enhanced by modulating gravity forcing function. Rotation-1 represents continuous anti-clockwise rotation of the sample cell at 20 rpm, while Rotation-2 represents a complex type of rotation pattern in one cycle-(360° counter-clockwise rotation at 20 rpm, stopped for 0.2 seconds, 180° clockwise rotation at 20 rpm, stopped for 0.2 seconds, 360° counter-clockwise rotation at 20 rpm, stopped for 0.2 seconds, 180° clockwise rotation at 20 rpm, and stopped for 0.2 seconds,). We repeated the cycle until the end of the experiment. Rotation-2 enhanced colloidal mixing. Enhanced lateral migration is also visible from defocused image for Rotation-2.

4.3.4 Lateral migration from the wall

As particles formed dynamic structures, the structures migrated away from the wall. We observed similar lateral migration pattern from experiment and simulation. With a closer view (10X microscope objective), initially particles were

focused when they reside close to the wall. Over time as particles migrated away from the wall (towards the bulk solution), they became unfocused. With 10X objective lens field of depth is 8.5 µm. Therefore, we can expect that when particles are 8.5 µm away from the focal plane, they are out of focus (as shown in Figure 4.9, top row). To generate similar data for the simulation images, particles residing above 8.5 µm are masked with a solid color (as shown in Figure 4.9, bottom row) as a representation of unfocused particles in experiment.

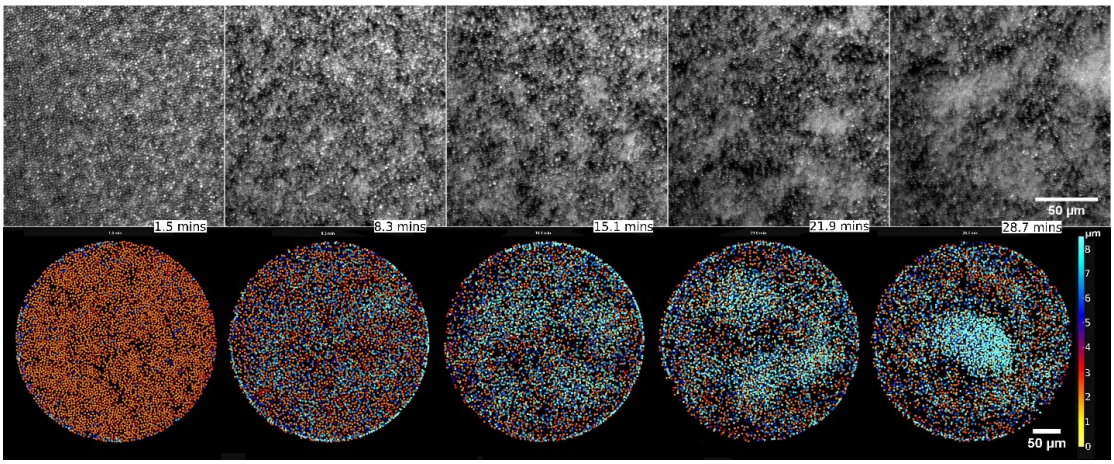

Figure 4.9: Particles laterally migrate away from the surface. (top) With 10X multiplication, due to narrow depth of field, particles enter to unfocused zone (migrate away from depth of field towards the bulk solution). (bottom) simulation work shows particle's lateral migration towards unfocused zone (8.5 µm away from the surface) while aggregating in a cluster.

In simulation, at different times we counted the number of particles which were above the height of 8.5 µm. Normalizing by the total number of particles, we can get an idea how many particles are getting into unfocused regime as time goes on. As particles migrate away from the surface, experimental images show aggregated cluster to be unfocused at higher magnification (in our case it is 10X). We see a similar trend showing unfocused clusters progress (in experimental images) and particles migrate out of focused region (in simulation images) over time. This is

shown in Figure 4.10.

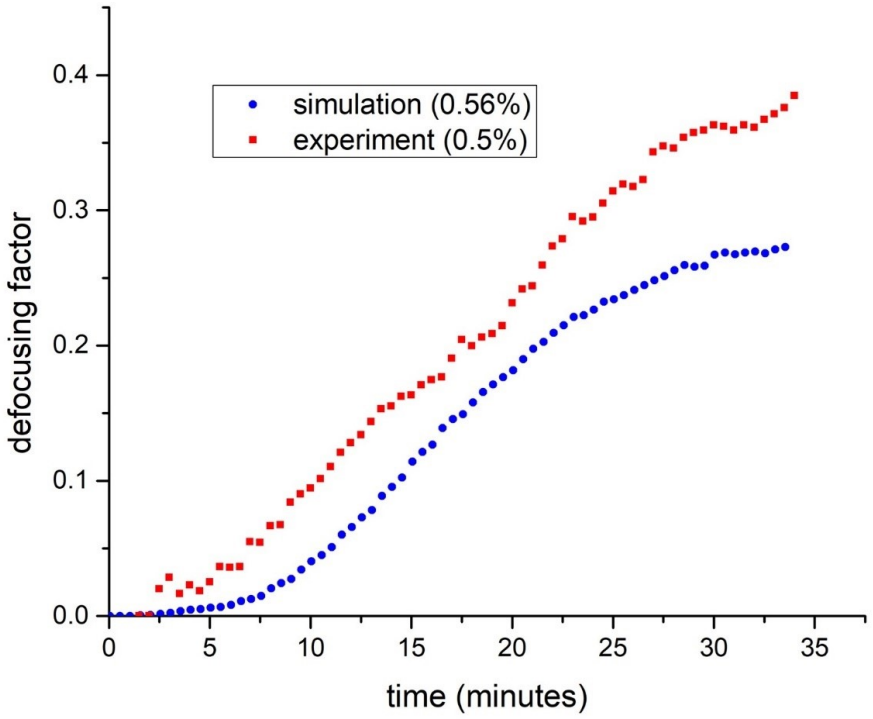

Figure 4.10: As particles form 'vortex' type cluster they are out of focus from the image plane. Therefore, gradient feature of image brightness decreases with time. Normalizing gradient features with initial gradient and subtracting from 1 can depict defocusing features which is shown as red squares. For simulation images, defocusing factor is measured knowing normalized particle fraction in the defocus region.

While one single particle does not migrate laterally, simulation and experiment for many particles show that particles aggregated while migrating away from the surface. This further confirms that our simulation predicts true colloidal hydrodynamics near a solid surface, which can be understood with two particles in Stokes flow: a particle with a force parallel to the boundary induces perpendicular motion on the other particle (Swan and Brady, 2007). For a many-body system, this effect is more obvious. In case of low Reynolds number flow, migration for single (Vasseur and Cox, 1977) or many particles (Yuan et al., 2018) have been shown

experimentally and theoretically as inertial migration. However, in our simulation the dynamics we considered is Stokes flow where inertia is absent, because of extremely low Reynolds number. As particles form cluster, they tend to shift the dynamics from extremely low Reynolds number to low Reynolds number. Interesting to note here is that without considering cluster-based inertia (where length scale is cluster diameter), Stokes flow for an individual particle (length scale is individual particle's diameter) predicts lateral migration. It signifies an important phenomenon in a sense that flow field caused by 'larger' particles or higher velocity (if that makes the flow field inertial) can be discretized as several small particles so that creeping flow motion can be applied.

4.4 Conclusion

Here we studied fluid dynamics of colloid mobility near a solid surface, where colloids were under cyclic gravity force vectors. We observed different dynamic colloid structure formations such as colloidal clusters and lanes by changing force patterns. Structures evolve faster with higher particle concentration because of added fluid motion due to mobility of nearby particles and their many-body hydrodynamic interactions. Lateral migration caused by different force pattern influences particle's mixing rate. Active colloids (or dynamic structures) are nonequilibrium phenomenon which can be difficult to study through a single or multiple parameters in a useful form or from thermodynamic concepts (Solon et al., 2015) (such as describing by the state variables- swim pressure (Takatori et al., 2014), temperature, concentrations etc.). Therefore, numerical simulation is one of the few

options to investigate colloidal structure formation. However, current methods are either very approximate (Zöttl and Stark, 2014) or based on complex mathematical formulations (Brady and Bossis, 1988; Wang and Brady, 2016; Fiore and Swan, 2019; Swan and Brady, 2007; Stenhammar et al., 2017), where an experimental colloidal scientists may not get enough physical intuition. Instead of using mathematical expressions for contact forces or lubrication interactions (Swan and Brady, 2007), which we found physically non-intuitive, we used hard-sphere colloidal collision or mobility model to track particle location after each simulation time step. The nearest velocity we calculated was at $2a$ distance which can be useful to minimize unaccounted short-range interactions. Therefore, the simulation technique is readily applicable for many practical applications where colloids are mobile near a solid surface. While our simulation worked for initially dispersed moderately concentrated ($< 1\%$ v/v) particle suspension, dense colloidal clusters evolved while not compromising actual physical dynamics. We laid the foundation for further dense colloidal suspension where reflected velocity fields due to stresslet and reflected velocity fields due to particles' reorganization through hard-sphere mobility model may need to be added. This simulation will help to predict behavior of different particle size distribution, particles located at a distance from the underlying surface, position-based and pairwise non-hydrodynamic interaction forces (such as surface charges, electric/magnetic field, etc.). Our simulation in the present form will work for any sized particles for a colloidal system where particles are spherical. However, active micro-swimmers made of different sizes and shapes can be discretized as small spheres, where their relative rigid positions can be tracked as a fixed link. For polydisperse systems, where the size distri-

bution is very large, the simulation may need to be modified to capture reflected short-ranged interactions within $2a$ of the center of the larger particle (a here is the diaamter of larger of the two particles). In the experiment, we explored a new avenue of dynamic structure formation through manipulating gravity vectors using a vertically rotated system, which can be a model system for studying hydrodynamic interactions.

CHAPTER 5

CONCLUSION

5.1 Introduction

While microgravity has been used for biological experiments for a long time to negate gravitational effects, colloid experiments in microgravity, such as on International Space Station, is a relatively new concept. Therefore, tools and methodologies have been developed for simulated microgarvity for biological experiments. Similar ground based apparatus for colloid experiments has not been developed or such a system has not been studied thoroughly. While it may not be possible to simulate long-term microgravity terrestrially, particles can resist quick sedimentation in a confined suspension system rotating vertically with appropriate rotation speed. Therefore, we investigated long-term colloid suspension mechanism which can mimic microgravity experiments for colloidal system. We started with basic knowledge of how colloids behave in confinement under the impact of rotational gravity forces. Based on rotational speed, pattern of gravity forces, and different concentration distribution, we studied colloidal structure formation and subsequent mixing through collision among dynamic structures for a certain

particle-solution selection. Our original goal was to characterize long-term colloid suspensions in this rotating system; however, along the way we observed interesting hydrodynamic patterning phenomena that was discussed in Chapter 4. In Section 5.2, I discuss how our studies herein relate towards the study of long-term suspensions.

5.2 Long term colloidal suspension regime

Within few minutes of sample loading, PMMA microparticles settles at the bottom of the sample cell. Subsequently, with the beginning of the rotational experiment, colloidal clusters formed which grew relatively faster depending on colloidal concentration (Section 4.3.1). Eventually colloid mobile clusters collide to each other and randomize their distribution throughout the sample cell, eventually resulting in a homogeneously suspended solution. Once uniformly distributed, the sample appears to remaining this state for an extended period of time (Figure 5.1). Particles still undergo sedimentation; however, their mobility is lower as their characteristic interaction distance for each particle becomes higher. If colloids aggregate and form a larger structure, this larger agglomeration will disrupt the otherwise uniform suspension behavior as it causes relatively larger disruptions in fluid flow. If large agglomerations form, the investigations of such suspensions are significantly compromised; nonetheless, this approach can be used to study long term colloidal system before forming such aggregation. In the shown set of experiments, we selected particle and the solution such that they only interact hydrodynamically. Therefore, after a long term suspended colloids did not form

crystalline structures for most of our samples. Though we did observe aggregations for some of our samples (Figure 2.13) which likely occurred due to weak electrostatic interactions.

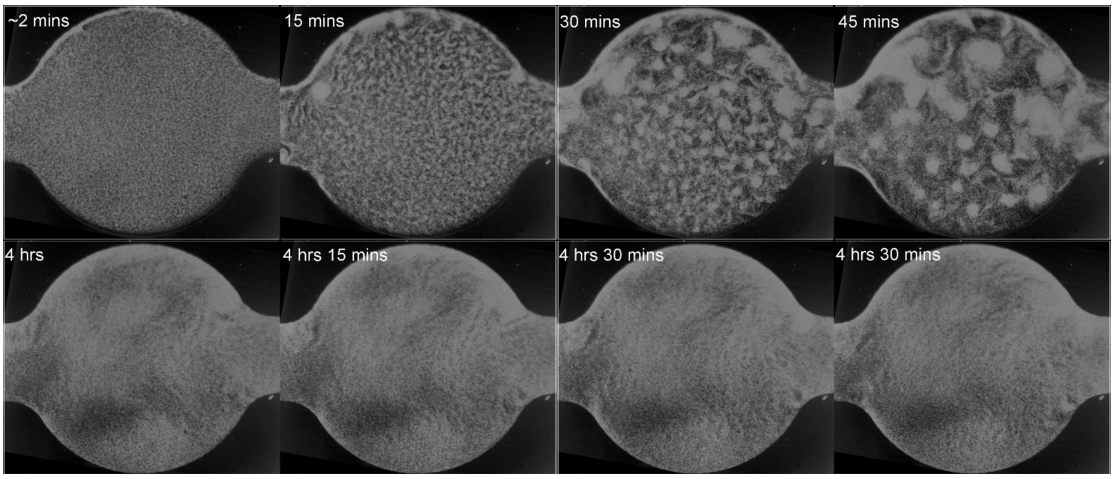

Figure 5.1: 1.0% (v/v) PMMA microspheres-DI water suspension was rotated at 20 rpm counterclockwise. Particles initially formed array like colloidal clusters (top row). Those clusters collided to each other and eventually distributed throughout the sample cell. The left column represents time from the beginning of the experiment and next three column represent subsequent 15 mins later colloidal distribution. The size of the sample cell is 3 mm and depth is 250 μm.

5.3 Limitations

Using MATLAB 2013a and using cluster parallel computing facilities, one rotational cycle took around six minutes for 4500 microparticles. Our simulation code is not optimised for efficient coding for faster running process. Therefore, it took several days to a week for a simulated 2 hour long suspension experiment. This is the reason we could not increase simulation space as increasing simulation space would increase number of particles for same concentration. Therefore, we were not able to see multiple collisions among growing clusters during cluster formation, which we observed experimentally.

We captured images from a camera system that did not rotate, whereas our sample cells were in consistent rotation. Working and observing from two different reference frames is sometimes confusing. Acquiring images within the same rotational reference frame as the experiment would help us to get more insight about the dynamics and eliminate otherwise lost data during its rotation. This would be especially important to study the formation of faster evolving patterns. By capturing continuous images (instead of taking one image in one rotation) and using registration method in the image processing software FIJI, we captured information on a rotational reference frame. However, image registration was not successful all the time.

5.4 Future directions

We envision future use of rotating platforms not only for facilitating long term colloidal suspension as a surrogate to microgravity experiment, but also as a model system to study colloidal hydrodynamics in a confinement. Such gravity manipulated system can be seen as an extension to the formulation of colloidal collective motion through the application of other methods such as electric or magnetic field.

Rotating platform with changing gravitational force vectors can be used for efficient mixing for colloidal solution where use of an active stirrer (Tierno et al., 2007) need to be avoided. For example, a magnetic stirrer can interfere with colloidal electrostatic interaction or with the application of external field.

Our simulation will be helpful for experimental colloidal scientists to set up an active colloidal system when Brownian motion is negligible relative to the fluid

motion driven by external field. In such an active colloidal system, shape and size of the particles and boundary of the confinement may play significant concern in system design. In such cases, different shape of the particles can be discretized as suitable sized microspheres where their relative position has to be tracked through fixed links. Similarly, side wall boundary can be discretized as well when after each simulation run boundary particles need to track back to its original position. During this process, hydrodynamic effect has to be counted.

The role of side wall boundary in colloidal motion is very evident (Figure 2.14). We did not explore much, however we can envision future work in side wall boundary modification. The modification could be saw-tooth like groove or rough surfaces, or flexible cilia type links. The role of such modification may not be obvious without a thorough study. However, our formulation of the simulation process can provide some clarity. For example, we can discretize protruded geometry on the side wall boundary, which may locate against a fluid flow, to spheres connected by fixed links. These spheres will follow the fluid motion due to disturbance flow. However, as they are rigid in position, putting them back in place would generate a opposing flow which may act as a counter flow. Therefore, a clever design on the boundary depending on the flow pattern can provide desired outcome.

The system can be useful in determining thermophoretic migration (Piazza, 2008; Würger, 2010) of particles due to thermal gradient for a low density particle distribution. We have seen that this type of migration is much slower (Figure 2.16) in a rotational system compared to their sedimentation velocity. Therefore, sedimentation masks thermophoretic motion which pose difficulty in measuring thermal effect (Suardi et al., 2016).

REFERENCES

Daniel Ahmed, Thierry Baasch, Nicolas Blondel, Nino Läubli, Jürg Dual, and Bradley J Nelson. Neutrophil-inspired propulsion in a combined acoustic and magnetic field. *Nature communications*, 8(1):1–8, 2017.

Joanna Aizenberg, Paul V Braun, and Pierre Wiltzius. Patterned colloidal deposition controlled by electrostatic and capillary forces. *Physical review letters*, 84 (13):2997, 2000.

Alicia Altemose, Aaron J Harris, and Ayusman Sen. Autonomous formation and annealing of colloidal crystals induced by light-powered oscillations of active particles. *ChemSystemsChem*, 2(1):e1900021, 2020.

Shimon Amselem. Remote controlled autonomous microgravity lab platforms for drug research in space. *Pharmaceutical research*, 36(12):1–15, 2019.

Christian Aponte-Rivera and Roseanna N Zia. Simulation of hydrodynamically interacting particles confined by a spherical cavity. *Physical Review Fluids*, 1 (2):023301, 2016.

AE Bailey, Wilson Che Kei Poon, Rebecca J Christianson, Andrew B Schofield, Urs Gasser, Vikram Prasad, Suliana Manley, Phil N Segre, Luca Cipelletti,

William V Meyer, et al. Spinodal decomposition in a model colloid-polymer mixture in microgravity. *Physical review letters*, 99(20):205701, 2007.

P Bartlett, PN Pusey, and RH Ottewill. Colloidal crystallization under time-averaged zero gravity. *Langmuir*, 7(2):213–215, 1991.

Rajneesh Bhardwaj, Xiaohua Fang, Ponisseril Somasundaran, and Daniel Attinger. Self-assembly of colloidal particles from evaporating droplets: role of dlvo interactions and proposition of a phase diagram. *Langmuir*, 26(11):7833–7842, 2010.

Subir Bhattacharjee, Menachem Elimelech, and Michal Borkovec. Dlvo interaction between colloidal particles: Beyond derjaguin's approximation. *Croatica Chemica Acta*, 71(4):883–903, 1998.

JR Blake. A note on the image system for a stokeslet in a no-slip boundary. In *Mathematical Proceedings of the Cambridge Philosophical Society*, volume 70, pages 303–310. Cambridge University Press, 1971.

JR Blake and AT Chwang. Fundamental singularities of viscous flow. *Journal of Engineering Mathematics*, 8(1):23–29, 1974.

John F Brady and Georges Bossis. Stokesian dynamics. *Annual review of fluid mechanics*, 20(1):111–157, 1988.

Guozhong Cao. Electrostatic stabilization: class notes. $\texttt{https://depts.washington.edu/solgel/pages/courses/MSE}_5\texttt{02/}Electrostatic_Stabilizatio$ $2021 - 09 - 14$.

Kyu Hwan Choi, Dong Woo Kang, Kyung Hak Kim, Jiwon Kim, Youngbok Lee, Sang Hyuk Im, and Bum Jun Park. Direct measurement of electrostatic interactions between poly (methyl methacrylate) microspheres with optical laser tweezers. *Soft matter*, 15(40):8051–8058, 2019.

Danielle Manoela Dantuma, Rania Elmaddawi, Yashwant Pathck, ANA MARGARIDA GRENHA, Rafaela de Oliveira, Carla Paludo, Marlise Araújo dos Santos, and Elisa Magno Nunes de Oliveira. Impact of simulated microgravity on nanoemulsion stability? a preliminary research. *American Journal of Medical and Biological Research*, 2015.

Boris V Derjaguin. Acta physicochim. *USSR*, 14, 1941.

Michelle Driscoll and Blaise Delmotte. Leveraging collective effects in externally driven colloidal suspensions: Experiments and simulations. *Current opinion in colloid & interface science*, 40:42–57, 2019.

Michelle Driscoll, Blaise Delmotte, Mena Youssef, Stefano Sacanna, Aleksandar Donev, and Paul Chaikin. Unstable fronts and motile structures formed by microrollers. *Nature Physics*, 13(4):375–379, 2017.

Louis Durlofsky, John F Brady, and Georges Bossis. Dynamic simulation of hydrodynamically interacting particles. *Journal of fluid mechanics*, 180:21–49, 1987.

Djamel El Masri, Teun Vissers, Stephane Badaire, Johan CP Stiefelhagen, Hanumantha Rao Vutukuri, Peter Helfferich, Tian Hui Zhang, Willem K Kegel, Arnout Imhof, and Alfons van Blaaderen. A qualitative confocal microscopy

study on a range of colloidal processes by simulating microgravity conditions through slow rotations. *Soft Matter*, 8(26):6979–6990, 2012.

Andrew M Fiore and James W Swan. Fast stokesian dynamics. *Journal of Fluid Mechanics*, 878:544–597, 2019.

Eric M Furst and Todd M Squires. *Microrheology*. Oxford University Press, 2017.

D Grasso, K Subramaniam, M Butkus, K Strevett, and J Bergendahl. A review of non-dlvo interactions in environmental colloidal systems. *Reviews in Environmental Science and Biotechnology*, 1(1):17–38, 2002.

Elisabeth Guazzelli and Jeffrey F Morris. *A physical introduction to suspension dynamics*, volume 45. Cambridge University Press, 2011.

John Happel and Howard Brenner. *Low Reynolds number hydrodynamics: with special applications to particulate media*, volume 1. Springer Science & Business Media, 2012.

Raul Herranz, Ralf Anken, Johannes Boonstra, Markus Braun, Peter CM Christianen, Maarten de Geest, Jens Hauslage, Reinhard Hilbig, Richard JA Hill, Michael Lebert, et al. Ground-based facilities for simulation of microgravity: organism-specific recommendations for their use, and recommended terminology. *Astrobiology*, 13(1):1–17, 2013.

Prashant V Kamat. Quantum dot solar cells. the next big thing in photovoltaics. *The journal of physical chemistry letters*, 4(6):908–918, 2013.

Mahmoud Khademi, Wuchun Wang, Wolfgang Reitinger, and Dominik PJ Barz.

Zeta potential of poly (methyl methacrylate)(pmma) in contact with aqueous electrolyte–surfactant solutions. *Langmuir*, 33(40):10473–10482, 2017.

Sangtae Kim and Seppo J Karrila. *Microhydrodynamics: principles and selected applications*. Courier Corporation, 2013.

DM Klaus, P Todd, and A Schatz. Functional weightlessness during clinorotation of cell suspensions. *Advances in Space Research*, 21(8-9):1315–1318, 1998.

Thomas E Kodger, Peter J Lu, G Reid Wiseman, and David A Weitz. Stable, fluorescent polymethylmethacrylate particles for the long-term observation of slow colloidal dynamics. *Langmuir*, 33(25):6382–6389, 2017.

Anthony JC Ladd. Hydrodynamic transport coefficients of random dispersions of hard spheres. *The Journal of chemical physics*, 93(5):3484–3494, 1990.

Myung Han Lee and Eric M Furst. Formation and evolution of sediment layers in an aggregating colloidal suspension. *Physical Review E*, 74(3):031401, 2006.

Li Li, Soeren Molin, Liang Yang, and Sokol Ndoni. Sodium dodecyl sulfate (sds)-loaded nanoporous polymer as anti-biofilm surface coating material. *International journal of molecular sciences*, 14(2):3050–3064, 2013.

Nikolai Markarian, Mike Yeksel, Boris Khusid, Anil Kumar, and Padetha Tin. Effects of clinorotation and positive dielectrophoresis on suspensions of heavy particles. *Physics of Fluids*, 16(5):1826–1829, 2004.

Martin Maxey. Simulation methods for particulate flows and concentrated suspensions. *Annual Review of Fluid Mechanics*, 49:171–193, 2017.

Jeremie Palacci, Stefano Sacanna, Asher Preska Steinberg, David J Pine, and Paul M Chaikin. Living crystals of light-activated colloidal surfers. *Science*, 339 (6122):936–940, 2013.

John P Pantina and Eric M Furst. Directed assembly and rupture mechanics of colloidal aggregates. *Langmuir*, 20(10):3940–3946, 2004.

An T Pham, Yuan Zhuang, Paige Detwiler, Joshua ES Socolar, Patrick Charbonneau, and Benjamin B Yellen. Phase diagram and aggregation dynamics of a monolayer of paramagnetic colloids. *Physical Review E*, 95(5):052607, 2017.

Roberto Piazza. Thermophoresis: moving particles with thermal gradients. *Soft Matter*, 4(9):1740–1744, 2008.

Ravi Prasher, Prajesh Bhattacharya, and Patrick E Phelan. Thermal conductivity of nanoscale colloidal solutions (nanofluids). *Physical review letters*, 94(2): 025901, 2005.

Ian Proudman. The almost-rigid rotation of viscous fluid between concentric spheres. *Journal of Fluid Mechanics*, 1(5):505–516, 1956.

Ingmar H Riedel, Karsten Kruse, and Jonathon Howard. A self-organized vortex array of hydrodynamically entrained sperm cells. *Science*, 309(5732):300–303, 2005.

Jens Rotne and Stephen Prager. Variational treatment of hydrodynamic interaction in polymers. *The Journal of Chemical Physics*, 50(11):4831–4837, 1969.

CP Royall, ME Leunissen, and A Van Blaaderen. A new colloidal model system to

study long-range interactions quantitatively in real space. *Journal of Physics: Condensed Matter*, 15(48):S3581, 2003.

P Sánchez, Michael R Swift, and PJ King. Stripe formation in granular mixtures due to the differential influence of drag. *Physical review letters*, 93(18):184302, 2004.

Asimina Sierou and John F Brady. Accelerated stokesian dynamics simulations. *Journal of fluid mechanics*, 448:115–146, 2001.

Alexandre P Solon, Yaouen Fily, Aparna Baskaran, Mickael E Cates, Yariv Kafri, Mehran Kardar, and J Tailleur. Pressure is not a state function for generic active fluids. *Nature Physics*, 11(8):673–678, 2015.

Joakim Stenhammar, Cesare Nardini, Rupert W Nash, Davide Marenduzzo, and Alexander Morozov. Role of correlations in the collective behavior of microswimmer suspensions. *Physical review letters*, 119(2):028005, 2017.

K Stewartson. On the flow between two rotating coaxial disks. In *Mathematical Proceedings of the Cambridge Philosophical Society*, volume 49, pages 333–341. Cambridge University Press, 1953.

Mirnah Binti Suardi, Mohd Azahari bin Razali, Amir bin Khalid, Hamidon bin Salleh, Azwan Sapit, Akmal Nizam bin Mohammed, and Mohd Faisal bin Hushim. Development for thermophoresis experimental under microgravity condition. In *IOP Conference Series: Materials Science and Engineering*, volume 160, page 012034. IOP Publishing, 2016.

Thomas Surrey, François Nédélec, Stanislas Leibler, and Eric Karsenti. Physical

properties determining self-organization of motors and microtubules. *Science*, 292(5519):1167–1171, 2001.

James W Swan and John F Brady. Simulation of hydrodynamically interacting particles near a no-slip boundary. *Physics of Fluids*, 19(11):113306, 2007.

Sho C Takatori, Wen Yan, and John F Brady. Swim pressure: stress generation in active matter. *Physical review letters*, 113(2):028103, 2014.

Lisa J Teece, Malcolm A Faers, and Paul Bartlett. Ageing and collapse in gels with long-range attractions. *Soft Matter*, 7(4):1341–1351, 2011.

Isaac Theurkauff, Cécile Cottin-Bizonne, Jérémie Palacci, Christophe Ybert, and Lydric Bocquet. Dynamic clustering in active colloidal suspensions with chemical signaling. *Physical review letters*, 108(26):268303, 2012.

William Thielicke and Eize Stamhuis. Pivlab–towards user-friendly, affordable and accurate digital particle image velocimetry in matlab. *Journal of open research software*, 2(1), 2014.

Pietro Tierno, Tom H Johansen, and Thomas M Fischer. Magnetically driven colloidal microstirrer. *The Journal of Physical Chemistry B*, 111(12):3077–3080, 2007.

Akira Toda, Yosuke Ohi, Ritsu Dobashi, Toshisuke Hirano, and Takashi Sakuraya. Accurate measurement of thermophoretic effect in microgravity. *The Journal of chemical physics*, 105(16):7083–7087, 1996.

Jeffrey J Urban, Dmitri V Talapin, Elena V Shevchenko, Cherie R Kagan, and Christopher B Murray. Synergism in binary nanocrystal superlattices leads to

enhanced p-type conductivity in self-assembled pbte/ag 2 te thin films. *Nature materials*, 6(2):115–121, 2007.

P Vasseur and RG Cox. The lateral migration of spherical particles sedimenting in a stagnant bounded fluid. *Journal of Fluid Mechanics*, 80(3):561–591, 1977.

Evert Johannes Willem Verwey, Jan Theodoor Gerard Overbeek, and K Van Nes. *Theory of the stability of lyophobic colloids: the interaction of sol particles having an electric double layer*. Elsevier Publishing Company, 1948.

Teun Vissers, Alfons van Blaaderen, and Arnout Imhof. Band formation in mixtures of oppositely charged colloids driven by an ac electric field. *Physical review letters*, 106(22):228303, 2011.

Mu Wang and John F Brady. Spectral ewald acceleration of stokesian dynamics for polydisperse suspensions. *Journal of Computational Physics*, 306:443–477, 2016.

Henricus H Wensink, Jörn Dunkel, Sebastian Heidenreich, Knut Drescher, Raymond E Goldstein, Hartmut Löwen, and Julia M Yeomans. Meso-scale turbulence in living fluids. *Proceedings of the national academy of sciences*, 109(36): 14308–14313, 2012.

Sébastien Wiederseiner, Nicolas Andreini, Gaël Epely-Chauvin, and Christophe Ancey. Refractive-index and density matching in concentrated particle suspensions: a review. *Experiments in fluids*, 50(5):1183–1206, 2011.

Wikipedia. Stokes's law. `https://en.wikipedia.org/wiki/Stokes%27_law`. Accessed: 2021-09-14.

Alois Würger. Thermal non-equilibrium transport in colloids. *Reports on Progress in Physics*, 73(12):126601, 2010.

Jing Yan, Ming Han, Jie Zhang, Cong Xu, Erik Luijten, and Steve Granick. Reconfiguring active particles by electrostatic imbalance. *Nature materials*, 15(10): 1095–1099, 2016.

Dan Yuan, Qianbin Zhao, Sheng Yan, Shi-Yang Tang, Gursel Alici, Jun Zhang, and Weihua Li. Recent progress of particle migration in viscoelastic fluids. *Lab on a Chip*, 18(4):551–567, 2018.

Z Zapryanov and S Tabakova. Many-particles hydrodynamic interactions. sedimentation. In *Dynamics of Bubbles, Drops and Rigid Particles*, pages 279–306. Springer, 1999.

Jixiang Zhu, Min Li, R Rogers, W Meyer, RH Ottewill, WB Russel, and PM Chaikin. Crystallization of hard-sphere colloids in microgravity. *Nature*, 387(6636):883–885, 1997.

W Zhu, Yannick Knapp, and Valérie Deplano. Low hazard refractive index and density-matched fluid for quantitative imaging of concentrated suspensions of particles. *Experiments in Fluids*, 57(5):68, 2016.

Andreas Zöttl and Holger Stark. Hydrodynamics determines collective motion and phase behavior of active colloids in quasi-two-dimensional confinement. *Physical review letters*, 112(11):118101, 2014.

APPENDIX A

Component wise velocity equations

Here we show component-wise velocity equations considering the physics explained in section 3.1.1, 3.1.2 and 3.1.5. Particle distribution is shown in Figure A.1. O represents origin of the coordinate system. Gravity vector rotates on XY plane. Z axis is pointing out of the XY plane. F_1 and F_2 represents X and Y component of gravity force $\mathbf{F}_g$.$\vec{r_p}$ is the position vector of the test particle which is moving due to gravity force $\mathbf{F}_g$ and $\vec{r_e}$ is the position vector of entrained particle.

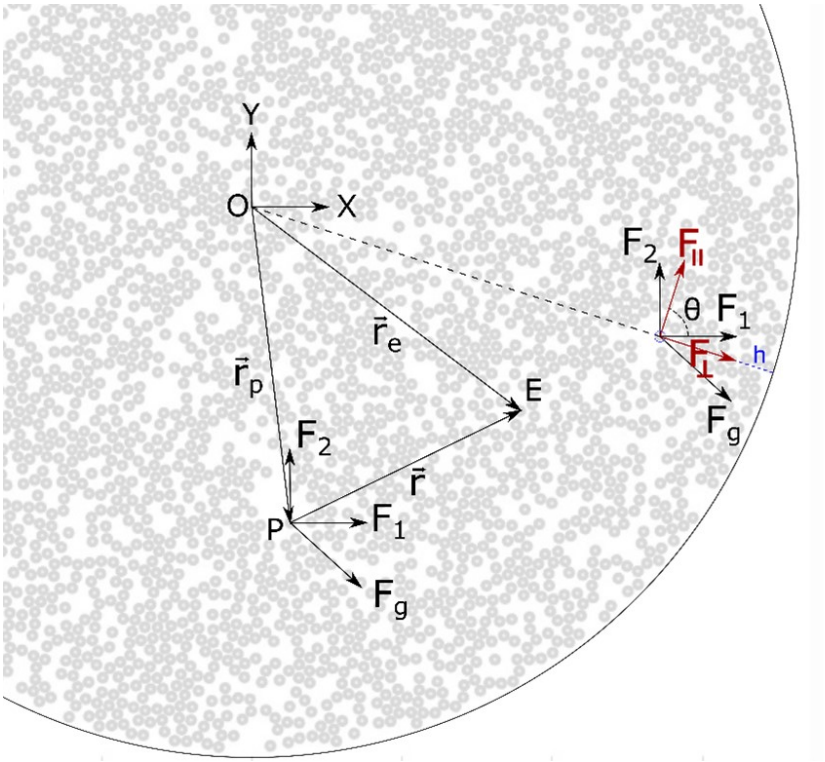

Figure A.1: Two representative particles P and E are chosen to explain all necessary equations. Gravity force is employed on particle P and E is the entrained particle. O is the origin of coordinate system. Gravity vector rotates on XY plane.

A.1 Reduced force due to side wall boundary effect

As explained in section 3.1.5, particles near the side wall boundary experience higher drag. Therefore, the position of those particles after each simulation step need to be accounted correctly using reduced gravity force. Gravity force $\mathbf{F}_g$ is first decomposed in F_1 and F_2 in X and Y direction respectively (as shown in Figure A.1). These component forces then transformed to $F_\perp$ (perpendicular to the boundary wall) and $F_\parallel$ (parallel to the boundary wall) using the following equations,

$$F_\parallel = F_1 cos(\theta) + F_2 sin(\theta) \tag{A.1.1}$$

$$F_{\perp} = F_1 sin\,(\theta) - F_2 cos(\theta) \tag{A.1.2}$$

Where, θ is computed as the following- when particle is located in positive X coordinate, $\theta = \frac{\pi}{2} + tan^{-1}\frac{y}{x}$ and when particle locates in negative Y coordinate, $\theta = \frac{3\pi}{2} + tan^{-1}\frac{y}{x}$, where x and y represent particle coordinates with respect to Point O (Figure A.1).

Reduced $F_{\parallel}$ and $F_{\perp}$ are calculated from the following equation, for details please see section 3.1.5.

$$F_{\parallel}{}' = \left(1 - \frac{9a}{16h}\right) F_{\parallel} \tag{A.1.3}$$

$$F_{\perp}{}' = \left(1 - \frac{9a}{8h}\right) F_{\perp} \tag{A.1.4}$$

As h (particle's radial distance from side wall boundary) increases, multiplying factor tends to one. Therefore, this modification only affects the boundary particles. These reduced forces then transformed back into $\mathbf{F}_1$ and $\mathbf{F}_2$ component.

$$F_1 = F_{\parallel} cos(\theta) + F_{\perp} sin(\theta) \tag{A.1.5}$$

$$F_2 = F_{\parallel} sin\,(\theta) - F_{\perp} cos(\theta) \tag{A.1.6}$$

Particles were prevented from crossing the sidewall boundaries and the parallel

surface using hard sphere colloid mobility model. In this case, side wall boundary and parallel surface are fixed and rigid. Therefore, particles are kept back to the surface radially inward (-**r**) for sidewall boundaries and perpendicularly upward (+**z**) for parallel surface.

A.2 Single particle mobility due to sedimentation near a solid surface

From Figure 3.1, we see that, $\mathbf{r} = x\hat{i} + y\hat{j} + z\hat{k}$, where $x = x_e - x_p$, $y = y_e - y_p$ and $z = z_e - z_p$. Therefore $r = \sqrt{x^2 + y^2 + z^2}$ and $R = \sqrt{x^2 + y^2 + (z_e + z_p)^2}$. Here, z_p is the height of the test particle from the underneath wall. The velocity components of a single particle mobility are as follows,

$$\begin{aligned} V_{x,1} = \frac{1}{8\pi\mu}\Bigg[&\left(\frac{1}{r} - \frac{1}{R} + \frac{x^2}{r^3} - \frac{x^2}{R^3}\right)F_1 + \left(\frac{xy}{r^3} - \frac{xy}{R^3}\right)F_2 \\ &+ 2F_1 z_p\left(\frac{z_p}{R^3} - \frac{3z_p x^2}{R^5} - \frac{(z_e + z_p)}{R^3} + \frac{3\,(z_e + z_p)\,x^2}{R^5}\right) \\ &+2F_2 z_p\left(-\frac{3z_p xy}{R^5} + \frac{3xy\,(z_e + z_p)}{R^5}\right)\Bigg] \end{aligned} \tag{A.2.1}$$

$$\begin{aligned} V_{y,1} = \frac{1}{8\pi\mu}\Bigg[&\left(\frac{1}{r} - \frac{1}{R} + \frac{y^2}{r^3} - \frac{y^2}{R^3}\right)F_2 + \left(\frac{xy}{r^3} - \frac{xy}{R^3}\right)F_1 \\ &+ 2F_2 z_p\left(\frac{z_p}{R^3} - \frac{3z_p y^2}{R^5} - \frac{(z_e + z_p)}{R^3} + \frac{3\,(z_e + z_p)\,y^2}{R^5}\right) \\ &+2F_1 z_p\left(-\frac{3z_p xy}{R^5} + \frac{3xy\,(z_e + z_p)}{R^5}\right)\Bigg] \end{aligned} \tag{A.2.2}$$

$$V_{z,1} = \frac{1}{8\pi\mu}\left[\left(\frac{xz}{r^3} - \frac{x\left(z_e+z_p\right)}{R^3}\right)F_1 + \left(\frac{yz}{r^3} - \frac{y\left(z_e+z_p\right)}{R^3}\right)F_2 \right. \\ + 2F_1 z_p\left(-\frac{3xz_p\left(z_e+z_p\right)}{R^5} + \frac{x}{R^3} + \frac{3x\left(z_e+z_p\right)^2}{R^5}\right) \\ \left. +2F_2 z_p\left(-\frac{3yz_p\left(z_e+z_p\right)}{R^5} + \frac{y}{R^3} + \frac{3y\left(z_e+z_p\right)^2}{R^5}\right)\right] \tag{A.2.3}$$

As suspended particles are of spherical shape, fluid flow caused by source dipole needs to (see Section 3.1.1 for details) be counted. Component velocities for source dipole are as follows,

$$V_{x,2} = \frac{a^2}{24\pi\mu r^3}\left(F_1 - \frac{3x\left(xF_1+yF_2\right)}{r^2}\right) \tag{A.2.4}$$

$$V_{y,2} = \frac{a^2}{24\pi\mu r^3}\left(F_2 - \frac{3y\left(xF_1+yF_2\right)}{r^2}\right) \tag{A.2.5}$$

$$V_{z,2} = -\frac{a^2 z\left(xF_1+yF_2\right)}{8\pi\mu r^5} \tag{A.2.6}$$

Therefore, resultant velocity field is shown as,

$$V_x = V_{x,1} + V_{x,2} \tag{A.2.7}$$

$$V_y = V_{y,1} + V_{y,2} \tag{A.2.8}$$

$$V_z = V_{z,1} + V_{z,2} \tag{A.2.9}$$

A.3 Torque and stresslet approximation, exerted by the fluid disturbance

Because of discontinuity of the velocity at the surface from liquid to the solid, entrained particles experience rotation due to torque, or straining motion due to stresslet or in linear combination of both. These effects are short-ranged. Therefore, it does not add significant contribution compared to long-range counterpart. For dilute suspension of monodispersed colloids, this part can be safely omitted. For dense bimodal or polydisperse suspension following approximation can be useful.

We can first consider about torque. This is explained in the text and shown graphically in Figure 3.2 . In section 3.1.1 and 3.1.2, we have shown velocity calculation for entrained particle. Now we will switch entrained and driven particle (we can do that because of the symmetry). Velocity field reflected at P due to rotation will change the velocity of the particle E.

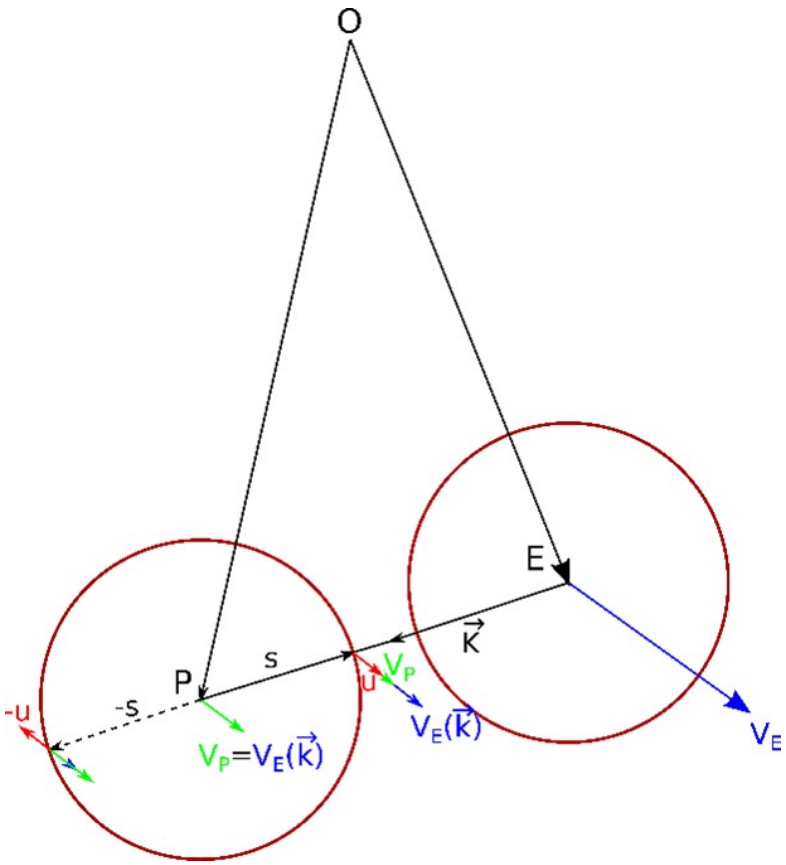

Figure A.2: Reflected flow field caused by particle's (P) rigidity and no-slip boundary condition. Flow field caused by particle E is reflected back to the particle E if both particles locate nearby to each other.

Let's assume u is the rotational velocity of the particle P (Figure A2) due to the gravity force on particle E. we can write angular velocity as,

$$\mathbf{\Omega} = \frac{u}{a}\left(\hat{\mathbf{s}} \times \hat{\mathbf{u}}\right) \tag{A.3.1}$$

$$\mathbf{\Omega} = \frac{-\hat{\mathbf{k}} \times \mathbf{u}}{a} \tag{A.3.2}$$

Where, $\hat{\mathbf{s}} = -\hat{\mathbf{k}}$ and $\mathbf{u} = u\hat{\mathbf{u}}$ (from Figure 3.2). However, $\hat{\mathbf{k}} = -\hat{\mathbf{r}}$ (particles are switched, compare Figure 3.2 with Figure 3.1). We can approximate $\mathbf{u}$ as $\mathbf{v}_p$, where $\mathbf{v}_p[= \mathbf{v}_E(\mathbf{k})]$ is the local velocity at the center of the particle P caused

by the gravity force at the particle E. Because of symmetry, velocity field caused by each particle is interchangeable. Therefore, $\mathbf{v}_E(\mathbf{k}) = \mathbf{v}(\mathbf{r})$, when $\mathbf{r} = -\mathbf{k}$. Therefore, the final expression for angular velocity is,

$$\mathbf{\Omega} = \frac{\hat{\mathbf{r}} \times \mathbf{v}(\mathbf{r})}{a} \tag{A.3.3}$$

Angular velocity components are as follows,

$$\Omega_x = \frac{yV_z - zV_y}{ar} \tag{A.3.4}$$

$$\Omega_y = \frac{zV_x - xV_z}{ar} \tag{A.3.5}$$

$$\Omega_z = \frac{xV_y - yV_x}{ar} \tag{A.3.6}$$

Once we know angular velocity of the particle P, we can get the velocity component of the particle E due to rotation of particle P from Equation 3.1.2.

$$v_{x,rot} = \frac{a^3(z\Omega_y - y\Omega_z)}{r^3} \tag{A.3.7}$$

$$v_{y,rot} = \frac{a^3(x\Omega_z - z\Omega_x)}{r^3} \tag{A.3.8}$$

$$v_{z,rot} = \frac{a^3 \left(y\Omega_x - x\Omega_y \right)}{r^3} \tag{A.3.9}$$

A similar scaling argument can be applied for straining motion. However, solution for the straining motion is more complicated compared to the rotation. While flow field due to rotation decays as r^{-3}, flow field due to straining decays as r^{-4}. As our solutions are relatively dilute, we did not include this. The equation (Guazzelli and Morris, 2011) for straining motion can be written as follows,

$$u_i = -\frac{5a^3 x_i \left(x_j E^{\infty}_{jk} x_k \right)}{r^5} - \frac{a^5}{2} E^{\infty}_{jk} \left[\frac{\delta_{ij} x_k + \delta_{ik} x_j}{r^5} - \frac{5 x_i x_j x_k}{r^7} \right] \tag{A.3.10}$$

$$u_i = -\frac{5a^3 x_i \left(x_j E^{\infty}_{jk} x_k \right)}{r^5} - \frac{a^5}{2} E^{\infty}_{jk} \left[\frac{\delta_{ij} x_k + \delta_{ik} x_j}{r^5} - \frac{5 x_i x_j x_k}{r^7} \right] \tag{A.3.11}$$

Where, $E^{\infty}_{jk} = \frac{1}{2} \left[\frac{\partial u_i(\mathbf{r})}{\partial x_j} + \frac{\partial u_j(\mathbf{r})}{\partial x_i} \right]$, evaluated at the center of particle P.

APPENDIX B

Computer simulation Code

B.1 MATLAB code for particle generation

```
% This code is to generate non overlapping
%circular spheres
% near a solid surface
%%
clear all
 a=2e-6;
 rlength=100e-6; %radius
 rheight=150e-6;
 centrx=rand(1,12000)*2*rlength-rlength;
 centrx=centrx';
 centry=rand(1,12000)*2*rlength-rlength;
 centry=centry';
 centrz=rand(1,12000)*(rheight-2*a)+a;
```

```
 centrz=centrz';
 rad(1:size(centrx,1),1) = a;


r = sqrt(centrx.^2+centry.^2);
        nn = find(r >(rlength));
        centrx(nn)=[];
        centry(nn)=[];
        rad(nn)=[];
        centrz(nn)=[];
clear nn


 tic;


writerObj = VideoWriter('particle_gen2.avi');
open(writerObj);


f = figure;
% Set a size if desired
    width = 1466;
    height = 1130;
set(f,'Position',[5 5 width height])


%Change the renderer to avoid bugs due to OpenGL
set(f,'Renderer','ZBuffer')
```

```
zscaled = centrz(:,end)/1e-6;
cn = ceil(max(zscaled));
cm = colormap(jet(cn));
S = repmat(350,numel(centrx(:,1)),1);

for pp = 1:1:100

    centrx1=zeros(1,size(centrx,1))';
    centry1=zeros(1,size(centrx,1))';
    centrz1=zeros(1,size(centrx,1))';

    parfor p = 1:1:size(centrx,1)

        centrx1(p)=centrx(p);
        centry1(p)=centry(p);
        centrz1(p)=centrz(p);

            x = centrx-centrx1(p);
            y = centry-centry1(p);
            z = centrz-centrz1(p);

            r = sqrt(x.^2+y.^2+z.^2);
        [B,I] = sort(r,'ascend');
```

```
% sort distances of all particles from particle p
% in ascending order.
% I is the original index location.

            mmm=find(r(I)<3*a); %
            mmm(1)=[]; % first value is zero,
                       % discard that index


            if isempty(mmm)
                ;
            else
                for(j=1:1:size(mmm))
                mm=I(mmm(j));
                if((r(mm))<2*a)

centrx1(p) = centrx1(p) + (0.5-a/r(mm))*x(mm);
centry1(p) = centry1(p) + (0.5-a/r(mm))*y(mm);
centrz1(p) = centrz1(p) + (0.5-a/r(mm))*z(mm);


                 end


                if (centrz1(p)<a)
                centrz1(p)=a;
                end
```

```
            x = centrx-centrx1(p);

            y = centry-centry1(p);

            z = centrz-centrz1(p);


            r = sqrt(x.^2+y.^2+z.^2);
             end
            %clear mm
          end
          %clear B I mmm

end

centrx = centrx1;

centry = centry1;

centrz = centrz1;

clear centrx1 centry1 centrz1

centrx_check(:,pp+1)=centrx;


%Clear the axes.

cla;



%Set the axis aspect ratio to 1:1.

axis equal;
```

```
%Set a title.
title([num2str(pp) ' iteration'])
hold on
%Display the circles.
scatter3(centrx, centry,centrz, S,centrz, 'filled')
colorbar
caxis([2e-6 20e-6]) %cn*1e-6
view(0,90)
grid off
set(gca,'FontSize',18)

  xlim([-rlength-3*a rlength+3*a]);
  ylim([-rlength-3*a rlength+3*a]);

%Pause for 1 second.
pause(0.1);
%movievector(i)= getframe;
frame = getframe(f);
writeVideo(writerObj,frame);

if max(centrx_check(:,pp+1)-centrx_check(:,pp))<1e-8
    break;
end
```

```
end
toc;


r = sqrt(centrx.^2+centry.^2);
        nn = find(r >(rlength));
        centrx(nn)=[];
        centry(nn)=[];
        rad(nn)=[];
        centrz(nn)=[];
clear nn
```

B.2 MATLAB code for pairwise hydrodynamic interaction

```
% change the file name to vsedfield.m
% This code describes a function which calculates
% pairwise velocity fields.
% x, y, z is the component of position vector r
% of all particles from entrianed particle P.
% centrx,centry,centrz is the location of all particles
% rlength represents simulation size in radius
% a is particle raidus
% F is gravity force on the particle
% vsedtheta describes orientation of the gravity force
% with respect to horizontal axis.
```

```
function [vx,vy,vz] = vsedfield(x,y,z,centrx, ...
...centry,centrz,rlength,a,F,vsedtheta)
mu = 8.9e-4;                %viscosity of water
r = sqrt(x.^2+y.^2+z.^2);
h=centrz;                   %height from the wall
R = sqrt(x.^2+y.^2+(z+2.*h).^2);
                            %See figure 1 main text
z2 = z+2.*h;                %Z component of R

%%compute reduce gravity force
r1 = sqrt(centrx.^2+centry.^2);
% r1, h1 for measuring particle radial
% distance from the side wall
h1 = sqrt(((rlength./r1-1).*centrx).^2+...
  ((rlength./r1-1).*centry).^2);

F1 = F*cos(vsedtheta);
F2 = F*sin(vsedtheta);

   aa=find(centrx>0);
   %find theta for coordinate transformation
       theta(aa)=pi/2+atan(centry(aa)./centrx(aa));
   bb=find(centrx<0);
```

```
    theta(bb)=3*pi/2+atan(centry(bb)./centrx(bb));
cc=find(centrx==0);
    theta(cc)=0;

theta=theta';

F11=F1.*cos(theta)+F2.*sin(theta);
%transform to new coordinate
F31=-F1.*sin(theta)+F2.*cos(theta);
F21(1:size(F11),1)=0;

F11=(1-9*a./(16.*h1)).*F11;
%calculate reduced force
F31=(1-9*a./(8.*h1)).*F31;

F1=F11.*cos(theta)-F31.*sin(theta);
%transform back to previous coordinate
F2=F11.*sin(theta)+F31.*cos(theta);

%% long range- point force- solid wall image reflection
vx = (F1.*((1./r-1./R)+(x.^2)./r.^3-(x.^2)./R.^3) + ...
F2.*(x.*y./r.^3-x.*y./R.^3)+ ...
2*F1.*h.*(h./R.^3-3.*h.*x.^2./R.^5-z2./R.^3+ ...
3.*z2.*x.^2./R.^5)+...
```

```
2*F2.*h.*(-3.*h.*x.*y./R.^5+ ...
3.*x.*y.*z2./R.^5))/(8*pi*mu);

vy = (F2.*((1./r-1./R)+(y.^2)./r.^3-(y.^2)./R.^3) + ...
F1.*(x.*y./r.^3-x.*y./R.^3)+ ...
2*F2.*h.*(h./R.^3-3.*h.*y.^2./R.^5-z2./R.^3+ ...
3.*z2.*y.^2./R.^5)+...
2*F1.*h.*(-3.*h.*x.*y./R.^5+...
3.*x.*y.*z2./R.^5))/(8*pi*mu);

vz = (F1.*(x.*z./r.^3-x.*z2./R.^3) + ...
F2.*(y.*z./r.^3-y.*z2./R.^3)+ ...
2*F1.*h.*(-3.*h.*z2.*x./R.^5+x./R.^3+ ...
3.*x.*z2.^2./R.^5)+...
2*F2.*h.*(-3.*h.*z2.*y./R.^5+y./R.^3+ ...
3.*y.*z2.^2./R.^5))/(8*pi*mu);

%%short range- source dipole
A = (F1.*x+F2.*y)./r;

vx1 = (((a^2)./(3*(r.^2))).*(F1-3.*A.*x./r))./(8*pi*mu.*r);
vy1 = (((a^2)./(3*(r.^2))).*(F2-3.*A.*y./r))./(8*pi*mu.*r);
vz1 = -(((a^2)./(3*(r.^2))).*(3.*A.*z./r))./(8*pi*mu.*r);
```

```
vxx = vx1+vx;

vyy = vy1+vy;

vzz = vz1+vz;


%%short range- particle rotation

omega_x = (y.*vzz-z.*vyy)./(a.*r);

omega_y = (z.*vxx-x.*vzz)./(a.*r);

omega_z = (x.*vyy-y.*vxx)./(a.*r);


vx2 = (a^3)*(omega_y.*z-y.*omega_z)./r.^3;

vy2 = (a^3)*(omega_z.*x-z.*omega_x)./r.^3;

vz2 = (a^3)*(omega_x.*y-x.*omega_y)./r.^3;


ux=vx1+vx2;

uy=vy1+vy2;

uz=vz1+vz2;


kk=find(centrz<2*a);

%account wall effect on the short range interaction

ux(kk)=(vx1(kk)+vx2(kk)).*centrz(kk)/(2*a);

uy(kk)=(vy1(kk)+vy2(kk)).*centrz(kk)/(2*a);

uz(kk)=(vz1(kk)+vz2(kk)).*centrz(kk)/(2*a);


vx = vx+ux;
```

```
    vy = vy+uy;

    vz = vz+uz;


            m=find(r==0);

      %calculate velocity for the entrained particle itself

      vx(m) = (1-9*a/(16*h(m))).*F1(m)/(6*pi*mu*a);

      vy(m) = (1-9*a/(16*h(m))).*F2(m)/(6*pi*mu*a);

      vz(m) = 0;


      clear m

end
```

B.3 MATLAB code for 'vortex' like cluster formation

```
%Created by Rony, Date- 5/12/2020

%This code calculates velocity of all particles

%based on hydrodynamic interaction



%% Initialize program


clear all;   %clears variables

warning off
```

```
%% Calculate force on the particle

a = 2.0e-6;          %particle radius
g = 9.81;            %gravity accelaration
visc = 8.9e-4;       %visocity of water
mu = 8.9e-4;         %viscosity of water
densityliq = 997;    %density liquid
densitysol = 1220;   %density solid
deldens = (densitysol-densityliq);
%density difference

F = (4/3)*pi*a^3*g*deldens;  %force on the particle

%% Orbital variables

n = 20;              %rotational speed (rpm)


%% simulation parameters

rlength = 180e-6;
%simulation space in radius, um
rotstep = -6;   %rotation step, degrees
```

```
rotend = -(360+rotstep); %end rotation
rotstart = 0;     %start rotation
timestep = 60*abs(rotstep)/(n*360);


%% Locate center position of random
%circles that don't overlap
centrx1=dlmread('centrx.txt');
%non-overlap particles coordinate
%generated from another code
centry1=dlmread('centry.txt');
centrz1=dlmread('centrz.txt');

centrx=centrx1(:,end);
%initial distribution
centry=centry1(:,end);
centrz=centrz1(:,end);


centrx_plot(:,1)= centrx;
%after each rotation,
%particles coordinates are saved here
centry_plot(:,1)= centry;
centrz_plot(:,1)= centrz;
```

```
for run=1:1:600
%End of value of run will
%save that amount of image in stack
tic;


k=0;
for t = rotstart:rotstep:rotend
%This loop runs within one rotation
    k=k+1;
    vsedtheta=degtorad(t-90);
    %gravity rotates clockwise


    %hardsphere model


    centrx1=zeros(1,size(centrx,1))';
    centry1=zeros(1,size(centrx,1))';
    centrz1=zeros(1,size(centrx,1))';


    parfor p = 1:1:size(centrx,1)


        centrx1(p)=centrx(p);
        centry1(p)=centry(p);
        centrz1(p)=centrz(p);
```

```
x = centrx-centrx1(p);

y = centry-centry1(p);

z = centrz-centrz1(p);


r = sqrt(x.^2+y.^2+z.^2);

 [B,I] = sort(r,'ascend');
% sort distances of all particles from particle
% p in ascending order.
% I is the original index location


mmm=find(r(I)<3*a);                                    %
mmm(1)=[];          % first value is zero,
                    % discard that index


 if isempty(mmm)

     ;

 else

    for(j=1:1:size(mmm))

   mm=I(mmm(j));


    if((r(mm))<2*a)


centrx1(p) = centrx1(p) + (0.5-a/r(mm))*x(mm);
```

```
centry1(p) = centry1(p) + (0.5-a/r(mm))*y(mm);
centrz1(p) = centrz1(p) + (0.5-a/r(mm))*z(mm);

        end

        if (centrz1(p)<a)
        centrz1(p)=a;
        end

        x = centrx-centrx1(p);
        y = centry-centry1(p);
        z = centrz-centrz1(p);

        r = sqrt(x.^2+y.^2+z.^2);
        end
        %clear mm
    end
    %clear B I mmm

end
centrx = centrx1;
centry = centry1;
centrz = centrz1;
clear centrx1 centry1 centrz1
```

```
clear x y z


        r1 = sqrt(centrx.^2+centry.^2);
        %boundary particles are kept within
        %the boundary using hardsphere model
ee=find(r1>(rlength-a));
centrx(ee)=(rlength-a).*centrx(ee)./r1(ee);
centry(ee)=(rlength-a).*centry(ee)./r1(ee);
clear ee

%computation

vxgrid=zeros(1,size(centrx,1))';
vygrid=zeros(1,size(centrx,1))';
vzgrid=zeros(1,size(centrx,1))';

parfor p = 1:1:size(centrx,1)
%velocity measurement of all particles

        x = centrx(p)-centrx;
        y = centry(p)-centry;
        z = centrz(p)-centrz;

[vx,vy,vz] = vsedfield(x,y,z,centrx,centry, ...
```

```
centrz,rlength,a,F,vsedtheta);
%pairwise velocity measurement
%for a single particle

            vxgrid(p) = sum(vx)+vxgrid(p);
            %sum all measurements to get
            %velocity of particle p
            vygrid(p) = sum(vy)+vygrid(p);
            vzgrid(p) = sum(vz)+vzgrid(p);

    end

        centrx = timestep*vxgrid+centrx;
        %update new location based
        %on new displacement
        centry = timestep*vygrid+centry;
        centrz = timestep*vzgrid+centrz;

end

centrx_plot(:,run+1)= centrx;
%after each rotation save the
%coordinates in new variables
centry_plot(:,run+1)= centry;
```

```
centrz_plot(:,run+1)= centrz;


dlmwrite('centrxx3.txt',centrx_plot);
%after each rotation save the
%coordinates of the particles in a file
dlmwrite('centryy3.txt',centry_plot);
dlmwrite('centrzz3.txt',centrz_plot);


toc;


end


matlabpool close
```

B.4 MATLAB code for lane formation

```
%% Description
% This program provides the velocity
%field for a rotating particle
%(one revolution).


%% Initialize program
```

```
clear all;   %clears variables
warning off


%% sedimentation velocity magnitude

a = 2.0e-6;   %particle radius
g = 9.81;   %gravity
visc = 8.9e-4;   %visocity
densityliq = 997;   %density liquid
densitysol = 1220;   %density solid
deldens = (densitysol-densityliq);
%density difference

%F = (1/6)*a^3*g*deldens/visc;
%sedimentation velocity

F = (4/3)*pi*a^3*g*deldens;
%sedimentation velocity

%% Orbital variables

n = 20; %rotational speed (rpm)
```

```
%rsed = vsed*60/(2*pi*n);
%sedimentation radius

%% simulation parameters

rlength =  180e-6;
%simulation space

rotstep1 = -6;   %rotation step, degrees
rotend = -(360+rotstep1);   %end rotation
rotstart = 0;   %start rotation
timestep = 60*abs(rotstep1)/(n*360);
stoptime = 0.2;

%% Locate center position of
%random circles that don't overlap
centrx1=dlmread('centrx.txt');
centry1=dlmread('centry.txt');
centrz1=dlmread('centrz.txt');



centrx=centrx1(:,end);
centry=centry1(:,end);
centrz=centrz1(:,end);
```

```
%r = sqrt(centrx.^2+centry.^2);
%          nn = find(r >(rlength));
%          centrx(nn)=[];
%          centry(nn)=[];
%          centrz(nn)=[];
%clear nn


%nn=find(centrz >1.3*a);
%          centrx(nn)=[];
%          centry(nn)=[];
%          centrz(nn)=[];
%clear nn


centrx_plot(:,1)= centrx;
centry_plot(:,1)= centry;
centrz_plot(:,1)= centrz;
%% Vector calculations


clear centrx1 centry1 centrz1


for run=1:1:300
tic;
k=0;
```

```
                %%4 different rotation in one cycles


for rot = 1:1:4


 if rot==1
      rotstart = 0;   %start rotation
      rotstep = rotstep1;   %rotation step, degrees
      rotend = -(360+rotstep);   %end rotation
        elseif rot==2
      rotstart = -360;   %start rotation
      rotstep = -rotstep1;   %rotation step, degrees
      rotend = -(180+rotstep);   %end rotation
        elseif rot==3
      rotstart = -180;   %start rotation
      rotstep = rotstep1;   %rotation step, degrees
      rotend = -(540+rotstep);   %end rotation
        else
      rotstart = -540;   %start rotation
      rotstep = -rotstep1;   %rotation step, degrees
      rotend = -(360+rotstep);   %end rotation
        end
           t=rotstart;
```

```
for u = 1:1:inf

    k=k+1;

    vsedtheta=degtorad(t-90);


    vxgrid=zeros(1,size(centrx,1))';

    vygrid=zeros(1,size(centrx,1))';

    vzgrid=zeros(1,size(centrx,1))';



    %%hardsphere model


    centrx1=zeros(1,size(centrx,1))';

    centry1=zeros(1,size(centrx,1))';

    centrz1=zeros(1,size(centrx,1))';


    parfor p = 1:1:size(centrx,1)


        centrx1(p)=centrx(p);

        centry1(p)=centry(p);

        centrz1(p)=centrz(p);


            x = centrx-centrx1(p);

            y = centry-centry1(p);

            z = centrz-centrz1(p);
```

```
        r = sqrt(x.^2+y.^2+z.^2);
        [B,I] = sort(r,'ascend');
% sort distances of all particles from particle
%p in ascending order
% I is the original index location

        mmm=find(r(I)<3*a); %
        mmm(1)=[]; % first value is zero,
                   % discard that index

        if isempty(mmm)
            ;
        else
            for(j=1:1:size(mmm))
            mm=I(mmm(j));

            if((r(mm))<2*a)

centrx1(p) = centrx1(p) + (0.5-a/r(mm))*x(mm);
centry1(p) = centry1(p) + (0.5-a/r(mm))*y(mm);
centrz1(p) = centrz1(p) + (0.5-a/r(mm))*z(mm);

            end
```

```
            if (centrz1(p)<a)
            centrz1(p)=a;
            end

            x = centrx-centrx1(p);
            y = centry-centry1(p);
            z = centrz-centrz1(p);

            r = sqrt(x.^2+y.^2+z.^2);
            end
            %clear mm
        end
        %clear B I mmm

end
centrx = centrx1;
centry = centry1;
centrz = centrz1;
clear centrx1 centry1 centrz1


clear x y z
```

```
%% hard-sphere model for side-wall boundary

r1 = sqrt(centrx.^2+centry.^2);
     ee=find(r1>(rlength-a));
     centrx(ee)=(rlength-a).*centrx(ee)./r1(ee);
     centry(ee)=(rlength-a).*centry(ee)./r1(ee);
     clear ee

%% pair-wise colloidal interaction
%counted for all particles

     parfor p = 1:1:size(centrx,1)

          x = centrx(p)-centrx;
          y = centry(p)-centry;
          z = centrz(p)-centrz;

[vx,vy,vz] = vsedfield(x,y,z,centrx,centry,...
     centrz,rlength,a,F,vsedtheta);

     vxgrid(p) = sum(vx)+vxgrid(p);
     vygrid(p) = sum(vy)+vygrid(p);
     vzgrid(p) = sum(vz)+vzgrid(p);
```

```
    end

% Update new location

        centrx = timestep*vxgrid+centrx;
        centry = timestep*vygrid+centry;
        centrz = timestep*vzgrid+centrz;


%check if it completes one rotational cycle

    if(u<=ceil(stoptime/timestep))
        ;
    elseif t~=rotend
        t=t+rotstep;
    else
        break;
    end
end

end

centrx_plot(:,run+1)= centrx;
centry_plot(:,run+1)= centry;
```

```
centrz_plot(:,run+1)= centrz;


dlmwrite('centrx_gel.txt',centrx_plot);
dlmwrite('centry_gel.txt',centry_plot);
dlmwrite('centrz_gel.txt',centrz_plot);


toc;
end


function [vx,vy,vz] = vsedfield1(x,y,z,centrx,...
centry,centrz, rlength,a,F,vsedtheta)
mu = 8.9e-4;
r = sqrt(x.^2+y.^2+z.^2);
h=centrz;
R = sqrt(x.^2+y.^2+(z+2.*h).^2);
z2 = z+2.*h;


r1 = sqrt(centrx.^2+centry.^2);
h1 = sqrt(((rlength./r1-1).*centrx).^2+...
((rlength./r1-1).*centry).^2);


F1 = F*cos(vsedtheta);
F2 = F*sin(vsedtheta);
```

```
   aa=find(centrx>0);
theta(aa)=pi/2+atan(centry(aa)./centrx(aa));
   bb=find(centrx<0);
theta(bb)=3*pi/2+atan(centry(bb)./centrx(bb));
   cc=find(centrx==0);
       theta(cc)=0;

   theta=theta'; %coordinate trnasformation

   F11=F1.*cos(theta)+F2.*sin(theta);
   %transform to new coordinate
   F31=-F1.*sin(theta)+F2.*cos(theta);
   F21(1:size(F11),1)=0;

   F11=(1-9*a./(16.*h1)).*F11;
   F31=(1-9*a./(8.*h1)).*F31;

   F1=F11.*cos(theta)-F31.*sin(theta);
   F2=F11.*sin(theta)+F31.*cos(theta);

% long range- point force- solid
% wall image reflection
vx = (F1.*((1./r-1./R)+(x.^2)./r.^3-(x.^2)./R.^3) + ...
F2.*(x.*y./r.^3-x.*y./R.^3)+  ...
```

```
2*F1.*h.*(h./R.^3-3.*h.*x.^2./R.^5-z2./R.^3+....
3.*z2.*x.^2./R.^5)+...
2*F2.*h.*(-3.*h.*x.*y./R.^5+3.*x.*y.*z2./R.^5))/(8*pi*mu);

vy = (F2.*((1./r-1./R)+(y.^2)./r.^3-(y.^2)./R.^3) + ...
F1.*(x.*y./r.^3-x.*y./R.^3)+ ...
2*F2.*h.*(h./R.^3-3.*h.*y.^2./R.^5-z2./R.^3+ ...
3.*z2.*y.^2./R.^5)+...
2*F1.*h.*(-3.*h.*x.*y./R.^5+3.*x.*y.*z2./R.^5))/(8*pi*mu);

vz = (F1.*(x.*z./r.^3-x.*z2./R.^3) + ...
F2.*(y.*z./r.^3-y.*z2./R.^3)+ ...
2*F1.*h.*(-3.*h.*z2.*x./R.^5+x./R.^3+...
3.*x.*z2.^2./R.^5)+...
2*F2.*h.*(-3.*h.*z2.*y./R.^5+y./R.^3+...
3.*y.*z2.^2./R.^5))/(8*pi*mu);

  %short range- source dipole
  A = (F1.*x+F2.*y)./r;

vx1 = (((a^2)./(3*(r.^2))).*(F1-3.*A.*x./r))./(8*pi*mu.*r);
vy1 = (((a^2)./(3*(r.^2))).*(F2-3.*A.*y./r))./(8*pi*mu.*r);
vz1 = -(((a^2)./(3*(r.^2))).*(3.*A.*z./r))./(8*pi*mu.*r);
```

```
vxx = vx1+vx;

vyy = vy1+vy;

vzz = vz1+vz;


%short range- particle rotation

omega_x = (y.*vzz-z.*vyy)./(a.*r);

omega_y = (z.*vxx-x.*vzz)./(a.*r);

omega_z = (x.*vyy-y.*vxx)./(a.*r);


vx2 = (a^3)*(omega_y.*z-y.*omega_z)./r.^3;

vy2 = (a^3)*(omega_z.*x-z.*omega_x)./r.^3;

vz2 = (a^3)*(omega_x.*y-x.*omega_y)./r.^3;


ux=vx1+vx2;

uy=vy1+vy2;

uz=vz1+vz2;


kk=find(centrz<2*a);

ux(kk)=(vx1(kk)+vx2(kk)).*centrz(kk)/(2*a);

uy(kk)=(vy1(kk)+vy2(kk)).*centrz(kk)/(2*a);

uz(kk)=(vz1(kk)+vz2(kk)).*centrz(kk)/(2*a);


vx = vx+ux;

vy = vy+uy;
```

```
  vz = vz+uz;


          m=find(r==0);
    vx(m) = (1-9*a/(16*h(m))).*F1(m)/(6*pi*mu*a);
    vy(m) = (1-9*a/(16*h(m))).*F2(m)/(6*pi*mu*a);
    vz(m) = 0;


    clear m
end
```

B.5 MATLAB code for plotting and video generation

```
clear all
a = 2.0e-6;   %particle radius
rlength = 180e-6;
nfacets=15;


centrx_plot=readmatrix('centrxx12.txt');
centry_plot=readmatrix('centryy12.txt');
centrz_plot=readmatrix('centrzz12.txt');


size1 = size(centrx_plot(1,:),2);
```

```
centrx_plot2=readmatrix('centrxx3.txt');
centry_plot2=readmatrix('centryy3.txt');
centrz_plot2=readmatrix('centrzz3.txt');

centrx_plot(:,size(centrx_plot(1,:),2)+ ...
1:size(centrx_plot(1,:),2) ...
+size(centrx_plot2(1,:),2))=centrx_plot2;
centry_plot(:,size(centry_plot(1,:),2)+ ...
1:size(centry_plot(1,:),2) ...
+size(centry_plot2(1,:),2))=centry_plot2;
centrz_plot(:,size(centrz_plot(1,:),2)+ ...
1:size(centrz_plot(1,:),2) ...
+size(centrz_plot2(1,:),2))=centrz_plot2;



centrx_plot(:, size1)=[];
centry_plot(:, size1)=[];
centrz_plot(:, size1)=[];

rad(1:size(centrx_plot,1),1) = a;

%% Create xy VideoWriter object (single color)
% writerObj = VideoWriter('gel1to6_3.avi');
% open(writerObj);
```

```
%
% f = figure;
%  %Set a size if desired
%      width = 1466;
%      height = 1130;
%      set(f,'Position',[0 0 width height])
%
% %Change the renderer to avoid bugs due to OpenGL
%      set(f,'Renderer','ZBuffer')
%
% % zscaled = centrz_plot(:,end)/1e-6;
% % cn = ceil(max(zscaled));
% % cm = colormap(jet(cn));
% %S = repmat(100,numel(centrx_plot(:,1)),1);
% S= rad;
% C= ones(size(centrx_plot,1),1)*[0 0 0];
%
% [sx,sy,sz]= sphere(nfacets);
%
% for i=1:1:size(centrx_plot,2)
%     %Clear the axes.
%      cla;
%
%     %Set the axis aspect ratio to 1:1.
```

```
%      axis equal;
%
%      %Set a title.
%      title([num2str(round((i-1)*9.8/60,1)) ' min'])
%
%      %Display the circles.
%%viscircles([centrx_plot(:,i), ...
% centry_plot(:,i)], rad,'Color','w');
%      hold on
%      c = gray(256);
%      tic;
%      for j= 1:size(centrx_plot,1)
%      surface(sx*S(j)+centrx_plot(j,i), sy*S(j)+...
%       centry_plot(j,i), sz*S(j)+centrz_plot(j,i),...
%                'LineStyle','none',...
%                'FaceColor',C(j,:),...
%          'FaceLighting','gouraud');
%%          colormap(c);
%%          shading interp;
%      end
%%light('Position',[0 0 1],'Style','local','Color',[1 1 1]);
%      %lighting gouraud;
%
%%scatter3sph(centrx_plot(1:10,i), centry_plot(1:10,i)...
```

```
%          ,centrz_plot(1:10,i))
%      toc;
%
%      view(0,90)
%      grid off
%
%      xlim([-rlength-3*a rlength+3*a]);
%      ylim([-rlength-3*a rlength+3*a]);
%
%      %Pause for 1 second.
%      pause(0.3);
%      %movievector(i)= getframe;
%      frame = getframe(f);
%      writeVideo(writerObj,frame);
% end
%
% close(writerObj);

%% Create xy VideoWriter object (multicolor)
writerObj = VideoWriter('vortexx_multicolr2.avi');
open(writerObj);

f = figure;
% Set a size if desired
```

```
    width = 1466;
    height = 1130;
set(f,'Position',[5 5 width height])

%Change the renderer to avoid bugs due to OpenGL
set(f,'Renderer','ZBuffer')

zscaled = centrz_plot(:,end)/1e-6;
cn = ceil(max(zscaled));
cm = colormap(jet(cn));
S = repmat(35,numel(centrx_plot(:,1)),1);

for i=1:1:size(centrx_plot,2)

    %Clear the axes.
    cla;


    %Set the axis aspect ratio to 1:1.
    axis equal;

    %Set a title.
    title([num2str(round((i-1)*3/60,1)) ' min'])
    hold on
```

```
    %Display the circles.
%       viscircles([0, 0], rlength,'Color','c');
%       hold on
%viscircles([centrx_plot(:,i), centrz_plot(:,i)],...
%rad,'Color','b');
    scatter3(centrx_plot(:,i), centry_plot(:,i),...
    centrz_plot(:,i), S,centrz_plot(:,i), 'filled')
    colorbar
    caxis([0 8.5e-6]) %cn*1e-6
    view(0,90)
    grid off

     xlim([-rlength-3*a rlength+3*a]);
     ylim([-rlength-3*a rlength+3*a]);

    %Pause for 1 second.
    pause(0.1);
    %movievector(i)= getframe;
    frame = getframe(f);
    writeVideo(writerObj,frame);

end

close(writerObj);
```

```
%% Create xz VideoWriter object
% writerObj = VideoWriter('vortezz12.avi');
% open(writerObj);
%
% f = figure;
%% Set a size if desired
% width = 800;
% height = 600;
% set(f,'Position',[5 5 width height])
%
%%Change the renderer to avoid bugs due to OpenGL
% set(f,'Renderer','ZBuffer')
%
% zscaled = centrz_plot(:,end)/1e-6;
% cn = ceil(max(zscaled));
% cm = colormap(jet(cn));
% S = repmat(30,numel(centrx_plot(:,1)),1);
%
% for i=1:1:size(centrx_plot,2)
%
%     %Clear the axes.
%     cla;
%
```

```
%
%     %Set the axis aspect ratio to 1:1.
%     axis equal;
%
%     %Set a title.
%     title([num2str(round((i-1)*3/60,1)) ' min'])
%     hold on
%     %Display the circles.
%%      viscircles([0, 0], rlength,'Color','c');
%%      hold on
%%viscircles([centrx_plot(:,i), centrz_plot(:,i)],...
%       rad,'Color','b');
%     scatter3(centrx_plot(:,i), centrz_plot(:,i),...
%     centrz_plot(:,i), S,centrz_plot(:,i), 'filled')
%     colorbar
%     caxis([0 100e-6]) %cn*1e-6
%     view(0,90)
%     grid off
%
%     xlim([-rlength-10*a rlength+10*a]);
%     ylim([-10*a 100*a]);
%
%     %Pause for 1 second.
%     pause(0.1);
```

```
%       %movievector(i)= getframe;
%       frame = getframe(f);
%       writeVideo(writerObj,frame);
%
% end
%
% close(writerObj);
```

CURRICULUM VITAE

NAME: Md Mahmudur Rahman

EDUCATION: Ph.D., Mechanical Engineering
University of Louisville, Louisville, KY, 2021

M.Sc., Mechanical Engineering and Applied Mechanics
University of Nebraska-Lincoln, 2014

B.Sc., Mechanical Engineering
Bangladesh University of Engineering & Technology,
Bangladesh, 2007

AWARDS: ASGSR ISS National Lab Poster Award in
Physical Sciences, ASGSR Annual Meeting, 2019. $500

NSF Innovation Corps grant,
University of Louisville NSF I-Corps, 2017-18, $2500

PUBLICATIONS: Rahman, Md Mahmudur, and Stuart J. Williams
"Cyclic force driven colloidal self-assembly near a
solid surface." *Journal of Colloid and Interface Science*,
Volume 607, Part 2, 2022, Pages 1402-1410,
ISSN 0021-9797

Rahman, Md Mahmudur, and Stuart J. Williams
"Membrane tension may define the deadliest virus
infection." *Colloid and Interface Science Communications*,
40 (2021): 100338.

Rahman, Md Mahmudur, Willis Lee,
Arvind Iyer, and Stuart J. Williams
"Viscous resistance in drop coalescence."
Physics of Fluids, 31, no. 1 (2019): 012104.

Lee, D., K. Golden, Md M. Rahman, A. Moran,
B. Gonzalez, and Sangjin Ryu.
"Fabrication of hydrogels with a stiffness gradient using
limited mixing in the Hele-Shaw geometry."

Experimental Mechanics, (2018): 1-11.

Lee, Donghee, Md Mahmudur Rahman,
You Zhou, and Sangjin Ryu.
"Three-dimensional confocal microscopy indentation
method for hydrogel elasticity measurement."
Langmuir, 31, no. 35 (2015): 9684-9693.

Ehsan, Md, Md Mahmudur Rahman, and Hasan Saadi.
"Effect of fuel adulteration on engine crankcase dilution."
Journal of Mechanical Engineering,
41, no. 2 (2010): 114-120.